

Inverse Problems in Acoustic Tomography: Theory and Applications

THÈSE N° 4165 (2008)

PRÉSENTÉE LE 31 JUILLET 2008

À LA FACULTE INFORMATIQUE ET COMMUNICATIONS
Laboratoire de communications audiovisuelles 1
SECTION DES SYSTÈMES DE COMMUNICATION

ÉCOLE POLYTECHNIQUE FÉDÉRALE DE LAUSANNE

POUR L'OBTENTION DU GRADE DE DOCTEUR ÈS SCIENCES

PAR

Ivana JOVANOVIĆ

Graduate in Electrical Engineering, University of Belgrade, Serbie
et de nationalité serbe

acceptée sur proposition du jury:

Prof. P. Fua, président du jury
Prof. M. Vetterli, Dr L. Sbaiz, directeurs de thèse
Prof. N. Duric, rapporteur
Prof. F. Natterer, rapporteur
Prof. M. Parlange, rapporteur



ÉCOLE POLYTECHNIQUE
FÉDÉRALE DE LAUSANNE

Suisse
2008

Contents

Abstract	v
Résumé	vii
Acknowledgments	ix
Frequently Used Terms, Abbreviations, and Notations	xi
1 Introduction	1
1.1 A brief history of acoustic tomography	2
1.2 Motivations	4
1.3 Thesis outline and contributions	6
I Inverse Problems in Acoustic Tomography	11
2 Theoretical Background	13
2.1 Ray theory of sound propagation in inhomogeneous moving media	13
2.2 The Radon transform	14
2.3 Helmholtz's decomposition	16
3 Forward and Inverse Problems	17
3.1 General formulation	17
3.2 Problem setup	18
3.3 Time-of-flight measurements	20
3.3.1 Longitudinal interaction	20
3.3.2 Time-of-flight estimation techniques	21
3.4 Angle-of-departure/arrival measurements	23
3.4.1 Transversal interaction	24
3.5 Important practical cases	26
3.5.1 Sound speed estimation in the scalar case	27
3.5.2 2D projection of a 3D solenoidal vector field	27
3.5.3 Horizontal slice in the stratified atmosphere	27
3.5.4 Solenoidal vector fields on bounded domains	28
3.5.5 Irrotational vector fields on bounded domains	30
3.6 Reconstruction algorithm	31
3.6.1 Linear versus non-linear tomography algorithm	31
3.7 Error analysis	32
3.7.1 Error in the longitudinal interaction	34

3.7.2	Error in the transversal interaction	35
3.8	Conclusions	35
4	Inversion Methods	37
4.1	Overview	37
4.2	Temperature and wind estimation using the inversion based on l_2 -norm minimization	38
4.2.1	Reconstruction of temperature and wind field	39
4.2.2	Reconstruction of temperature and solenoidal wind field	41
4.2.3	Inversion: conjugate-gradient method	42
4.2.4	Simulation results	42
4.2.5	Discussion	43
4.3	Temperature estimation in diffusive environment using the inversion based on sparsity	49
4.3.1	Compressed Sensing	49
4.3.2	Temperature estimation in a diffusive environment	51
4.3.3	Simulation results	52
4.3.4	Discussion	54
4.4	Characterization of diffusive heat sources using the inversion based on FRI	57
4.4.1	Sampling signals with FRI	57
4.4.2	Characterization of diffusive sources	57
4.4.3	Simulation results	63
4.4.4	Discussion	64
4.5	Conclusions	65
II	Applications	67
5	Breast Cancer Detection	69
5.1	Breast cancer detection with ultrasound	70
5.2	Experimental setup	70
5.3	Signal enhancement and time-of-flight estimation	71
5.3.1	Raw signal analysis	71
5.3.2	Reference signal	74
5.3.3	Signal preprocessing	74
5.3.4	First peak arrival versus cross-correlation method	76
5.4	Results	76
5.4.1	In vitro study	77
5.4.2	In vivo study	82
5.5	Conclusions	83
6	Thermal Therapy Monitoring	87
6.1	Temperature monitoring in tissues with ultrasound	87
6.2	Temperature changes without tissue phase change	89
6.3	Temperature changes with tissue phase change	93
6.4	Conclusions	99

7	Temperature Estimation in the Atmosphere	101
7.1	Temperature and wind estimation in the atmosphere	101
7.2	Experimental setup	102
7.2.1	Transducers	103
7.2.2	Audio card	103
7.2.3	Amplifiers and preamplifiers	104
7.3	Time of flight estimation	108
7.3.1	Probe signal	108
7.3.2	Sample delay estimation	108
7.3.3	Subsample delay estimation	109
7.4	Position calibration	109
7.5	Results	111
7.6	Conclusions	112
8	Conclusions	113
8.1	Summary	113
8.2	Future work	115
	Bibliography	117
	Curriculum Vitae	123

Abstract

Acoustic tomography aims at recovering the unknown parameters that describe a field of interest by studying the physical characteristics of sound propagating through the considered field. The tomographic approach is appealing in that it is non-invasive and allows to obtain a significantly larger amount of data compared to the classical one-sensor one-measurement setup. It has, however, two major drawbacks which may limit its applicability in a practical setting: the methods by which the tomographic data are acquired and then converted to the field values are computationally intensive and often ill-conditioned. This thesis specifically addresses these two shortcomings by proposing novel acoustic tomography algorithms for signal acquisition and field reconstruction.

The first part of our exposition deals with some theoretical aspects of the tomographic sampling problems and associated reconstruction schemes for scalar and vector tomography. We show that the classical time-of-flight measurements are not sufficient for full vector field reconstruction. As a solution, an additional set of measurements is proposed. The main advantage of the proposed set is that it can be directly computed from acoustic measurements. It thus avoids the need for extra measuring devices. We then describe three novel reconstruction methods that are conceptually quite different. The first one is based on quadratic optimization and does not require any a priori information. The second method builds upon the notion of sparsity in order to increase the reconstruction accuracy when little data is available. The third approach views tomographic reconstruction as a parametric estimation problem and solves it using recent sampling results on non-bandlimited signals. The proposed methods are compared and their respective advantages are outlined.

The second part of our work is dedicated to the application of the proposed algorithms to three practical problems: breast cancer detection, thermal therapy monitoring, and temperature monitoring in the atmosphere. We address the problem of breast cancer detection by computing a map of sound speed in breast tissue. A noteworthy contribution of this thesis is the development of a signal processing technique that significantly reduces the artifacts that arise in very inhomogeneous and absorbent tissue. Temperature monitoring during thermal therapies is then considered. We show how some of our algorithms allow for an increased spatial resolution and propose ways to reduce the computational complexity. Finally, we demonstrate the feasibility of tomographic temperature monitoring in the atmosphere using a custom-built laboratory-scale experiment. In particular, we discuss various practical aspects of time-of-flight measurement using cheap, off-the-shelf sensing devices.

Keywords: acoustic tomography, inverse problems, breast cancer, tempera-

ture, wind.

Résumé

Le but de la tomographie acoustique est d'estimer les paramètres inconnus d'un milieu en étudiant les caractéristiques du son s'y propageant. L'approche tomographique est séduisante car elle permet d'obtenir de manière non invasive une quantité de données bien plus grande que la configuration classique dans laquelle les senseurs effectuent des mesures ponctuelles. Elle souffre cependant de deux désavantages majeurs qui limitent potentiellement son application en pratique: les méthodes utilisées pour acquérir les données tomographiques et les convertir en valeurs de champ nécessitent une importante puissance de calcul et sont très souvent mal conditionnées. Cette thèse apporte des solutions à ces deux problèmes en présentant de nouveaux algorithmes de tomographie acoustique permettant l'acquisition de signaux et la reconstruction de champs.

La première partie de notre exposé se concentre sur des aspects théoriques du problème d'échantillonnage tomographique ainsi que sur les méthodes de reconstruction s'y rattachant, aussi bien pour des champs scalaires que vectoriels. Nous démontrons que les mesures classiques de temps de vol ne suffisent pas à reconstruire le champ vectoriel complet. Pour résoudre ce problème, l'utilisation d'un ensemble supplémentaire de mesures est proposé. Ces nouvelles données ont l'avantage d'être directement calculables à partir de signaux acoustiques. Elles ne nécessitent donc pas l'utilisation d'appareils de mesure additionnels. Nous décrivons ensuite trois nouvelles techniques de reconstruction qui sont conceptuellement assez différentes les unes des autres. La première est basée sur une optimisation quadratique et ne nécessite aucune information a priori. La seconde repose sur la notion de parcimonie dans le but d'améliorer la qualité de reconstruction lorsque peu de données sont disponibles. La troisième approche examine la reconstruction tomographique comme un problème d'estimation paramétrique et le résout en utilisant certains résultats récents sur l'échantillonnage de signaux à bande non-limitée. Les méthodes considérées sont comparées et leurs avantages respectifs brièvement exposés.

La deuxième partie de notre travail est dédiée à l'application des algorithmes susmentionnés à trois problèmes pratiques: la détection de cancer du sein, la visualisation lors de thérapies thermiques et la mesure de température dans l'atmosphère. La détection de cancer du sein s'effectue en cartographiant la vitesse du son dans le tissu mammaire. Une contribution importante de cette thèse est le développement d'une technique de traitement du signal qui réduit de manière significative les artefacts qui apparaissent dans les tissus fortement inhomogènes et absorbants. Le problème du contrôle de température lors de thérapies thermiques est ensuite considéré. Nous montrons que certains de nos

algorithmes permettent d'obtenir une meilleure résolution spatiale et proposons des stratégies pour réduire leur complexité. Finalement, nous démontrons la faisabilité de la mesure tomographique de température dans l'atmosphère à l'aide d'une expérience menée à l'échelle de laboratoire. En particulier, nous discutons différents aspects pratiques liés à l'estimation de temps de vol à l'aide de senseurs bon marché.

Mots-clés: tomographie acoustique, problèmes inverses, cancer du sein, température, vent.

Acknowledgments

First and foremost, I would like to thank to my two thesis supervisors Professor Martin Vetterli and Dr. Luciano Sbaiz for their support, constructive feedback and strong encouragement. Martin, thank you for offering me the opportunity to work in your lab and for the inexhaustible enthusiasm and inspiration you have been giving me. Luciano, thank you making the first steps in the tomography project and for a wonderful help in solving all possible problems.

I am thankful to the thesis committee members: Professor Nebojsa Durić, Professor Frank Natterer, and Professor Marc Parlange for accepting to evaluate this work, for their appreciation and valuable comments. Special thanks goes to Nebojsa and the entire image processing team at the Karmanos Cancer Institute, for giving me the opportunity to do an internship in their group. Thank you for a great collaboration and your generous support to provide us with the access to clinical research facilities.

I also owe many thanks to Baltasar Beferull-Lozano for a fruitful collaboration on the doctoral school project during my pre-doc school.

I would also like to thank all the past and present members of LCAV for all the great times spent together. Special thanks goes to my office mates Bob, Vladan, and Ali. I also thank Ali for the successful collaboration on the “sparse tomography” project.

I would like to thank all my friends from Switzerland and abroad, for their support and great parties we had together. The fellows from the predoctoral school and the Serbian community made my stay in Switzerland enjoyable and unforgettable.

I am especially thankful to Olivier, for his support, constant help and patience he has showed during last four years. Olivier, thank you for all the time we spent together and many other things that have changed me and my stay in Switzerland. I have learned so many things from you.

I am very thankful to my “second” family in Switzerland, my aunt Miska, my uncle Naim, and my cousin Arian for making me feel as at home. You were always of a great support and help for me.

Finally, I am very grateful to my family, my mother Milina, my father Miodrag, and my sister Zorana, for their dedication, unconditional love and support they always give me. They have always believed in me and I would like to dedicate this thesis to them.

Frequently Used Terms, Abbreviations, and Notations

Terms and abbreviations

MSE: mean squared error;

solenoidal vector field: vector field whose divergence is zero;

source-free vector field: vector field whose divergence is zero;

irrotational vector field: vector field whose curl is zero;

curl-free vector field: vector field whose curl is zero;

Notation and variables

vectors are bold lowercase letters (\mathbf{y} , $\boldsymbol{\alpha}$, etc);

matrices are bold uppercase letters (\mathbf{D} , \mathbf{F} , etc);

\mathbf{b} gradient of the eikonal, $\mathbf{b} = \nabla\xi$;

b amplitude of the vector \mathbf{b} ;

c speed of sound;

c_0 reference or average speed of sound;

Δc sound speed variation, $\Delta c = c - c_0$;

D bounded region;

∂D boundary of D ;

\mathbf{d} data vector;

d_i i -th element of \mathbf{d} ;

\mathbf{G} matrix representing the mapping from the model parameters to the measurements;

$\hat{\mathbf{G}}$ estimate of \mathbf{G} ;

l_Γ longitudinal interaction along Γ ;

\mathbf{m} model parameters vector;

m_j j -th element of \mathbf{m} ;

$m(x, y)$ two-dimensional function;

M two-dimensional Fourier transform of $m(x, y)$;

\mathbf{n} vector normal to the wave front;

$\mathcal{R}m$ the Radon transform of the function m ;

$\hat{\mathcal{R}}m$ one-dimensional Fourier transform of $\mathcal{R}m$;

\mathbf{r}	position vector, $\mathbf{r} = (x, y, z)$;
\mathbf{r}_T	transmitter's position, $\mathbf{r}_T = (x_T, y_T, z_T)$;
\mathbf{r}_R	receiver's position, $\mathbf{r}_R = (x_R, y_R, z_R)$;
\mathbf{s}	vector tangent to the trajectory Γ ;
\mathbf{s}_\perp	vector normal to the vector \mathbf{s} ;
t	time variable;
t_Γ	transversal interaction along Γ ;
\mathbf{u}_g	group velocity;
u_g	group velocity amplitude;
\mathbf{v}	medium velocity, wind field for the case of the atmosphere, $\mathbf{v} = (v_x, v_y, v_z)$;
\mathbf{v}_{xy}	two-dimensional medium velocity in the xy -plane;
\mathbf{v}_S	solenoidal vector field;
\mathbf{v}_I	irrotational vector field;
\mathbf{v}_H	homogeneous component of the vector field \mathbf{v} ;
$y(t)$	continuous signal;
Γ	sound ray trajectory;
θ	angle of the sound wave;
θ_T	angle-of-departure;
θ_R	angle-of-arrival;
ξ	eikonal;
σ_l^2	variance of the longitudinal interaction;
σ_t^2	variance of the transversal interaction;
τ	time-of-flight;
τ_0	reference time-of-flight;
ϕ	scalar potentials;
ψ	vector potentials;
Ω	bounded region;
$\partial\Omega$	boundary of Ω ;
$\mathbf{1}_\Gamma$	indicator function with the support Γ ;

Chapter 1

Introduction

The word *tomography* is derived from the greek words *tomos* which means “a slice” or “a cutting”, and *graphein* which means “to draw” or “to write”. Thus, tomography is simply imaging of a slice. It produces an image of the internal structure of an object based on the interactions between the object and energy emitted by radiating devices and captured by appropriate sensors. The different choices of energy radiation (X-ray, γ -ray, neutron, light, sound, electrical, etc.) used in probing different mediums result in a vast variety of tomography disciplines: X-ray tomography, magnetic resonance imaging, neutron tomography, positron emission tomography, ultrasound tomography, optoacoustic tomography, seismic tomography, quantum tomography, etc. As a result, tomography methods have been widely used for many decades in medicine, archaeology, biology, geophysics, oceanography, and technology for non-destructive testing. Examples include the use of X-rays in medicine to diagnose a large number of different disease entities, or seismic tomography to image the interior of the Earth, for instance, for oil exploitation.

There are at least three reasons why tomographic methods are very appealing. First, they are non-invasive methods: the sensors need not be located inside the field being measured. Second, tomography methods can collect a significantly larger amount of data than the classical one-sensor one-measurement setup (see Figure 1.1). Third, the information provided by processing the signals received at multiple locations enables to acquire a global (as opposed to a punctual) knowledge of the measured field. These benefits, however, cannot be achieved without some sacrifice. The methods by which the tomographic measurements are acquired and converted to field information, the latter being referred to inversion methods, are computationally intensive and often ill-conditioned.

This thesis studies inversion methods for a tomography discipline that uses sound propagation to infer the properties of the medium. This discipline is called acoustic tomography, where acoustic generally refers to the use of audible sound as well as ultrasound and infrasound. A variety of applications, in basic research and in technology, exploit the fact that the transmission of sound is affected by the medium through which it passes. It thus provides information concerning the properties of the medium, including objects, inhomogeneities and the velocity of the medium. Different methods have been developed over the past decades as a means to recover these properties. We next review some

key historical discoveries that have paved the way towards the use of acoustic tomography in a variety of settings.

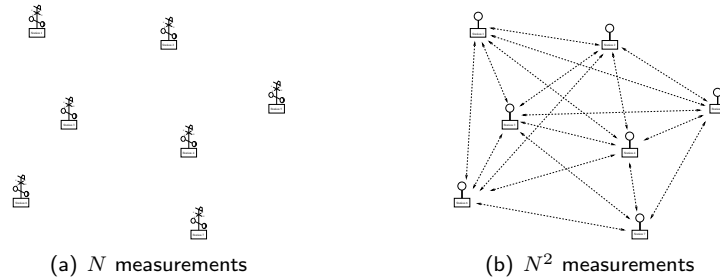


Figure 1.1: Tomography methods are non-invasive and allow to collect an amount of data proportional to the square of the number of sensors. (a) A classical one-sensor one-measurement setup. (b) A tomographic setup - every sensor sends signals to all other sensors.

1.1 A brief history of acoustic tomography

The research on acoustic tomography starts with the understanding of sound propagation in a moving inhomogeneous medium, and the differences between the scalar and vector tomography imaging. In general, a medium can be described by its scalar (e.g. medium inhomogeneities), and vector (e.g. medium speed) properties. Trying to image vector properties of the medium fundamentally differs from imaging its scalar properties. Moreover, the vector properties of the medium influence differently the sound propagation than the scalar properties. This fact may be rather subtle and, in fact, in the past, it was not immediately recognized by the research community.

Sound propagation

The theory of acoustics in moving media was initially developed as a study of sound propagation in the atmosphere. From time immemorial, it had been known that, in the atmosphere, the sound from a source was more noticeable downwind than upwind. This phenomena was confirmed in the experiments by Delaroché in 1816 [21], and Arago in 1822 [2], but a correct qualitative explanation was given only in 1857 by Stokes [68]. Later in 1874, Reynolds [60] gave nearly the same explanation, but used the concept of sound *ray* to explain sound propagation. Furthermore, Reynolds showed that sound rays in the atmosphere *bend*; for example upwards if there is a temperature lapse with height. Only a long time later, in 1945, Rayleigh [59] derived the mathematical expressions of sound propagation in moving media and formulated a *refraction law* for acoustic rays traversing a stratified moving medium. The ray path obtained by Rayleigh, however, does not coincide with the real ray path because in a moving medium the unit vector normal to the wavefront does not usually coincide with the tangent to the ray path. Barton [4] was the first to show that these two vectors may not coincide in a moving medium. Since then, many papers on acoustics in moving medium have pointed out that Rayleigh made

a mistake. Other researchers later rederived expressions to compute acoustic ray path in moving medium.

It is now well established that the propagation of sound waves in an inhomogeneous moving medium, e.g. the atmosphere, is completely determined by the system of linearized equations of fluid dynamics [53]. When the medium inhomogeneities are large compared to the wavelength, the energy propagation is well described by the ray theory of sound propagation. As pointed by Barton, the ray theory for moving media differs from the ray theory in still media, and this point will be discussed in more details in Section 2.1.

Scalar tomography

The mathematical basis for all tomography disciplines was introduced almost a century ago in the pioneering work of the Austrian mathematician Johann Radon. In his paper from 1917 [57], Radon proved that any two-dimensional object can be reconstructed uniquely from an infinite set of its line-integrals, the so-called projections. This result, known as the Radon transform, laid down the key concept needed for the tomographic imaging of *scalar* functions. The result has been independently rediscovered a number of times since then by other mathematicians, radio astronomers, electron microscopists, workers in optics, and medical radiologists. The first practical reconstructions of this kind were accomplished by the radio astronomer Ronald Bracewell in 1956 [8]. The same mathematical problem later arose in electron microscopy [61, 26], and in various optical applications [62].

It is in the area of medical diagnosis, however, that the most excitement has been generated around the Radon transform. The first practical, clinically oriented solution to reconstructive tomography appeared in the early 1960, after Alan Cormack [18, 19] began to popularize and extend the work of Radon. Cormack received the 1979 Nobel prize for medicine, jointly with Godfrey Hounsfield, who developed the first EMI Scanner, involving X-ray scanning and digital computing [30, 31]. This first scanner generated images of isolated slices of the brain with excellent tissue contrast. In 1974, a whole body scanner was developed by Ledley. Since then, a number of different companies have manufactured body scanners, and a broadly based competitive market has by now been developed. A standard treatise on the mathematics behind scalar tomography is given by F. Natterer [48].

Although the X-ray scanner was the spark that ignited the greatest excitement in the tomography field, other kinds of radiation have proved to be successful as well. The early work in acoustic tomography was based on algorithms that were developed for X-ray tomography. Later, it became evident that more accurate models of the physical mechanisms generating the image were needed for high resolution and correct reconstruction. This point will be of particular interest in this thesis.

Vector tomography

The ability to reconstruct a scalar function using tomography techniques has resulted in a wealth of applications in many disciplines. A number of other applications, related to imaging of a flow field, has raised the need for similar methods in tomographic reconstruction of vector fields.

The velocity of the medium is a vector function. While in the scalar case the state of a particular point contributes equally to all rays passing through it, the situation for vector fields is far more complicated in that the contribution also depends on the direction of sound propagation. A basic result of vector tomography is that the integrals of a vector function along all lines only allow to recover the curl part of the vector field.

In an early study, Johnson *et al.* [34] noted that there is a part of vector fields, which they refer to as “invisible” part, that could not be reconstructed from the line integral measurements. They proposed a technique to compute only one particular solution of the vector field. The first to reach the full mathematical understanding of the problem was Norton [49] in 1988. Working in the Fourier domain he derived a reconstruction method for the vector fields and explored the nature of the ambiguity using the Helmholtz decomposition of vector fields. Moreover, he pointed out important situations where it is possible to fully determine the field, for instance divergence-free fields fulfilling homogeneous Neumann conditions on the boundary. During the short history of vector tomography, the basic result about the curl has been repeatedly and independently discovered, also by Braun and Hauck [10], Juhlin [38], and Sharafutdinov [65]. In this thesis, we will treat the problem of vector tomography through the application of wind and temperature estimation in the atmosphere.

1.2 Motivations

Applications of acoustic tomography methods are diverse. They are irreplaceable methods in oceanography, seismology, and showed a great potentials in medicine. The results of this thesis are motivated by two important applications: acoustic tomography in the atmosphere, and acoustic tomography for breast screening. The first one can be identified as a vector tomography problem, while the second one is a scalar tomography problem. Let us look more in details at these two applications of interest.

Acoustic tomography in the atmosphere

Sound has been used to probe vertical structure of the atmosphere since the early 1900’s, when scientists used powerful explosions on the ground, to deduce the presence of temperature inversion and strong winds in the stratosphere [23, 20]. Similar schemes with controlled ground-based sources were later used by other scientists, including Greenfield *et al.* [27], Ostashev [52], and Chunchuzov *et al.* [15]. These schemes could be referred to as vertical-slice acoustic tomography, although the term was not used at that time.

A horizontal-slice acoustic tomography for monitoring phenomena in the atmosphere, in particular temperature and wind, was first proposed in the 1990’s [66, 76], as an attempt to use the techniques successfully applied in monitoring ocean’s structure [47]. Shortly after, imaging these physical quantities in near ground atmosphere with acoustic tomography has been demonstrated in field experiments [76, 16, 78]. However, the knowledge on the basic result of vector tomography seems to have not been much transferred between the disciplines. Despite the fact that line integrals are not sufficient to recover the

full vector field, previous work only considered the line integrals (obtained from the time-of-flights measurements) to reconstruct both the scalar (temperature) and the vector (wind) fields. Hence, one of the motivation for this work was to bring forth related material from adjacent fields of research, and to present some known as well as new results. In particular, the questions of joint two-dimensional temperature and wind field reconstruction, for general and specific cases of wind field will be settled.

Acoustic tomography for breast cancer detection

The use of acoustic, more precisely ultrasound tomography for breast cancer screening is relatively new. There is still no commercialized ultrasound breast scanner, but many competing groups are currently working on such a device. While the need for this research is obvious, it is further motivated by the following numbers.

Within the European Union, every 2.5 minutes a woman is diagnosed with breast cancer. Every 7.5 minutes a woman dies from the disease. The incidence of breast cancer is increasing. Breast cancer remains the main cause of death in women aged between 35 and 59. The importance of screening becomes even more obvious when knowing that 90% of all breast cancer cases could be cured if detected early and treated in quality assured specialist breast units.

Although mammography is the gold standard for breast imaging, it also generates many abnormal findings not related to cancer leading to the false positive rate that can be as high as 80%. The differentiation of benign from malignant tissue in mammogram findings is as well very poor for young women and women with dense breast, and results in 50% of the false negative rate. In order to overcome these problems, mammography is generally complemented by ultrasound imaging. This latter helps differentiate cysts from solid masses and has become the dominant mode for guiding needle biopsy. Efforts to improve the diagnostic accuracy of ultrasound have been carried out on two fronts. One approach is based on improving the classical ultrasound devices and techniques that rely on reflection (or B-mode) imaging while the second, to which our own study belongs, utilizes transmission tomography to characterize breast tissue. Greenleaf *et al.* [28] have shown that using the parameters of sound speed and attenuation could help in differentiate benign masses from cancer. Namely, the cancer has a high sound speed and attenuation when comparing to normal tissue or benign masses. As a direct result of this and other similar studies, a number of investigators developed transmission ultrasound scanner as an attempt to measure transmission parameters *in vivo*. Examples include the work of Carson *et al.* [13], Andre *et al.* [1], Johnson *et al.* [32], Marmarelis *et al.* [46], Liu and Waag [42], and Duric *et al.* [24].

Our own contribution to this research came as a result of a collaboration with the latter research group from the Karmanos Cancer Institute in Detroit, USA. They have developed the Computed Ultrasound Risk Evaluation System (CURE), the clinical breast imaging device that aims at whole breast, operator independent imaging, and differentiation of breast masses. In order to improve the final image quality in terms of estimation accuracy and resolution we have worked both on the acquisition part of the system, that is, enhancement of the received signal, and the inversion part, that is, employing different inversion methods. Using the same prototype we also show that ultrasound transmis-

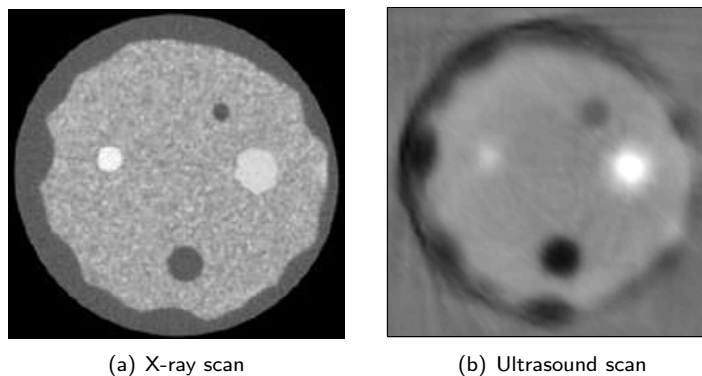


Figure 1.2: The ultrasound tomography images are comparable with those of X-ray scanners. The ultrasound scan of a breast-mimicking phantom represents the sound speed map inside the phantom. The reconstruction is obtained using our algorithms.

sion tomography can be used to monitor thermal therapies, for instance, the cryosurgery.

The potentials of acoustic tomography for medical applications are high. The ultrasound tomography images are comparable with those of X-ray scanners, while the method is non-ionizing and there is no limitation in number of scans we can perform. In Figure 1.2(a), we can see the X-ray scan of a breast-mimicking phantom and in Figure 5.8(b) the reconstruction of a sound speed map obtained using our reconstruction algorithms. The gray scale for the sound speed map is linear from 1464 m/s to 1552 m/s (for more details see Chapter 5).

1.3 Thesis outline and contributions

One of the most appealing aspects of the subject of this thesis is its interdisciplinary nature. Topics that we cover range from the theoretical fundamentals of inverse problems in scalar and vector tomography, to some practical details on how to build the experimental prototypes for the applications of acoustic tomography in meteorology and in medicine. In all this, we will take a signal processing point of view and put the emphasis on developing practical algorithmic solutions.

In the first part of the thesis, we treat acoustic tomography as an inverse problem, focusing on the uniqueness of the solution, and introducing new inversion methods.

In *Chapter 2*, we give some basic theoretical results that are going to be used throughout this thesis. First, we review the theory of sound propagation in moving inhomogeneous medium, using the principles of geometrical acoustics, namely, the ray theory of sound propagation. We point out that some particular results of the ray theory in a moving medium may not be obtained from the analogous results for a motionless medium. Further, the theoretical basis for all tomographic reconstruction, the Radon transform, is presented.

We briefly discuss different inversion formulas, and emphasize the difference between the transform-based and algebraic inversion methods, the latter being used in our work. Finally, we present Helmholtz's theorem, also known as the fundamental theorem of vector calculus. The decomposition of vector field in its solenoidal (divergence-free) and the irrotational (curl-free) component given by this theorem will play an important role in deriving the theoretical results in the sequel.

In *Chapter 3*, we study forward and inverse problems in acoustic tomography for the general cases of scalar and vector fields. The scalar and vector field problems appear in reconstructing the sound speed and the medium speed in a moving inhomogeneous medium. Primarily, we show that, when the relationship between the measurements and the unknown vector field is linearized, the classical time-of-flight measurements are insufficient to reconstruct the irrotational component of the vector field. As a solution, an additional set of measurements is proposed. This set is sensitive to the missing irrotational component of the vector field. The main novelty is that these new measurements are solely related to the parameters of sound propagation, more precisely, to the angle-of-departure and angle-of-arrival of sound waves. Hence, the reconstruction of scalar and vector fields is now physically realizable in acoustic measurements. To take the full advantage of the additional set of measurements the bent-ray model of sound propagation introduced in *Chapter 2* is considered. We also discuss important practical cases for which the required measurements can be reduced to one of the two proposed sets. The most important result in this part, is a proof that when a temperature (scalar) and a divergence-free 2D wind (vector) field are observed on bounded domains, the complete reconstruction is possible using only the time-of-flights. No additional measurements are needed, unlike what was suggested in previous research. Analogously, we prove that the angle-of-departures/arrivals are sufficient to reconstruct temperature and curl-free 2D wind fields on bounded domains.

When the bent ray model of sound propagation is considered, the measured data are related to the integrals along bent rays. However, as the bending depends on the underlying fields, a non-linear relation between the measurements and the unknown fields is introduced. We apply an iterative method to solve this non-linear problem. The iterations alternate between estimating the trajectories and the unknown fields. The algorithm compares the measurements with the forward prediction of the current state of the system, and computes the updates by inverting the algebraic system of equation. This inversion step is discussed in details in *Chapter 4*, as it is an inherent and the most important step in the algorithm, even for the case of the straight ray sound propagation model (when the algorithm stops after the first iteration). We show that although the component needed to compute the irrotational part of the field is approximated using the angle-of-departure/arrival measurements, the proposed algorithm cancels the approximation error, since the iterations stop when the measurements are equal to the output (forward prediction) of the current estimate. A similar idea is used in the so-called zero-methods. We also suggest a new method for estimating the time-of-flights, suitable for mediums with high inhomogeneities and/or high attenuation. This method is experimentally tested in *Chapter 5* and *Chapter 6*. The two methods for estimating the angle-of-departure/arrivals are also given. Finally, we analyze the reconstruction

error. By following the general estimation approach for error analysis, we emphasize two important sources of errors: the errors in the measurements; and the mismatch between the reality and the assumed field model.

In *Chapter 4*, we propose three inversion methods that can be applied in tomographic setups, both in the context of the inversion inside the iterative reconstruction algorithm presented in Chapter 3, and as the inversion step in the non-iterative case. The three methods are conceptually different, and the difference is based on whether or not any *a priori* information (or regularization) is used, and whether or not the inversion method is linear. Also, in all three methods, different sets of model parameters are chosen to describe the unknown fields. First, a method based on l_2 -norm minimization of error is presented. It does not use any *a priori* information, and, therefore, it refers to a general practical situation of estimating the sound speed and the moving component of an inhomogeneous moving medium. The method is applied to a concrete problem of estimating wind and temperature in the atmosphere. This method is used to test the convergency of the iterative non-linear tomography algorithm. Second, we propose a new inversion method for acoustic tomography. This method is based on the idea of compressed sensing, that is, acquiring a sparse signal in the most efficient way. We show that this method can be successfully applied to a large class of problems in acoustic tomography for two reasons. First, the fields that we want to recover are compressible in the sense that they have a sparse expansion in a set of basis functions. Second, the tomographic measurements are such that the solution can be computed with fewer measurements than the number of unknowns. The concrete example that we consider is the problem of temperature estimation in a diffusive environment. Finally, the third method is based on the idea of sampling signals with finite rate of innovation, namely, the signals that have a parametric representation with a finite number of degrees of freedom per unit of time. Although, in general, these signals are neither bandlimited nor live on shift-invariant spaces, their exact reconstruction can be achieved using only a finite number of measurements. We show that some of these sampling schemes can be extended for the use in acoustic tomography. Particularly, we show that this method can be applied in the problem of characterizing the diffusive heat sources localized in space and time. We present a method to compute the positions, time origin, and the amount released from these diffusive sources. A comparison between the three methods is drawn at the end of the chapter.

The second part of the thesis presents the real applications of acoustic tomography to: breast cancer detection and breast screening, thermal therapy monitoring, and temperature estimation in the atmosphere. In all three examples, the reconstruction of the unknown field is obtained using the iterative algorithm proposed in Chapter 3, and the bent ray model for sound propagation. The next two chapters of the thesis follow as a result of a collaboration with an imaging research group at the Karmanos Cancer Institute, Wayne State University, Detroit, USA, which has developed a clinical breast imaging prototype, based on acoustic tomography principles. Their generous support to provide us with the access to clinical research facilities allowed us to test our algorithms *in vitro* and on human data.

In *Chapter 5*, we consider the use of acoustic, more precisely ultrasound transmission tomography for breast cancer detection and breast screening. The

goal is to obtain a map of the sound speed inside the breast tissue, that is later used for characterization of different tissue masses. Faced with the problem of estimating the time-of-flights in very inhomogeneous and absorbing medium, we propose to use a beamforming technique to overcome this problem. The technique shows to be very efficient in reducing many artifacts. We think that introducing beamforming to acoustic tomography imaging, and suggesting a method to compute the parameters of the beamformer, is an important contribution of the thesis. Next to the reconstruction obtained using the l_2 -norm minimization of error, we also show the reconstructions using the methods based on sparsity. The latter methods are subject of our future research, as they show a great potential.

In *Chapter 6*, we consider the problem of temperature monitoring during thermal therapies, particularly the tissue freezing with cryoprobes. We show that the sound speed can be used as a temperature dependent parameter. The mapping between the temperature and the sound speed was not in the scope of this work, and we only summarize some existing results on this topic. The estimation of sound speed in the scenario of tissue freezing is by itself a challenging task because, first, the sound is highly attenuated when traversing the frozen tissue; and second, the sound speed to be reconstructed has a high spatial bandwidth, due to the dramatic change of sound speed between the frozen and unfrozen tissue. We show that the first problem can be overcome using again the beamforming technique. As the classical reconstruction algorithms inherently smooth the reconstruction, we propose to solve the second problem by applying the reconstruction techniques based on sparsity. We also suggest ideas on how to speed up the reconstruction algorithms in order to enable real time applications, which is important in clinical settings.

In *Chapter 7*, we describe how we built a laboratory size acoustic tomography setup, used for estimating temperature from time-of-flight measurements. The experiment aims at showing the feasibility of our acoustic tomography method, identifying the practical problems and providing the bounds on the achievable accuracy. The setup consists of 12 transmitters and 12 receivers placed on a ring with a radius of 1 m. To compensate for relatively modest power levels of input and output signals, arrays of amplifiers and preamplifiers are used. Both the amplifiers and preamplifiers were built in our laboratory in order to meet the tight specifications of bandwidth and SNR. To avoid mechanical distance calibration, we use the time-of-flights estimates to compute the positions and the delays of the transducers. This is a favorable option and it allows the system to be self-calibrated. We also show the technique to estimate the time-of-flights with an accuracy of the order of 10^{-7} s, even when the sampling interval is of the order of 10^{-5} s (96 KHz sampling frequency of the audio card). We show that it is possible to measure small temperature variations with good spatial resolution. Except for the amplifiers and the preamplifiers, the whole system is assembled from commercially available and relatively cheap components. This proves that acoustic tomography has a good potentials to replace some of today's expensive meteorological techniques.

Finally, *Chapter 8* summarizes this thesis and discusses some directions for future research.

Part I

Inverse Problems in Acoustic Tomography

Chapter 2

Theoretical Background

In this chapter, we present basic theoretical results that are going to be used throughout this thesis. First, we review the theory of sound propagation in moving inhomogeneous medium, using the principles of geometrical acoustics. Further, we revisit the theory of the Radon transform, that is the theoretical basis for all tomographic reconstructions. We briefly discuss different inversion formulas and methods. Finally, we present Helmholtz's theorem, that plays an important role in understanding vector tomography problems.

2.1 Ray theory of sound propagation in inhomogeneous moving media

In the following, we will use the equations for sound propagation presented in [53]. Let the acoustical properties of a moving medium be described by the speed of sound $c(\mathbf{r})$, and let its velocity be $\mathbf{v}(\mathbf{r})$, where both c and \mathbf{v} are arbitrary well-behaved functions of the position vector \mathbf{r} . The eikonal equation is given by:

$$\frac{c_0}{c(\mathbf{r})} - \frac{\mathbf{v}(\mathbf{r}) \cdot \nabla \xi(\mathbf{r})}{c(\mathbf{r})} = |\nabla \xi(\mathbf{r})|, \quad (2.1)$$

where c_0 is an arbitrary constant reference sound speed (e.g. the spatial average), ξ is the eikonal function (phase) of the wavefront, and the operator ∇ is the gradient operator. Equation (2.1) was derived by Bolkhintzev [6], and it is called the Hamilton-Jacobi equation. It is shown that the solution of (2.1) can be reduced to the integration of the characteristic system of the differential equations:

$$\frac{d\mathbf{r}}{d\nu} = \frac{\mathbf{b}}{b} + \frac{\mathbf{v}}{c}, \quad (2.2)$$

$$\frac{d\mathbf{b}}{d\nu} = -\frac{c_0 \nabla c}{c^2} - \frac{\nabla(\mathbf{b} \cdot \mathbf{v})}{c} + \frac{\mathbf{b} \cdot \mathbf{v} \nabla c}{c^2}, \quad (2.3)$$

$$\frac{d\xi}{d\nu} = b + \frac{\mathbf{b} \cdot \mathbf{v}}{c}. \quad (2.4)$$

In these equations, ν is the independent variable, and the vector $\mathbf{b} = \nabla \xi$. The vector $\mathbf{r}(\nu)$ determines the ray path of a sound wave in an inhomogeneous

moving medium. The ray path $\mathbf{r}(\nu)$ can be obtained as a solution of (2.2) and (2.3), while (2.4) is not needed. In many cases, it is convenient to relate the independent variable ν to the ray length s , or the time t . The relationship between s , t , and ν is given as [53]:

$$\begin{aligned} d\nu &= \frac{c ds}{u_g}, \\ dt &= \frac{ds}{u_g}, \end{aligned}$$

where u_g is the amplitude of the group velocity \mathbf{u}_g . Changing the time variable instead of the independent variable leads to a property which is useful in understanding the effect of the moving medium: the group velocity along a ray is the sum of the medium speed and the sound speed. Equations (2.2) and (2.3) become:

$$\frac{d\mathbf{r}}{dt} = c\mathbf{n} + \mathbf{v}, \quad (2.5)$$

$$\frac{d\mathbf{b}}{dt} = -\frac{c_0 \nabla c}{c} - \nabla(\mathbf{b} \cdot \mathbf{v}) + \frac{\mathbf{b} \cdot \nabla c}{c}. \quad (2.6)$$

where $\mathbf{u}_g = d\mathbf{r}/dt$, and \mathbf{n} is a unit vector normal to the wavefront $\mathbf{n} = \mathbf{b}/b$. From (2.5), and (2.6), the ray path can be computed imposing some initial conditions for \mathbf{r} and \mathbf{b} . For example, the starting point may correspond to the transmitter position $\mathbf{r}(0) = \mathbf{r}_T$, and the initial $\mathbf{b}(0)$ is chosen such that the ray reaches the receiver (see Figure 2.1). The method just shown for solving the differential equations is called the shooting method. We use this method for the ray tracing algorithm. More on the implementation of the shooting method can be found in [56].

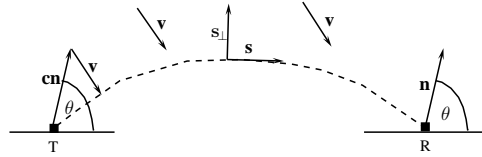


Figure 2.1: Sound propagation. An example of a ray trajectory with the vectors \mathbf{n} normal to the wave front, \mathbf{s} tangent to the trajectory, \mathbf{s}_\perp normal to \mathbf{s} . The vector \mathbf{v} represents the wind field, and c is the sound speed.

2.2 The Radon transform

For an arbitrary function $m(x, y)$, its Radon transform is defined as the integral of $m(x, y)$ along a straight line $\Gamma(r, \phi)$

$$\mathcal{R}m(r, \phi) = \int_{\Gamma(r, \phi)} m(x, y) ds, \quad (2.7)$$

where $Rm(r, \phi)$ refers to the projection of $m(x, y)$, acquired as a function of r , the distance along the projection, and ϕ , the rotation angle. The simplest projection is a collection of parallel ray integrals as given by $Rm(r, \phi)$ for a constant ϕ .

The one-dimensional Fourier transform along r yields

$$\hat{\mathcal{R}}m(k, \phi) = \int \int_{\Gamma(r, \phi)} m(x, y) ds e^{-jkr} dr. \quad (2.8)$$

Using

$$\begin{bmatrix} x \\ y \end{bmatrix} = \begin{bmatrix} \cos \phi & -\sin \phi \\ \sin \phi & \cos \phi \end{bmatrix} \begin{bmatrix} r \\ s \end{bmatrix}, \quad (2.9)$$

and (2.8), one obtains

$$\hat{\mathcal{R}}m(k, \phi) = \int \int m(x, y) e^{-j(k \cos \phi x + k \sin \phi y)} dx dy,$$

and in a shorter notation

$$\hat{\mathcal{R}}m(k, \phi) = M(k \cos \phi, k \sin \phi), \quad (2.10)$$

where M denotes the 2D Fourier transform of the function m . This is commonly called the projection slice theorem, and informs us that one projection contains the spectral information along one center line in the 2D spectral domain. The theorem is the basis for a variety of reconstruction algorithms such as the direct Fourier inversion method and the filtered back-projection. Here, we present one form of the Radon's inversion formula

$$m(x, y) = \frac{1}{2\pi} \int_0^\pi \int_{-\infty}^\infty \frac{1}{x \cos \phi + y \sin \phi - r} \frac{\partial Rm(r, \phi)}{\partial r} dr d\phi.$$

This is one type of a transform-based inversion, in which a special measurements setup is assumed, e.g. we need the projections for the angles from 0 to π . In practice, we do not have an infinite number of projections and the inversion formulas are to be discretized. Different scanning geometry and different discretization lead to different forms of the inversion formula.

In our work, we are going to use the fact that the scalar function can be recovered from its Radon transform projections for the theoretical derivation of our results. However, practical reconstruction algorithms will be based on an entirely different approach for tomographic imaging. In this approach, we assume that the cross section consists of an array of unknowns, and then we set up algebraic equations for the unknowns in terms of the measured projection data. This approach is useful in many situations. For example, sometimes, it is not possible to measure a large number of projections, or the projections are not uniformly distributed over 180° or 360° , both these conditions being necessary requirements for the transform based techniques to produce results with a good accuracy. More importantly, the algebraic techniques are useful in acoustic tomography, where the sound propagation rays between the source and the receiver are subject to ray bending on account of refraction. In this case, we do not even have the projections of the function m (in its strict sense), because the integration is done along curves. To compute the solution, we

then need to solve a linear system of equations. Therefore, since in acoustic tomography, we do not have the classical Radon inversion setup, we will study various alternative inversion methods.

2.3 Helmholtz's decomposition

According to Helmholtz's theorem, every vector field \mathbf{v} can be decomposed into an irrotational \mathbf{v}_I (or curl-free, $\nabla \times \mathbf{v}_I = 0$) and solenoidal \mathbf{v}_S (or source-free, $\nabla \cdot \mathbf{v}_S = 0$) component:

$$\mathbf{v}(\mathbf{r}) = \mathbf{v}_I(\mathbf{r}) + \mathbf{v}_S(\mathbf{r}).$$

More precisely, we have:

Theorem 2.1 (Helmholtz decomposition). Let $n = 3$ or $n = 2$, and let $\mathbf{v} \in \mathcal{S}(\mathbb{R}^n, \mathbb{R}^n)$. Then there exist unique $\mathbf{v}_S, \mathbf{v}_I \in \mathcal{C}^\infty(\mathbb{R}^n, \mathbb{R}^n)$ with $\mathbf{v}_S(\mathbf{r}), \mathbf{v}_I(\mathbf{r}) \rightarrow 0$ as $|\mathbf{r}| \rightarrow \infty$, such that

$$\begin{aligned} \mathbf{v} &= \mathbf{v}_S + \mathbf{v}_I, \\ \nabla \cdot \mathbf{v}_S &= 0, & \nabla \cdot \mathbf{v}_I &= \nabla \cdot \mathbf{v}, \\ \nabla \times \mathbf{v}_S &= \nabla \times \mathbf{v}, & \nabla \times \mathbf{v}_I &= 0. \end{aligned}$$

Moreover, there exist unique potential functions $\psi(\mathbf{r}) \in \mathcal{C}^\infty(\mathbb{R}^n, \mathbb{R}^n)$, $\phi(\mathbf{r}) \in \mathcal{C}^\infty(\mathbb{R}^n)$ with $\psi(\mathbf{r}), \phi(\mathbf{r}) \rightarrow 0$ as $|\mathbf{r}| \rightarrow \infty$, such that

$$\begin{aligned} \mathbf{v}_S &= \nabla \times \psi \\ \mathbf{v}_I &= \nabla \phi. \end{aligned}$$

As we can see, the two components can be described using the scalar potential ϕ , and the vector potential ψ . For a two-dimensional field, e.g. in the xy -plane, ψ has only a component along the z axis: $\psi = \psi \mathbf{e}_z$. The representation using potentials is equivalent to the full knowledge of the vector field, and it amounts to represent a vector field with the two scalar functions $\phi(\mathbf{r})$ and $\psi(\mathbf{r})$.

The Helmholtz decomposition is not unique when the vector field \mathbf{v} is defined on a bounded regular domain D and the field does not go to zero on the boundary ∂D . In this case, the field has a *harmonic* component, which is both irrotational and solenoidal. A harmonic component can be represented as either the gradient of a scalar potential or the curl of a vector potential function, or some blend of the two. Sometimes, it is appropriate to separate this third harmonic component and to make the decomposition unique. For example, Braun and Hauck [10] proposed to decompose the solenoidal field into the "pure" solenoidal homogeneous component \mathbf{v}_{S_0} and the residual harmonic component \mathbf{v}_H ,

$$\mathbf{v}_S = \mathbf{v}_{S_0} + \mathbf{v}_H,$$

where \mathbf{v}_{S_0} is homogeneous in that its normal component is zero on the boundary (completely tangential). A similar decomposition can be applied to an irrotational vector component.

The Helmholtz decomposition will be used to derive the theoretical results in the sequel.

Chapter 3

Forward and Inverse Problems

In this chapter, we establish the mathematical framework for solving inverse problems in acoustic tomography, and this will be used as a basis in all subsequent developments. Section 3.1 gives the general formulation of an inverse problem. In Section 3.2, we describe a tomographic setup used for sensing a general inhomogeneous moving medium and list the possible inverse problems. Our ultimate goal is to obtain sound speed and velocity of the medium as a function of the position. To this end, we first define a set of data, acquired using sound propagation and acoustic tomography methods, that enables the reconstruction of the unknown parameters. Section 7.3 introduces the classical measurements used in acoustic tomography, namely the time-of-flight measurements, and shows that they are not sufficient to reconstruct the moving component of the medium. As a solution, in Section 3.4, an additional set of measurements related solely to the parameters of sound propagation, namely to the angle-of-departure and the angle-of-arrival of sound waves, is suggested. A new method to obtain these measurements is also proposed. In Section 3.5, important practical inverse problem scenarios are discussed, emphasizing the cases for which the required measurements can be reduced to only one of the two proposed sets. We will show that, on bounded domains, the classical time-of-flight measurements are sufficient to recover the sound speed and the moving component of the medium when the latter component is a divergence-free 2D vector. Conversely, the angle-of-departures/arrivals are sufficient to reconstruct the sound speed and the curl-free 2D velocity of the medium. Further, an iterative reconstruction algorithm is proposed in Section 3.6, and possible variations to the main scheme are discussed. Section 3.7 analyzes the reconstruction error and gives the Cramér-Rao lower bound for the time-of-flight estimation.

3.1 General formulation

Acoustic tomography is a type of inverse problem: specifically, the information brought by sound propagation through the field of interest is used to infer the local properties of the field. In the usual terminology of inverse problems, the set of parameters to be determined, which describes the state of the field, is called the model, \mathcal{M} . To obtain the information on the model parameters, measurements of some observable parameters are needed. The experimental

measurements are called the data, \mathcal{D} . In order to compute the model parameters, first the forward problem is defined by devising a mapping \mathcal{G} , that is non-linear in general, such that

$$\mathcal{D} = \mathcal{G}\mathcal{M}.$$

The inverse mapping

$$\mathcal{M} = \mathcal{G}^{-1}\mathcal{D}$$

is then constructed from the forward mapping.

Linearization Usually solving a non-linear problem is analytically hard and computationally intractable and thus forward problems are often linearized. Commonly, it is done by using the Taylor series expansion in terms of the models:

$$\mathcal{D} = \mathcal{G}\mathcal{M}_0 + \mathcal{G}_l(\mathcal{M} - \mathcal{M}_0) + \dots,$$

and keeping only the first order terms, so that:

$$\mathcal{D} - \mathcal{D}_0 = \mathcal{G}_l(\mathcal{M} - \mathcal{M}_0), \quad (3.1)$$

where $\mathcal{D}_0 = \mathcal{G}\mathcal{M}_0$, and \mathcal{G}_l is a linearized mapping around the unperturbed model \mathcal{M}_0 .

Discretization While inverse problems are often formulated in infinite dimensional spaces (or continuous domain), limitations to a finite number of measurements, and the practical consideration of recovering only a finite number of unknown parameters, usually lead to the problems being recast in discrete form. For example, suppose that the propagation medium can be adequately described by a set of \mathcal{M} parameters, m_1, m_2, \dots, m_M , and that there are N data, d_1, d_2, \dots, d_N . If the problem is as well linearized, then the forward problem can be written in the matrix form

$$\mathbf{d} = \mathbf{G}\mathbf{m}, \quad (3.2)$$

where \mathbf{d} and \mathbf{m} are column vectors whose elements are $d_i - d_{i_0}$ for $i = 1, \dots, N$ and $m_j - m_{j_0}$ for $j = 1, \dots, M$, and \mathbf{G} is an $N \times M$ matrix whose elements are

$$G_{ij} = \frac{\partial d_i}{\partial m_j}.$$

Equation (3.2) is the basic equation of our forward modeling and it is going to be studied in great detail.

3.2 Problem setup

We consider the tomographic setup illustrated in Figure 3.1. The region of interest is surrounded by acoustic transmitters and receivers. The transmitting elements are sequentially or simultaneously driven with transmit pulses that are emitted towards the receivers. While traveling from a transmitter to a receiver, the original signal interacts with the medium and it is modified by the time

the receiving elements are reached. In general, for each transmit pulse there is a set of received pulses, characterized with different shapes, amplitudes and delays. Comparison of the received signals with the transmit signals and the knowledge of the geometric setup (relative positions of the transducers) form the conceptual basis for interpreting the physical properties of the medium. In general, the medium is assumed to be inhomogeneous and moving.

In acoustic transmission tomography the signal sent from the transmitters and received by receivers after passing through the object of interest is generally used to produce two images, one based on the speed of sound (group velocity for the case of moving medium), and one based on the attenuation of sound. The reflection properties of the medium, imaged by the methods commonly called reflection tomography methods, are usually reconstructed from the time delays of later arriving signals (the signals scattered from the object). However, the attenuation and the reflection properties stay beyond the scope of this thesis. In this research, our specific goal, is to infer the sound speed c and the moving component \mathbf{v} of the medium. This problem is very general and covers a vast number of applications, some of which will be the subjects of our study. Towards the reconstruction of c and \mathbf{v} , we first suppose that the positions of the transducers are known. Some practical aspects of position calibration are discussed in Chapter 7. Also, the propagation of sound is modeled with the ray theory introduced in Section 2.1.

In the rest of this chapter, our goal is to define a set of data acquired by acoustic tomography that enables the reconstruction of c and \mathbf{v} . Particularly, we will show that the measurements of the time-of-flight and the angles-of-departure/arrival of the sound wave can be used for this purpose.

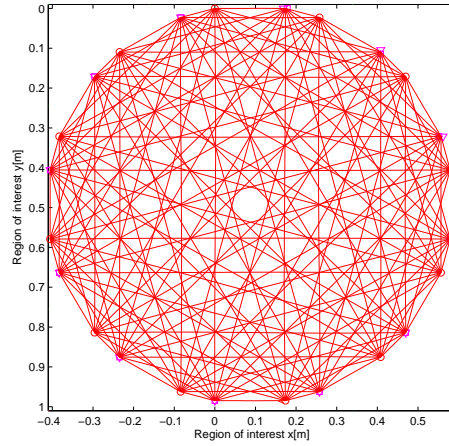


Figure 3.1: Problem setup. The region of interest is an inhomogeneous moving medium surrounded by acoustic transmitters and receivers. The ultimate goal is to find the sound speed and the moving component of the medium. The available data are the acoustic signals sent from every transmitter and received by every receiver.

3.3 Time-of-flight measurements

The time taken by a sound wave to propagate from a transmitter to a receiver is called *time-of-flight*. In this section, we discuss the possibility to reconstruct c and \mathbf{v} from time-of-flight measurements. We will show that, in general, these measurements are not sufficient to reconstruct the velocity field \mathbf{v} . We also present two techniques for estimating time-of-flights.

3.3.1 Longitudinal interaction

The time-of-flight from a transmitter to a receiver is equal to:

$$\tau = \int_{\Gamma} \frac{1}{u_g} ds = \int_{\Gamma} \frac{1}{(c\mathbf{n} + \mathbf{v}) \cdot \mathbf{s}} ds, \quad (3.3)$$

where u_g is the amplitude of the group velocity \mathbf{u}_g , \mathbf{s} is the unit vector tangent to the ray path Γ and also parallel to \mathbf{u}_g . Although not proved, we believe that the time-of-flights uniquely determine c and \mathbf{v} . Some evidences on this conjecture will be given in Section 3.4. However, since the relationship between τ , c , and \mathbf{v} is highly non-linear, it is rather impractical to choose (3.3) as the forward model. Instead, (3.3) is linearized as:

$$\begin{aligned} \tau &\simeq \int_{\Gamma} \frac{1}{c_0 \mathbf{n} \cdot \mathbf{s}} ds - \int_{\Gamma} \frac{(\Delta c \mathbf{n} + \mathbf{v}) \cdot \mathbf{s}}{(c_0 \mathbf{n} \cdot \mathbf{s})^2} ds \\ &\simeq \tau_0 - \frac{1}{c_0^2} \int_{\Gamma} (\Delta c \mathbf{n} + \mathbf{v}) \cdot d\mathbf{s}. \end{aligned}$$

c_0 is a reference sound speed (e.g. the spatial average sound speed), $\Delta c = c - c_0$, and Δc and $\|\mathbf{v}\|$ are typically much smaller than c_0 . Now, the time-of-flight perturbations are linearly related to Δc and \mathbf{v} ,

$$(\tau_0 - \tau) c_0^2 = \int_{\Gamma} (\Delta c \mathbf{n} + \mathbf{v}) \cdot d\mathbf{s}. \quad (3.4)$$

The line integral on the right-hand side of (3.4) will be called the longitudinal interaction l_{Γ} , by analogy with the line integrals of the vector field defined in [10],

$$l_{\Gamma} = \int_{\Gamma} (\Delta c \mathbf{n} + \mathbf{v}) \cdot d\mathbf{s}. \quad (3.5)$$

It is important to verify if from (3.5) we can uniquely compute the changes in c , and \mathbf{v} , or equivalently if l_{Γ} is sufficient for estimating c and \mathbf{v} . Unfortunately, it is not the case, as shown in the following example.

Example 3.3.1 (Invisible vector field). Assume a particular synthetic vector field $\mathbf{v}_1(\mathbf{r}) = \mathbf{r}$, and a particular measurement set up, as shown in Figure 3.2. The transmitters and the receivers are placed on a circle centered at the origin. For simplicity of exposure, c is assumed to be constant, i.e. $\Delta c = 0$. Using the previously proposed linearization, the time-of-flight between any two

points on the boundary ∂D are

$$\tau \simeq \int_{-L}^L \frac{1}{c_0} ds - \frac{1}{c_0^2} \int_{-L}^L \mathbf{v}_1 \cdot d\mathbf{s} = \frac{2L}{c_0} = \tau_0,$$

as the integral of an odd function over a symmetric interval is always equal to zero. Hence, the first order time-of-flight perturbations or equivalently the longitudinal interaction does not depend on this particular vector field and no information on the field can be obtained whatsoever. One could argue that a radial vector field of this type is not very realistic. However, in the linearized model, the perturbations τ_2 caused by any other “realistic” vector field \mathbf{v}_2 would not differ from the perturbations caused by $\mathbf{v}_2 + \mathbf{v}_1$, since \mathbf{v}_1 is shown to be an “invisible” vector field. Conversely, if we measure the time-of-flights τ_2 what is the underlying moving component? Now, it is clear that both \mathbf{v}_2 and $\mathbf{v}_2 + \mathbf{v}_1$ are the correct answers, and the inverse problem has no unique solution. More generally, we could interpret the longitudinal interaction as a linear function, and the invisible field as an element of the null space. Therefore, the solutions of the inverse problem can be expressed as the sum of a solution compatible with the measurements plus all the elements of the null space. To resolve this ambiguity we need more information. Again, the non-linear model provides more information since

$$\begin{aligned} \tau &= \int_{-L}^L \frac{1}{c_0 + \mathbf{v}_1 \cdot \mathbf{s}} ds = \int_{-L}^L \frac{1}{c_0 + s} ds \\ &= \log(c_0 + L) - \log(c_0 - L) \neq \tau_0, \end{aligned}$$

but it is of little practical interest, due to the difficulty in solving the non-linear inverse problem. \square

More formally, the limitations of the longitudinal interaction can be explained as follows. Applying the Helmholtz decomposition on \mathbf{v} in (3.5), and assuming for simplicity that $\Delta c = 0$, we have

$$\begin{aligned} l_\Gamma &= \int_\Gamma (\nabla\phi + \nabla \times \psi) \cdot d\mathbf{s} \\ &= \phi(\mathbf{x}_R) - \phi(\mathbf{x}_T) + \int_\Gamma \frac{\partial\psi}{\partial y} s_x - \frac{\partial\psi}{\partial x} s_y ds, \end{aligned}$$

where the latter equality comes from the gradient theorem, i.e. $\int_a^b \nabla f \cdot d\mathbf{s} = f(b) - f(a)$, and the reference system is as shown in Figure 2.1. Notice that, except for the boundary values $\phi(\mathbf{x}_R)$ and $\phi(\mathbf{x}_T)$, the longitudinal interaction does not give any information on the irrotational vector component $\phi(\mathbf{x})$.

3.3.2 Time-of-flight estimation techniques

Time delay estimation, which serves as the first stage that feeds into subsequent processing blocks of a system has the most significant importance for the reconstruction. Due to its importance in many fields, this area has made remarkable advances in the past few decades.

In the time-of-flight estimation problem, we can either estimate the absolute time-of-flight or the difference with respect to the arrival of any reference signal.

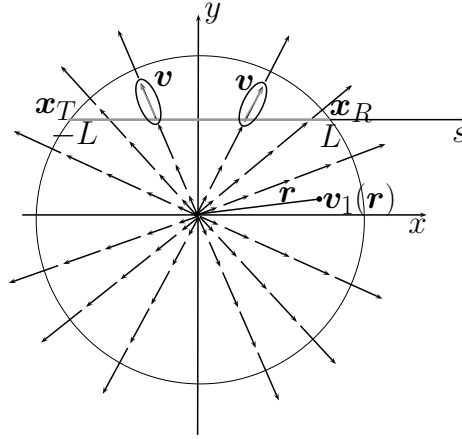


Figure 3.2: Example of an “invisible” vector field, $v_1(\mathbf{r}) = \mathbf{r}$. The transmitters and the receivers are placed on a circle centered at the origin. The longitudinal interaction between any two points on the boundary \mathbf{r}_T and \mathbf{r}_R sums up to zero, and bears no information on \mathbf{v} . The field \mathbf{v} is “invisible” to the longitudinal interaction (i.e. in the linearized model).

The reference signal can be a signal sent through a known or controlled medium, for example a room with a uniform known temperature, or through water also with a uniform and known temperature. The correct time-of-flight will be then equal to the sum of the difference and the reference time-of-flight. Intuitively, estimating the difference of the time-of-flight is an easier problem because the systematic error that can appear when estimating the absolute time can be avoided. For example, the delays of the transducers, all electronic delays, and the transducers positions, although carefully taken into account, are never perfectly estimated and they are potential sources of the systematic error. However, the same systematic error appears in the time-of-flight of the reference signal, and it is going to be canceled when the difference between these two time-of-flights is computed. Whenever the specific problem nature offers the possibility of having the reference signal, its use can only improve the time-of-flight estimation. However, in some cases, we are not given any reference signal and the absolute time-of-flight has to be computed.

In the following, we are going to present two methods for the time-of-flight estimation. These methods will be later used in the application part of the thesis.

Cross-correlation method Suppose a signal $x(t)$ is sent by a transmitter. The received signal can be represented as a series of delayed versions of $x(t)$:

$$y(t) = a_1x(t - \tau_1) + a_2x(t - \tau_2) + \dots + a_Nx(t - \tau_N) + n(t),$$

where $n(t)$ is noise. Each term on the right represents a separate ray path caused by signal reflection or refraction. The amplitudes a_i depend upon the

gain of the system, absorption, and reflection losses. The received signal $y(t)$ is cross-correlated with the transmitted signal $x(t)$. Assuming that the signal and the noise are mutually uncorrelated, the cross correlation $R_{xy}(\tau)$ is

$$R_{xy}(\tau) = \int x(t)y(t + \tau) dt = \sum_{i=1}^N a_i R_x(\tau - \tau_i).$$

We see that the cross correlation consists of a series of delayed versions of the autocorrelation of $x(t)$. Provided that the width of the main lobe of R_x is smaller than the difference between any of the τ_i 's, each arrival will appear as a separate peak in $R_{xy}(\tau)$, with amplitude proportional to a_i . It can be shown that the width of the autocorrelation envelope equals twice the reciprocal of the signal bandwidth. As we are interested in the first arrival of the signal, the position of the first peak of the cross-correlation determines the time-of-flight.

In practice, the signal we received is never a delayed version of the signal we sent. On its way to the receiver, the signal is first convolved with the transfer function of the transmitter, then the channel (region of interest) and finally the receiver transfer function. These transfer functions are usually not available and their non-linearity complicates additionally the time-of-flight estimation. These problems can be partially overcome if instead of using the source signal $x(t)$ the cross-correlation is computed as the convolution of $y(t)$ and the reference signal. In this case the peak of the cross-correlation determines the time-of-flight difference between the actual signal and the reference signal. The systematic error is then avoided. However, highly heterogeneous medium causes the signal to be refracted, which results in having close peaks of the cross-correlation, no matter whether the source or the reference signal is used.

First arrival method This is a very simple method for time-of-flight estimation. It basically analyzes the received signal from the moment the transmission starts and it determines the time-of-flight as the instant at which the received signal power increases the noise level. To detect this point one can setup an amplitude threshold or use different statistical methods, as the one proposed in [40].

However, the beginning of the signal usually contains the part related to the transducers' transition bandwidth or the ringing of the transducers. Namely, the transducers do not respond instantaneously to the excitation but only after the transition period. Then, it becomes difficult to detect the signal starting point. Having a reference signal now permits not to search for the beginning of the signal but for the first significant peak, as shown in Figure 3.3. This point is easier to detect in case the received signal is attenuated, and has a low SNR. In Chapters 5 and 6, we will show that when the medium is highly heterogeneous this simple method outperforms the cross-correlation method.

3.4 Angle-of-departure/arrival measurements

In the past, several researches working in the field of fluid tomography came to the conclusion that the time-of-flight measurements are not sufficient for the vector field reconstruction [34, 50, 10]. In [10], the authors proposed a

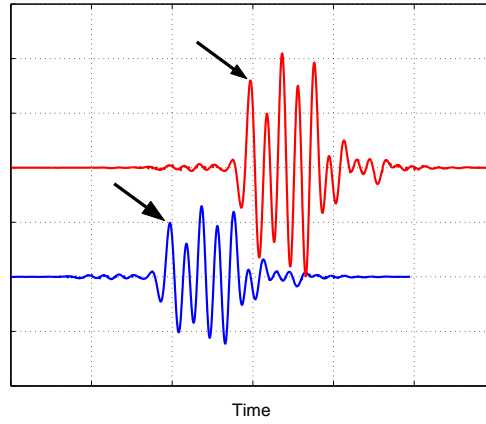


Figure 3.3: The signal and the reference. It is hard to determine the beginning of the signals. Since we are interested only in the time-of-flight difference we can compute the difference by comparing any other two points, chosen to be the corresponding signal markers, for example the first significant peaks.

new set of measurements called the *transversal* interaction, which together with the longitudinal interaction allows to recover both the solenoidal and the irrotational components of a vector field. To obtain the transversal interaction, an optical Schlieren technique is proposed. However, that is only practical in rather specialized setups having an optical access. We suggest a new method for estimating the transversal interaction based solely on acoustic measurements.

In this section, we first show in what sense the transversal interaction complements the longitudinal interaction. Then, we suggest a method to obtain the transversal component by measuring the angle-of-departure and the angle-of-arrival of the sound wave, and propose two techniques to estimate these angles.

3.4.1 Transversal interaction

The transversal interaction corresponds to the integration of the normal component of the vector field along the propagation path

$$t_{\Gamma} = \int_{\Gamma} \mathbf{v} \cdot d\mathbf{s}_{\perp},$$

and it provides the information on the irrotational component of the vector field since

$$\begin{aligned} t_{\Gamma} &= \int_{\Gamma} (\nabla\phi + \nabla \times \boldsymbol{\psi}) \cdot d\mathbf{s}_{\perp} \\ &= -\psi(\mathbf{r}_R) + \psi(\mathbf{r}_T) + \int_{\Gamma} \frac{\partial\phi}{\partial y} s_x - \frac{\partial\phi}{\partial x} s_y ds. \end{aligned}$$

Now, we need a method to obtain the transversal interaction. Let us first slightly modify the definition of the transversal interaction in order to take into

account the sound speed field as well:

$$t_\Gamma = \int_\Gamma (\Delta c \mathbf{n} + \mathbf{v}) \cdot d\mathbf{s}_\perp.$$

Notice that the total speed along the trajectory is tangent to the trajectory, hence, in every point

$$(c_0 \mathbf{n} + \Delta c \mathbf{n} + \mathbf{v}) \cdot \mathbf{s}_\perp = 0.$$

The transversal component can thus be written as

$$t_\Gamma = -c_0 \int_\Gamma \mathbf{n} \cdot d\mathbf{s}_\perp.$$

In order to estimate t_Γ we need to know $\mathbf{n} = (\cos \theta \ \sin \theta)^T$ along the trajectory Γ (see Figure 2.1). In a first approximation, it can be supposed that \mathbf{n} is constant along Γ which is true when c and \mathbf{v} are uniform [64]. Then,

$$\begin{aligned} t_\Gamma &= c_0 \int_\Gamma \begin{pmatrix} \cos \theta \\ \sin \theta \end{pmatrix} \cdot (\mathbf{s} \times \mathbf{e}_z) ds \\ &\simeq c_0 (\cos \theta (y_R - y_T) - \sin \theta (x_R - x_T)), \end{aligned} \quad (3.6)$$

where $\mathbf{s}_\perp = -\mathbf{s} \times \mathbf{e}_z$, and t_Γ can be approximately computed if we know the angle θ and the exact position of the transmitter and the receiver. A better approximation of t_Γ can be obtained if we take $\theta = (\theta_T + \theta_R)/2$ where θ_T and θ_R are the corresponding angles at the transmitter and the receiver side respectively. Also, an improvement can be achieved if we assume that Γ is known (e.g. from the previous iteration) and the vector \mathbf{n} changes linearly from \mathbf{n}_T at the transmitter side to \mathbf{n}_R at the receiver side. The angles θ_T and θ_R can be estimated from the angle-of-departure and angle-of-arrival of the sound wave, as explained in the following.

Assume we want to measure the angle θ_R . This angle can be estimated from \mathbf{n}_R that is found as:

$$\mathbf{n}_R = \frac{\mathbf{u}_g - \mathbf{v}}{\|\mathbf{u}_g - \mathbf{v}\|}. \quad (3.7)$$

The group velocity \mathbf{u}_g can be found using the acoustic tripole, as follows. We measure the time-of-flight for R0-R2, and set $\Delta t_1 = \tau_{R1} - \tau_{R0}$ and $\Delta t_2 = \tau_{R2} - \tau_{R0}$, where τ_{R_i} is the time-of-flight measured at the receiver R_i . Then, it holds that

$$\mathbf{u}_g \cdot \mathbf{p}_1 = \|\mathbf{u}_g\|^2 \Delta t_1 \quad (3.8)$$

$$\mathbf{u}_g \cdot \mathbf{p}_2 = \|\mathbf{u}_g\|^2 \Delta t_2 \quad (3.9)$$

where \mathbf{p}_1 and \mathbf{p}_2 are shown in Fig. 3.1. Each of the previous equation is the acoustic dipole equation. We need two of them as the speed \mathbf{u}_g is unknown. From (3.8) and (3.9) we can find \mathbf{u}_g . The same configuration of the acoustic tripole can be used to measure the local wind \mathbf{v} at the receiver side. This can be done using the principles of the sonic anemometer [17]. Once \mathbf{u}_g and \mathbf{v} are estimated, we can compute \mathbf{n}_R and the angle θ_R from (3.7). The method dual to this one can be used to measure the angle θ_T . In this case, we would use the time-of-flights from the transmitters T0-T2 (see Figure 3.1).

It is important to notice that in order to take full advantage of this additional set of measurements, the bent ray model of sound propagation needs to be considered.

At this point, it is worth adding that the approximation in (3.6) might seem to be too rough but in our iterative reconstruction algorithm (see Section 3.6) this approximation will only be applied to the error fields, and only the difference between \mathbf{n} and its current estimate $\hat{\mathbf{n}}$ is assumed to be constant. The error introduced by the approximation will be evaluated in Section 4.2.1.

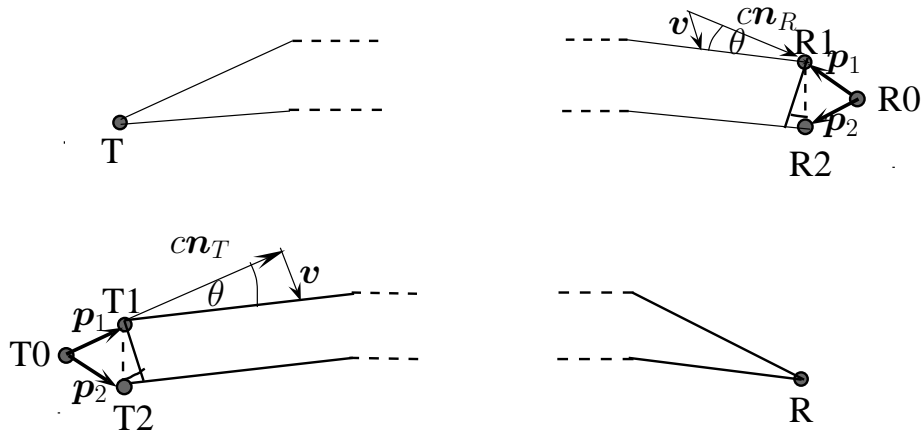


Figure 3.4: The vectors \mathbf{n}_T and \mathbf{n}_R can be estimated by measuring the angle-of-departure and the angle-of-arrival of the sound wave and by measuring \mathbf{v} locally at the transmitter or the receiver side. Both the angle-of-departure/arrival and the local wind measurements are measured using the acoustic tripole (i.e. T0-T2 and R0-R2).

As we can see, the time-of-flights can be used to estimate the angle-of-departure/arrival measurements. These two sets then allow for full reconstruction of a vector field. Thus, we conjecture that in the non-linear model in (3.3) the time-of-flight measurements uniquely recovers both the scalar and the vector fields.

3.5 Important practical cases

The longitudinal and the transversal interactions together uniquely determine the sound speed and the moving component and they both can be estimated by measuring the parameters of sound propagation. The correct general formulation of the forward problem is then

$$l_\Gamma = \int_\Gamma (\Delta c \mathbf{n} + \mathbf{v}) \cdot d\mathbf{s} \quad (3.10a)$$

$$t_\Gamma = \int_\Gamma (\Delta c \mathbf{n} + \mathbf{v}) \cdot d\mathbf{s}_\perp. \quad (3.10b)$$

In the following, important practical scenarios will be discussed emphasizing the situations in which the set of measurements can be reduced to either (3.10a) or (3.10b). All the cases are going to consider the physical fields on a bounded region, where in practical setups the boundary represent the closed curve on which the sources and receivers reside.

3.5.1 Sound speed estimation in the scalar case

When there is no moving component in the medium, the sound speed can be estimated from any of the two equations in (3.10), and actually the problem reduces to a scalar tomography problem. However, the sound speed should be preferably estimated from the longitudinal interaction, since the time-of-flight measurements are directly related to the longitudinal interaction, while the angle-of-departure/arrival measurements are related to the transversal interaction by approximated relations.

Obviously, if the time-of-flights are used to solve the scalar tomography problem, the transversal component is not needed. However, the angle-of-departure and the angle-of-arrival measurements can still be useful because they convey information on the sound trajectories that depend on the underlying speed of sound. Therefore, this set can possibly be used in addition to the time-of-flights to increase precision.

3.5.2 2D projection of a 3D solenoidal vector field

The following practical cases all refer to special cases of vector field since the sound speed estimation was shown to be an “easy” problem. Also, they all consider the fields on a bounded region, where in practical setups the boundary refers to the closed curve on which the sources and receivers reside.

A usual situation in practice is that the 2D vector field to be reconstructed is obtained by taking out a slice from a 3D solenoidal vector field. The examples include the velocity field of incompressible fluid flow, like the wind field in the atmosphere or flow fields in liquids. However, since the flow leaves and enters the slice, the assumption of the absence of the sources is not valid anymore. Indeed, it is easy to see that the solenoidal condition for a 3D vector field, in general does not extend to any of its 2D slices. For example, if

$$\nabla \cdot \mathbf{v} = 0,$$

then in the xy -plane we have

$$\nabla \cdot \mathbf{v}_{xy} = \frac{\partial v_x}{\partial x} + \frac{\partial v_y}{\partial y} = -\frac{\partial v_z}{\partial z} \neq 0. \quad (3.11)$$

Hence, we conclude that in this case both l_Γ and t_Γ are needed for the reconstruction and no simplification can be made.

3.5.3 Horizontal slice in the stratified atmosphere

In the atmosphere there is a usual stratification caused by gravity, and, as a rule, the horizontal component of wind field \mathbf{v}_{xy} is greater than the vertical component v_z by a factor of 10 – 100. This gives a possibility to assume

sometimes that $v_z = 0$. More precisely, the vertical component is commonly neglected for temporarily average wind data in micrometeorological studies and if the influence of mesoscale vertical advection (e.g. convection) is neglected. Hence, by inserting this assumption into (3.11) the source-free condition in the horizontal plane will now be satisfied, i.e. $\nabla \cdot \mathbf{v}_{xy} = 0$, and the wind field \mathbf{v}_{xy} can be approximated with a solenoidal field.

We have seen that the longitudinal interaction contains the information on the solenoidal wind field and the problem seems to be solved. However, recall that bounded domains admit harmonic fields that can be seen both as solenoidal or irrotational. For example, Braun and Hauck [10] proposed to decompose the solenoidal field into the “pure” solenoidal homogeneous component \mathbf{v}_{S_0} and the residual harmonic component \mathbf{v}_H ,

$$\mathbf{v}_S = \mathbf{v}_{S_0} + \mathbf{v}_H,$$

where \mathbf{v}_{S_0} is homogeneous in that its normal component is zero on the boundary (completely tangential). In their solution, derived from the original inverse Radon transform, it is shown that in the case of a circular geometry setup the obtained result consists of \mathbf{v}_{S_0} and only one half of \mathbf{v}_H . The problem that the harmonic field is reconstructed with only one half of its magnitude can be further treated by reapplying the same inversion in order to achieve the correct reconstruction. However, the harmonic component will be imaged differently in different geometry setups and the successful reconstruction might not be always possible. Another more general approach was suggested by Norton [50]. He showed that the measurements of the normal component of \mathbf{v}_S taken on the boundary of the region can be used to resolve the ambiguity of the harmonic part. However, we are going to show that no additional measurements are required in order to determine the solenoidal vector field on the bounded domain.

3.5.4 Solenoidal vector fields on bounded domains

In order to show that, on bounded domains, the time-of-flights are sufficient to determine the solenoidal vector field, it suffices to prove that the time-of-flights (in terms of the line-integrals) uniquely represent the field. This result is stated in the following theorem.

Theorem 3.1 (Solenoidal vector fields). The solenoidal vector field \mathbf{v} in a bounded simply connected domain D is uniquely determined from the longitudinal interaction through D .

Proof: Assume that there exist two different solenoidal vector fields \mathbf{v} and \mathbf{u} with the same line integrals through D ,

$$\int_{\Gamma} \mathbf{v} \cdot d\mathbf{s} = \int_{\Gamma} \mathbf{u} \cdot d\mathbf{s}, \quad \text{for all } \Gamma \text{ in } D. \quad (3.12)$$

Applying the 2D version of the Stoke’s theorem on the difference field $(\mathbf{v} - \mathbf{u})$

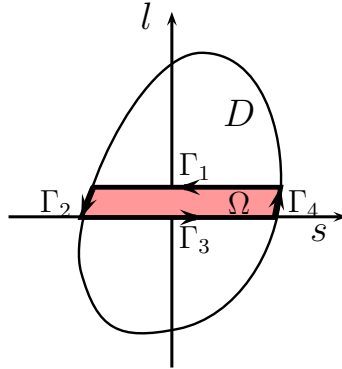


Figure 3.5: Solenoidal vector field in a bounded domain D is uniquely determined from its line integrals taken over D .

and taking $\Gamma = \partial\Omega$ for any $\Omega \in D$ we have

$$\begin{aligned} \oint_{\partial\Omega} (\mathbf{v} - \mathbf{u}) \cdot d\mathbf{s} &= \iint_{\Omega} \nabla \times (\mathbf{v} - \mathbf{u}) \cdot \mathbf{e}_z \, ds \, dl \\ \oint_{\partial\Omega} \mathbf{v} \cdot d\mathbf{s} - \oint_{\partial\Omega} \mathbf{u} \cdot d\mathbf{s} &= \iint_{\Omega} \nabla \times (\mathbf{v} - \mathbf{u}) \cdot \mathbf{e}_z \, ds \, dl. \end{aligned} \quad (3.13)$$

The left hand side of (3.13) is identically equal to zero by the hypothesis in (3.12), since the corresponding line integrals along Γ_1 through Γ_4 (see Figure 3.5) are equal. Taking the derivative over l (note that Ω can change with l , e.g. by fixing Γ_3 and moving $\Gamma_1(l)$ in the vertical direction), we get

$$0 = \int_{\Gamma_1} \nabla \times (\mathbf{v} - \mathbf{u}) \cdot \mathbf{e}_z \, ds. \quad (3.14)$$

In the previous equation, $\nabla \times (\mathbf{v} - \mathbf{u}) \cdot \mathbf{e}_z$ is a scalar value and does not depend on the mutual orientation of Γ and $\mathbf{v} - \mathbf{u}$. Therefore, (3.14) coincides with the Radon transform of this value and since it is always zero we can conclude that the value itself is identical to zero almost everywhere,

$$\nabla \times (\mathbf{v} - \mathbf{u}) = 0.$$

Hence,

$$\mathbf{v} - \mathbf{u} = \nabla\varphi$$

almost everywhere, for some potential function φ defined on D . Then, it also holds that

$$0 = \int_{\Gamma} (\mathbf{v} - \mathbf{u}) \cdot d\mathbf{s} = \int_{\Gamma} \nabla\varphi \cdot d\mathbf{s} = \varphi(\mathbf{r}_R) - \varphi(\mathbf{r}_T).$$

Here, Γ is arbitrary, which leads to the conclusion that

$$\varphi = \text{const.} \quad \text{on } \partial D.$$

Also, the field $\nabla\varphi$ is by construction irrotational and since it represents the

difference of the two solenoidal fields, it is also solenoidal. These two conditions are satisfied only when the field is a harmonic field. The harmonic fields on D , satisfies the solutions of the Laplace equation, and they are uniquely determined by its boundary values. Therefore,

$$\varphi = \text{const.} \quad \text{on } D,$$

and then

$$\nabla\varphi = 0 \quad \text{on } D,$$

proves that $\mathbf{v} = \mathbf{u}$, and the solenoidal field \mathbf{v} is uniquely determined from its line integrals. ■

The above theorem demonstrates that the line integrals contain sufficient information for the reconstruction of solenoidal vector fields. Although, we show that the transform is injective and therefore, the inverse transform exists, we do not provide the explicit inversion formula. Instead, we are going to use algebraic reconstruction methods to reconstruct the unknown field. These methods will be discussed in Section 4.2.

3.5.5 Irrotational vector fields on bounded domains

It is possible to draw an analogy between the previous case and the case of irrotational vector fields observed on bounded domains.

Theorem 3.2 (Irrotational vector fields). The irrotational vector field \mathbf{v} in a bounded simply connected domain D is uniquely determined from the transversal interaction t_Γ through D .

Proof: Assume that there exist two different irrotational vector fields \mathbf{v} and \mathbf{u} with the same t_Γ integrals through D ,

$$\int_\Gamma \mathbf{v} \cdot d\mathbf{s}_\perp = \int_\Gamma \mathbf{u} \cdot d\mathbf{s}_\perp, \quad \text{for all } \Gamma \text{ in } D.$$

Because the fields are irrotational, we have:

$$\mathbf{v} = \nabla\phi_1,$$

$$\mathbf{u} = \nabla\phi_2,$$

and the transversal interaction can be rewritten as:

$$\begin{aligned} \int_\Gamma \mathbf{v} \cdot d\mathbf{s}_\perp &= \int_\Gamma \nabla \times \phi_1 \mathbf{e}_z \cdot d\mathbf{s} = \int_\Gamma \mathbf{v}' \cdot d\mathbf{s} \\ \int_\Gamma \mathbf{u} \cdot d\mathbf{s}_\perp &= \int_\Gamma \nabla \times \phi_2 \mathbf{e}_z \cdot d\mathbf{s} = \int_\Gamma \mathbf{u}' \cdot d\mathbf{s}. \end{aligned}$$

It then also holds that

$$\int_\Gamma \mathbf{v}' \cdot d\mathbf{s} = \int_\Gamma \mathbf{u}' \cdot d\mathbf{s} \quad \text{for all } \Gamma \text{ in } D.$$

Applying the results from Theorem 3.1, we have $\mathbf{v}' = \mathbf{u}'$ and

$$\nabla \times \phi_1 \mathbf{e}_z = \nabla \times \phi_2 \mathbf{e}_z.$$

From the previous equation it also holds that

$$\nabla \phi_1 = \nabla \phi_2 \quad \Rightarrow \quad \mathbf{v} = \mathbf{u}.$$

■

The theorem proves that the transversal interaction uniquely determines an irrotational vector field on a bounded region and it can be useful in case we are specifically interested only in the irrotational vector component.

3.6 Reconstruction algorithm

So far, we have used continuous transforms, e.g. the Radon transform, on which we could choose to apply continuous inversions, e.g. the inverse Radon transform, the Fourier slice theorem, back projection etc. However, the Radon transform assume the knowledge of the line integrals of the unknown function for all the lines and all the directions. Even its discrete version requires a large number of projections with a special geometric setup, for example, the projections have to be uniformly distributed over 180° or 360° , in order to produce the results with a reasonable accuracy. An entirely different approach for tomographic reconstruction consists of first assuming that the measured field can be represented by an array of \mathcal{M} parameters m_1, m_2, \dots, m_M , and then setting up a linear set of equations for the unknowns in terms of \mathcal{D} , i.e. the measured data d_1, d_2, \dots, d_N . Then the forward problem in (3.1) can be formulated as in (3.2), that we repeat here:

$$\mathbf{d} = \mathbf{G}\mathbf{m}. \quad (3.15)$$

The previous equation represents the discretized version of (3.10), that is, the sampled version of l_Γ and t_Γ represent the measurements \mathbf{d} , while \mathbf{m} contains the parameters of sound speed c and medium velocity \mathbf{v} . Also, the trajectories used to model the sound propagation are implicitly inside \mathbf{G} .

3.6.1 Linear versus non-linear tomography algorithm

In the context of (3.2) we can define two problems. In *linear tomography*, we are given \mathbf{G} and \mathbf{d} , and the objective is to determine \mathbf{m} . The assumption here is that the ray paths are known *a priori*. Typically, they are assumed to be straight lines. In *non-linear tomography*, we are given only the observation \mathbf{d} , and the goal is to infer \mathbf{m} and incidently \mathbf{G} . Non-linear tomography inversion is required in problems with large medium inhomogeneities and/or medium speed. In this case, the ray trajectories are bent but they are not known before the inversion begins. In non-linear tomography, an iterative algorithm is needed to find the solution. The iterations alternate between estimating the sound speed and the moving component, and computing the trajectories [64]. The basic structure of such an algorithm is given in Algorithm 3.1.

¹It is also possible to solve the system $\hat{\mathbf{G}}\mathbf{m}^{i+1} = \mathbf{d}$

Algorithm 3.1: Non-linear tomography

1. Set the iteration $i = 0$ and \mathbf{m}^i as an initial model (a constant or the previously best-known model).
2. Compute the trajectories $\hat{\Gamma}$, matrix $\hat{\mathbf{G}}$ and the measurements $\hat{\mathbf{d}}$ for the current model \mathbf{m}^i .
3. Set $\Delta\mathbf{d} = \mathbf{d} - \hat{\mathbf{d}}$. If $\Delta\mathbf{d}$ is sufficiently small, stop.
4. Find the corrections $\Delta\mathbf{m}$ as the solution of the linear system of equations¹:

$$\hat{\mathbf{G}}\Delta\mathbf{m} = \Delta\mathbf{d}. \quad (3.16)$$
5. Update the current version of the model as $\mathbf{m}^{i+1} = \mathbf{m}^i + \Delta\mathbf{m}$.
6. Set $i = i + 1$ and go to step 2.

Analyzing Algorithm 3.1 we see that there are only two significant calculations: the solution of the forward problem (step 2); and the computation of the corrections of the parameters (step 4). Step 2 should not introduce any instability, since it can be performed essentially as accurately as the computing budget permits. Step 4, on the other hand, is crucial for the stability of the algorithm, and it is the main step both in the linear and non-linear tomography. The desired solution to the inverse problem will not in general be the simple matrix inversion because either: i) not all of the data are linearly independent, and/or ii) not all of the models are linearly independent. The latter indicates that there are multiple solutions to the same data set and the results of the theoretical analysis carried in Section 3.5 should be used to choose the proper data sets and the proper model to avoid this case. Additionally, the matrix \mathbf{G} might be poorly conditioned, and noisy data may prevent from finding the exact solution to the system in (3.2). There is a vast area of research on inverse methods trying to deal with all these problems. In Chapter 4, we are also going to concentrate more on inverting the linear system of equations (as the one in (3.15)) that arises in different tomographic problems.

3.7 Error analysis

Several technical aspects influence the performance of the tomographic reconstruction. The most important are:

1. The SNR in the raw signal,
2. The accuracy of the time-of-flight measurements, and the angle-of-departure and the angle-of-arrival measurements;
3. The accuracy of the distance measurement between the transmitters and receivers;
4. The coverage of the area by sound rays (the number of emitters and receivers and their locations);

5. The resolving power of the inversion method.

Applying different methods for the time-of-flight estimation and different inversion algorithms our efforts can directly affect the second and the last error cause. The use of the reference signal in the time-of-flight estimation can partially suppress the systematic error in the transducer positions, as it will be pointed in Section 5.3.2. Possible super-resolution techniques can improve the reconstruction in the context of the fourth aspect.

Even though the reconstruction accuracy depends on many factors, considering the problem as a parameter estimation problem helps to understand better the error. The parameter estimation problem is to determine a set of parameters \mathbf{m} from a set of noisy observations \mathbf{D} (we use capital letters for random quantities). Assume that from \mathbf{D} the parameters \mathbf{m} are estimated by applying an inverse mapping \mathbf{G}^\dagger as:

$$\hat{\mathbf{M}} = \mathbf{G}^\dagger \mathbf{D}. \quad (3.17)$$

where $\hat{\mathbf{M}}$ are the estimates of \mathbf{m} . Since the measurements are noisy, $\hat{\mathbf{M}}$ is also a random quantity. The estimation error is defined as the difference between the actual parameters and its estimates,

$$\mathbf{E} = \mathbf{m} - \hat{\mathbf{M}}.$$

The error is a random quantity as well, and, for example, the mean-squared error is given by $E[\mathbf{E}^T \mathbf{E}]$. The mean-squared error matrix, or the error-error covariance matrix is $\mathbf{R}_E = E[\mathbf{E} \mathbf{E}^T]$. On the main diagonal, its entries are the mean-squared estimation errors for each component of the parameter vector, whereas the off-diagonal terms express the correlation between the errors. The mean-squared estimation error $E[\mathbf{E}^T \mathbf{E}]$ equals the trace of the error-error covariance matrix, $\text{tr}[\mathbf{R}_E]$.

From (3.17), the error-error covariance matrix \mathbf{R}_E is

$$\begin{aligned} \mathbf{R}_E &= E[(\mathbf{m} - \mathbf{G}^\dagger \mathbf{D})(\mathbf{m} - \mathbf{G}^\dagger \mathbf{D})^T] \\ &= \underbrace{(\mathbf{m} - \mathbf{G}^\dagger \mathbf{d}_0)(\mathbf{m} - \mathbf{G}^\dagger \mathbf{d}_0)^T}_{\text{model mismatch}} + \underbrace{E[\mathbf{G}^\dagger \mathbf{N} \mathbf{N}^T \mathbf{G}^{\dagger T}]}_{\text{noise}}, \end{aligned}$$

where $\mathbf{D} = \mathbf{d}_0 + \mathbf{N}$, with \mathbf{N} being the zero mean noise that is uncorrelated with the data and the model. The advantage of this analysis is that now the error can be divided into the error from the model mismatch

$$(\mathbf{m} - \mathbf{G}^\dagger \mathbf{d}_0)(\mathbf{m} - \mathbf{G}^\dagger \mathbf{d}_0)^T \quad (3.18)$$

and the error from the noise,

$$E[\mathbf{G}^\dagger \mathbf{N} \mathbf{N}^T \mathbf{G}^{\dagger T}] = \mathbf{G}^\dagger \mathbf{R}_N \mathbf{G}^{\dagger T}. \quad (3.19)$$

The term in (3.18) vanishes when there exist a perfect model \mathbf{G} , such that $\mathbf{G} \mathbf{m} = \mathbf{d}_0$ and $\mathbf{G}^\dagger \mathbf{G} = \mathbf{I}$. In reality, this is rarely the case but the gap between the model and the reality decreases as the number of transmitters and receivers and consequently the estimation resolution increases. When the model mismatch is present, this term can be evaluated if we assume that \mathbf{m} is

a random vector, and that we know the correlation function of the unknown fields \mathbf{R}_m . Then, we can estimate the model mismatch as

$$E[(\mathbf{M} - \mathbf{G}^\dagger \mathbf{D}_0)(\mathbf{M} - \mathbf{G}^\dagger \mathbf{D}_0)^T] = \mathbf{R}_M - \mathbf{R}_{MD_0} \mathbf{G}^{\dagger T} - \mathbf{G}^\dagger \mathbf{R}_{MD_0}^T + \mathbf{G}^\dagger \mathbf{R}_{D_0} \mathbf{G}^{\dagger T}. \quad (3.20)$$

Even though \mathbf{R}_M is usually unknown, certain models can be assumed as suggested in [75].

The term in (3.19) corresponds to the error in estimating the longitudinal and the transversal component. Assuming that the noise components are uncorrelated and that $\mathbf{N}^T = (\mathbf{N}_l^T \mathbf{N}_t^T)$, where \mathbf{N}_l and \mathbf{N}_t are the noise in the longitudinal and the transversal components respectively, we have

$$\mathbf{R}_N = E\left[\begin{pmatrix} \mathbf{N}_l \\ \mathbf{N}_t \end{pmatrix} (\mathbf{N}_l^T \mathbf{N}_t^T)\right] = \text{diag}[\sigma_l^2, \dots, \sigma_l^2, \sigma_t^2, \dots, \sigma_t^2].$$

The off-diagonal terms are zero because the noise components \mathbf{N}_l and \mathbf{N}_t are uncorrelated. In the following, we analyze the terms σ_l^2 and σ_t^2 . After estimating \mathbf{R}_N , the complete term $\mathbf{G}^\dagger \mathbf{R}_N \mathbf{G}^{\dagger T}$ needs to be computed for a specific practical setup and a specific inversion method that determine \mathbf{G}^\dagger .

3.7.1 Error in the longitudinal interaction

It follows from (3.4) that the variance of the longitudinal interaction depends on the variances of τ , τ_0 and c_0 . The average or the reference time-of-flight τ_0 can be either measured before the main experiment or computed as:

$$\tau_0 = \frac{\|\mathbf{r}_T - \mathbf{r}_R\|}{c_0}. \quad (3.21)$$

We first suppose that τ_0 is estimated with the same techniques as τ . In that case, it can be assumed that $\sigma_\tau^2 = \sigma_{\tau_0}^2$, and from (3.4) we have:

$$\sigma_l^2 = 2c_0^4 \sigma_\tau^2 + 4(\tau_0 - \tau)^2 c_0^2 \sigma_{c_0}^2.$$

In the second case, the error in τ_0 originates from the error in the distance $\mathbf{r}_T - \mathbf{r}_R$, and the error in c_0 . The longitudinal interaction can be written as:

$$l_\Gamma = \left(\frac{\|\mathbf{r}_T - \mathbf{r}_R\|}{c_0} - \tau \right) c_0^2 = \|\mathbf{r}_T - \mathbf{r}_R\| c_0 - \tau c_0^2$$

from which we compute the variance as

$$\sigma_l^2 = 2c_0^2 \sigma_p^2 + c_0^4 \sigma_\tau^2 + \|\mathbf{r}_T - \mathbf{r}_R\|^2 \sigma_{c_0}^2. \quad (3.22)$$

It is also assumed that the error variances of \mathbf{r}_T and \mathbf{r}_R are both equal to σ_p^2 , and the approximation $\tau c_0 \simeq \|\mathbf{r}_T - \mathbf{r}_R\|$ is used. Depending on the transducers type, the ambiguity in defining the center of the transmission may vary from 1 mm to 50 mm, resulting in σ_p

$$\text{from } \sigma_p = 10^{-3} \text{ m up to } \sigma_p = 5 \cdot 10^{-2} \text{ m.}$$

To estimate σ_τ^2 we use the Cramér-Rao lower bound. This bound determines

the lower bound for σ_τ^2 and it is actually achieved when the time-of-flight is estimated from the peak of the cross-correlation between the sent and the received signal. In [77], it is computed that:

$$\sigma_\tau^2 \geq \frac{1}{8\pi^2} \frac{1}{\text{SNR}} \frac{1}{T_o B} \frac{1}{f_c^2} \frac{1}{(1 + B^2/12f_c^2)}, \quad (3.23)$$

where SNR is the signal-to-noise ratio, T_o the observation time, f_c the central frequency and B the signal bandwidth. If we change the parameters in (3.23) with the one that we use in our experiments [36], that are $T_o = 2 \text{ ms}$, $f_c = 40 \text{ kHz}$, $B = 2 \text{ kHz}$ and for the two cases of SNR, we get

$$\begin{aligned} \text{SNR} = 30\text{dB} &\longrightarrow \sigma_\tau \simeq 4.4 \cdot 10^{-8} \text{ s}, \\ \text{SNR} = 10\text{dB} &\longrightarrow \sigma_\tau \simeq 4.4 \cdot 10^{-7} \text{ s}. \end{aligned}$$

We can conclude that σ_p is relatively big and will dominate the terms in (3.22). Moreover, there are different delays in the acquisition instruments as well as the delay in the transducers itself that will contribute to the error in $\sigma_{n_i}^2$. However, this is a systematic error that disappears when τ_0 is measured and not computed from (3.21).

3.7.2 Error in the transversal interaction

The variance of the error in the transversal component is going to be computed assuming that the approximation in (3.6) is valid. The variance then reduces to

$$\begin{aligned} \sigma_t^2 &= (\cos\theta(y_R - y_T) - \sin\theta(x_R - x_T))^2 \sigma_{c_0}^2 + E[c_0^2 (\cos\theta(y_R - y_T) - \sin\theta(x_R - x_T))^2] \\ &= (\cos\theta(y_R - y_T) - \sin\theta(x_R - x_T))^2 \sigma_{c_0}^2 \\ &\quad + c_0^2 E[\cos^2\theta(y_R - y_T)^2 - 2\cos\theta\sin\theta(y_R - y_T)(x_R - x_T) + \sin^2\theta(x_R - x_T)^2] \\ &= c_0^2 (2\sigma_p^2 E[\cos^2\theta] + 2\sigma_p^2 E[\sin^2\theta]) \\ &= (\cos\theta(y_R - y_T) - \sin\theta(x_R - x_T))^2 \sigma_{c_0}^2 + 2c_0^2 \sigma_p^2. \end{aligned}$$

Surprisingly, σ_t does not depend on the error in the angle-of-arrival measurements, but on the other hand, σ_p is always present.

3.8 Conclusions

In this chapter, we have defined the inverse problem concerning the reconstruction of the sound speed c and the moving component \mathbf{v} of an inhomogeneous moving medium. Two types of measurements have been proposed to compute the solution of the inverse problem, namely, the longitudinal and the transversal interaction. An important result of our study is that for the complete reconstruction of c and \mathbf{v} , the longitudinal and the transversal interactions are both needed. However, the knowledge of the longitudinal interaction (respectively, transversal interaction) allows the reconstruction of only pure solenoidal (respectively, pure conservative) fields. As opposed to previously suggested solutions, we showed that the longitudinal interaction is indeed sufficient for the

reconstruction of the solenoidal vector fields on bounded domains. As a practical example of such a solenoidal field, we referred to the case of estimating a horizontal slice of the wind field in the stratified atmosphere. We also showed that the angle-of-departures/arrivals are sufficient to reconstruct a temperature and an irrotational 2D vector fields on bounded domains.

The longitudinal interaction can be obtained from the time-of-flight measurements. We showed that the transversal interaction can be obtained from the angle-of-departure and the angle-of-arrival measurements of the sound waves, and suggested two techniques to measure these angles.

We presented the non-linear inversion algorithm that alternates between estimating the trajectories of the sound wave and the unknown fields. The error analysis presented at the end of the chapter helps in better understanding different technical and practical aspects that influence the reconstruction accuracy.

Chapter 4

Inversion Methods

In the previous chapter, we outlined the general inverse tomography algorithm. We pointed out that the step in which the system of equations in (3.16) is inverted is the crucial step responsible for the overall success of the algorithm. In this chapter, three inversion methods for the previous system are proposed and tested numerically. All three methods are conceptually different. The difference consists in the use or not of any *a priori* information (or regularization), and whether or not the inversion method is linear. Also, in all three methods, different models are chosen to describe the unknown fields.

In this chapter, Section 4.1 gives a brief classification of the inversion methods. In Section 4.2, the method based on squared error minimization is presented. It does not use any *a priori* information, and, therefore, it refers to a general practical situation of estimating the sound speed and the moving component of an inhomogeneous medium. This method is used to test the convergency of the non-linear tomography algorithm and the effect of using an approximation to compute the transversal component. The two other methods, presented in Sections 4.3 and 4.4, make use of some additional assumptions on the underlying field. In Section 4.3, the field is assumed to be sparse in some transform domain, and, in Section 4.4, the field is assumed to be characterized by a finite number of parameters.

All the inversion methods are tested with numerical simulations. Practical experiments will be described in Part II. A simulation gives complete control over the setup and gives exact knowledge of the unknown parameters. It enables to test the effectiveness of the inversion method both in the context of the global iterative inversion algorithm, and as the inversion step in the non-iterative case.

4.1 Overview

A common idea behind most of the inversion methods is to minimize the error $e = d - Gm$ in some sense.

Group 1 The error l_2 -norm minimization is achieved in methods like the Moore-Penrose pseudoinverse, gradient methods, etc. When the matrix G is of large size, the direct inversion is practically limited by computational complexity and memory constraints and the methods referred to as row action

or Algebraic Reconstruction Technique (ART) are more attractive. The main idea is that the solution is updated by successively processing each equation separately. Improvements that lead to better convergence are suggested in Simultaneous Iterative Reconstruction Technique (SIRT).

Group 2 Another group of methods also try to minimize the squared error but in the statistical sense (on average) which results in the stochastic methods based on Wiener filtering or Kalman filtering. In these methods *a priori* knowledge about the correlation structure of the solution and the noise is needed. The methods can be extended to include correlation over space and time [73] as well.

Group 3 Depending on the specific example, the notion of the *a priori* knowledge can be extended to any other useful information that is available about the field, e.g. the temperature is localized, the wind is a “smooth” function, etc. In many cases the information can not be incorporated into the covariance matrix and other deterministic methods like parametric estimation needs to be applied. For example, it may be known that in a certain transform domain the model parameters \mathbf{m} have a sparse representation, i.e. $\mathbf{T}\mathbf{m} = \mathbf{m}_s$ where \mathbf{m}_s is sparse. In that case, the new solution \mathbf{m}_s to the system

$$\mathbf{GT}^\dagger \mathbf{T}\mathbf{m} = \mathbf{GT}^\dagger \mathbf{m}_s = \mathbf{d}$$

is searched as a minimum l_0 -norm solution and it can be achieved by different algorithms as linear programming or convex optimization, which under certain circumstances converge to the solution with minimum l_0 -norm. The concept is known as Compressed Sensing [22] and it is shown to be very useful for tomographic sampling in general [37].

4.2 Temperature and wind estimation using the inversion based on l_2 -norm minimization

In this section, we consider a practical problem of estimating temperature and wind field in the atmosphere. We implement Algorithm 3.1 with the inversion step based on minimizing the l_2 -norm of an error between the data and the model output. Since the inversion methods from the first group impose no constraints on the reconstructed fields, no regularization is applied. It is, hence, useful as means to examine the “pure” resolving power of the algorithm. This allows to test the approximation steps applied in deriving the longitudinal and the transversal components.

Sound propagation in the atmosphere In dry air, we can assume the ideal gas law approximation for sound velocity, which is accurate for standard Earth sea-level conditions. Using the ideal gas law, the sound speed is:

$$c = \sqrt{R\gamma T}, \quad (4.1)$$

where R is the molar gas constant (approximately 8.3145 J/K/mol expressed in units of energy per kelvin per mole), γ is the adiabatic index (assumed to

be 1.400), and $T[K]$ is the absolute temperature in kelvins. Based on (4.1) the meteorologists use even the simpler relationship

$$c = 20.05\sqrt{T(1 + 0.511q)}, \quad (4.2)$$

where the value 20.05 stands for the product of specific gas constant for dry air and the ratio of specific heat at constant volume, and q is the mixing ratio of water vapor (usually between 0 and 0.03). Knowing the sound speed we can directly compute the temperature in the atmosphere. As there is a one-to-one mapping between T and c in the atmosphere, we are sometimes going only to concentrate on estimating c . The wind speed acts as the moving component of the medium, and it is linearly added to the sound speed to form the total speed of sound propagation, known as group velocity,

$$\mathbf{u} = c\mathbf{n} + \mathbf{v},$$

where \mathbf{v} is the wind speed. Our goal is to estimate c and \mathbf{v} from the time-of-flight and the angle-of-departure/arrival measurements.

4.2.1 Reconstruction of temperature and wind field

The first step in estimating the unknown fields in the region of interest is to choose a discrete model that represents the fields. We define a grid covering the region of interest, and assume that the fields can be represented by: 1) the node values assigned at the nodes, and 2) some interpolation scheme to attribute the values between the nodes. The node values are the elements of the model parameters \mathbf{m} . The limiting case of having infinitely many grid points is equivalent to the continuous case (assuming that the underlying field is smooth). We choose that the values of the points between the nodes are approximated by a linear combination of the nodal values

$$m(\mathbf{r}) = \sum_{k=1}^N m_k \alpha_k(\mathbf{r}), \quad (4.3)$$

where m_k is the corresponding value at the node k , and $\alpha_k(\mathbf{r})$ is an interpolating function. In general, the points between the nodes are interpolated using polynomials of a certain degree.

For example, one can cover the domain with a tiling of triangles, triangular cells, and assume a linear interpolation in which case $N = 3$. Function $\alpha_k(\mathbf{r})$ is then a two-dimensional polynomial of order 1, i.e. the components are approximated by a plane for every triangle. This is a standard interpolation in finite element methods [11] called *linear Lagrange triangle* interpolation. The space generated by the nodal variables is the space of two-dimensional continuous piecewise linear functions. Choosing v_x and v_y components of the wind field \mathbf{v} as the nodal values, and Δc_k elements of the sound speed field as the nodal values as well, the continuity of the fields is going to be ensured. If the trajectories are known, (4.3) allows to write the set of interactions in (3.10) as a linear combination of the unknown components $v_{x,k}$, $v_{y,k}$ and Δc_k . For the

longitudinal component we have:

$$\begin{aligned}
l_\Gamma &= \int_\Gamma (\Delta c \mathbf{n} + \mathbf{v}) \cdot d\mathbf{s} = \sum_{j=1}^J \int_{\Gamma_j} (\Delta c \mathbf{n} + \mathbf{v}) \cdot d\mathbf{s} \\
&= \sum_{j=1}^J \int_{\Gamma_j} \sum_{k=1}^3 \alpha_{jk}(s) (\Delta c_{jk} \mathbf{n} + \mathbf{v}_{jk}) \cdot d\mathbf{s} \\
&= \sum_{j=1}^J \sum_{k=1}^3 \left(\underbrace{\int_{\Gamma_j} \alpha_{jk}(s) \mathbf{n} \cdot d\mathbf{s}}_{a_{jk}} \right) \Delta c_{jk} + \sum_{j=1}^J \sum_{k=1}^3 \left(\underbrace{\int_{\Gamma_j} \alpha_{jk}(s) s_x ds}_{b_{jk}} \right) v_{x,jk} \\
&\quad + \sum_{j=1}^J \sum_{k=1}^3 \left(\underbrace{\int_{\Gamma_j} \alpha_{jk}(s) s_y ds}_{c_{jk}} \right) v_{y,jk}, \tag{4.4}
\end{aligned}$$

where the index j corresponds to the current cell, and $\Gamma_j = \Gamma \cap \text{cell}_j$. The index k denotes the vertex index within the current cell. A similar set of equations can be developed for the transversal components, by exchanging the vector $\mathbf{s} = [s_x, s_y]$ with the vector $\mathbf{s}_\perp = [-s_y, s_x]$,

$$\begin{aligned}
t_\Gamma &= \int_\Gamma (\Delta c \mathbf{n} + \mathbf{v}) \cdot d\mathbf{s}_\perp = \sum_{j=1}^J \int_{\Gamma_j} (\Delta c \mathbf{n} + \mathbf{v}) \cdot d\mathbf{s}_\perp \\
&= \sum_{j=1}^J \int_{\Gamma_j} \sum_{k=1}^3 \alpha_{jk}(s) (\Delta c_{jk} \mathbf{n} + \mathbf{v}_{jk}) \cdot d\mathbf{s}_\perp \\
&= \sum_{j=1}^J \sum_{k=1}^3 \left(\underbrace{\int_{\Gamma_j} \alpha_{jk}(s) \mathbf{n} \cdot d\mathbf{s}_\perp}_{a_{jk}} \right) \Delta c_{jk} - \sum_{j=1}^J \sum_{k=1}^3 \left(\underbrace{\int_{\Gamma_j} \alpha_{jk}(s) s_y ds}_{b_{jk}} \right) v_{x,jk} \\
&\quad + \sum_{j=1}^J \sum_{k=1}^3 \left(\underbrace{\int_{\Gamma_j} \alpha_{jk}(s) s_x ds}_{c_{jk}} \right) v_{y,jk}. \tag{4.5}
\end{aligned}$$

In matrix notation, we can write:

$$\begin{pmatrix} \mathbf{G}_l \\ \mathbf{G}_t \end{pmatrix} \cdot \begin{bmatrix} v_x \\ v_y \\ \Delta c \end{bmatrix} = \begin{bmatrix} \mathbf{l} \\ \mathbf{t} \end{bmatrix}, \tag{4.6}$$

where the matrices \mathbf{G}_l and \mathbf{G}_t describe the linear relationship between the measurements and the unknowns, as given in (4.4) and (4.5). The system in (4.6) is to be solved using Algorithm 3.1.

4.2.2 Reconstruction of temperature and solenoidal wind field

In Section 3.5.3, it was shown that the longitudinal interaction allows to recover the sound speed and the medium speed when the medium speed is a 2D solenoidal vector field. Therefore, the longitudinal interaction is sufficient for the reconstruction of temperature and a solenoidal wind field, and the system in (4.6) can be reduced to:

$$\mathbf{G}_l \cdot \mathbf{m} = l. \quad (4.7)$$

In the previous case, we chose to represent the wind field as $\mathbf{v} = [v_x, v_y]$. However, this representation does not reflect the fact that \mathbf{v} has only a solenoidal component. To incorporate this constrain in the solution of the wind field, one of the possibilities is to choose a different wind field representation. For example, the condition of zero divergency is satisfied if a vector field has only a vector potential component, namely

$$\mathbf{v} = \nabla \times \psi \mathbf{e}_z = \left[\frac{\partial \psi}{\partial y}, -\frac{\partial \psi}{\partial x} \right],$$

where $\psi = \psi \mathbf{e}_z$ is a vector potential. This representation automatically discards all irrotational (“invisible”) winds because no irrotational field can be represented using vector potentials. If we want to ensure the continuity of the field then ψ , but also its derivatives $[\frac{\partial \psi}{\partial x}, \frac{\partial \psi}{\partial y}]$ should be continuous. In this case, the linear Lagrange triangles are not anymore appropriate, and we choose another finite element, namely the reduced *Hsieh-Clogh-Tocher triangles* (HCT) [9]. The HCT interpolates the third order polynomial function that is continuous together with its first order derivatives. In the HCT representation, the region of interest is covered with the triangular cells and the points inside the cells, are parameterized using the value of the 3 vertex nodes m_k , and 6 directional first order derivatives $\frac{\partial m}{\partial x}, \frac{\partial m}{\partial y}$ (2 per node),

$$m(\mathbf{r}) = \sum_{k=1}^9 m_k \alpha_k(\mathbf{r}).$$

This more complex tessellation adds complexity to the algorithm, since now every cell is determined by 9 parameters. However, the reconstructed wind field is a second order polynomial function, while the reconstructed sound speed is a third order polynomial. The coefficients in \mathbf{G}_l has to be computed accordingly to the new representation, but similarly as before:

$$\begin{aligned} l_\Gamma &= \int_{\Gamma} (\Delta c \mathbf{n} + \nabla \times \psi \mathbf{e}_z) \cdot d\mathbf{s} \\ &= \sum_{j=1}^J \int_{\Gamma_j} (\Delta c \mathbf{n} + \nabla \times \psi \mathbf{e}_z) \cdot d\mathbf{s} \\ &= \sum_{j=1}^J \int_{\Gamma_j} \left(\sum_{k=1}^9 \alpha_k(s) \Delta c_k \right) \mathbf{n} \cdot \mathbf{s} + \nabla \times \left(\sum_{k=1}^9 \beta_k(s) \psi_k \right) \mathbf{e}_z \cdot \mathbf{s} ds, \end{aligned}$$

where ψ_k and Δc_k are now the unknowns in the HCT model. The previous equation then needs to be incorporated in the global non-linear algorithm Algorithm 3.1.

4.2.3 Inversion: conjugate-gradient method

We simulate both the forward and the inverse problem. First, the forward model is simulated. Our code implements the equations (2.5) and (2.6) for ray tracing in an inhomogeneous moving medium. A fifth-order Runge-Kutta algorithm is applied to integrate the ray equations forward in time. The shooting method [56] is used to search for the correct ray. The algorithm has an adjustable integration step size and error tolerance at the receiver side. The resulting time-of-flights, the angle-of-arrivals and angles-of-departures are then taken as the measurement set.

Having the measurements, the solution of equations (4.6) and (4.7) is computed using Algorithm 3.1. We choose to use the conjugate gradient method as the inversion step in Algorithm 3.1. This method is itself an iterative method, and it achieves the solution which minimizes the l_2 -norm of the error e , in maximum M iterations, where M is the number of unknown parameters. However, we perform only few iterations (internal iteration of the conjugate-gradient method). The choice of doing only few iterations is motivated by the fact that our goal is not really to solve (3.17) but to converge to the solution of the non-linear problem $\mathbf{G}(\mathbf{m})\mathbf{m} = \mathbf{d}$. While the convergence is never insured, it is always “safer” to make smaller updates $\Delta\mathbf{m}$ assuming that the direction of the global minimum ($\min[\mathbf{d} - \mathbf{G}(\mathbf{m})\mathbf{m}]$) is close to the direction of the minimum in (3.17).

4.2.4 Simulation results

The simulation setup consists of a circular array that is 10 m in diameter, and it is equipped with 20 transmitters and 20 receivers. Every transmitter sends a signal to every receiver, which results in 380 transmission paths. The region of interest is covered with triangular cells of the equal size. Ideally, to resolve the sound speed and the wind field at one nodal point the number of transmissions affected by that node needs to be equal or greater than the number of unknowns that characterize the node. Also, the total number of transmission paths needs to be equal or greater than the total number of unknowns. However, if no a priori knowledge is considered the system of equations to be solved is usually poorly conditioned. It can be stabilized by having more measurements than the number of unknowns.

Example 4.2.1 (Perfect model match). In the first example, the perfect model match between the forward and the inverse problem is assumed. The only noise comes from the error in computing the forward model (corresponding to the tolerance error in the shooting method and the error in Runge-Kutta method). In every iteration, we need to solve the linearized system in (4.6).

Figure 4.1 shows the original wind field and the reconstructions for the straight ray and the bent ray model respectively. The arrows represent the amplitudes and the directions of the wind. The maximal wind speed is 5 m/s. The bent ray model achieves better result and always outperforms the straight

ray model. Numerically, the root mean squared error (RMSE) of the wind reconstruction is used to measure the average error. In this example, we computed $\text{RMSE}_v = 1.63$ m/s for the straight ray, and $\text{RMSE}_v = 1.35$ m/s for the bent ray model. The local error is usually smaller, since the RMSE is computed including points at the border, which are reconstructed with less accuracy due to the fact that less information about these points is available.

The original sound speed is shown in Figure 4.2(a), and the reconstruction errors for the straight and bent ray model are represented in Figure 4.2(b) ($\text{RMSE}_c = 2.69$ m/s), and Figure 4.2(c) ($\text{RMSE}_c = 0.81$ m/s), respectively. Thus, like for the wind field, the reconstruction with the bent ray model outperforms the straight ray model reconstruction. □

Example 4.2.2 (Imperfect model match plus noise). In the second example, it is assumed that the 2D slice of a wind field is solenoidal. The measurement setup is identical to the previous one, except that in this case the region of interest is covered by the HCT triangles.

Figure 4.3(a) represents the original and the reconstructed wind speed. The maximal wind speed is 6.2 m/s. No difference between the true wind and the reconstructed wind can be noticed. Figure 4.3(b) shows the reconstruction for the noisy received signal with $\text{SNR} = 10$ dB. The model mismatch is created by adding 30 dB distortion to the coefficients in \mathbf{G}_l (with respect to the energy of the coefficients in \mathbf{G}_l). The result shows that the reconstruction is robust to the noise, and the model mismatch.

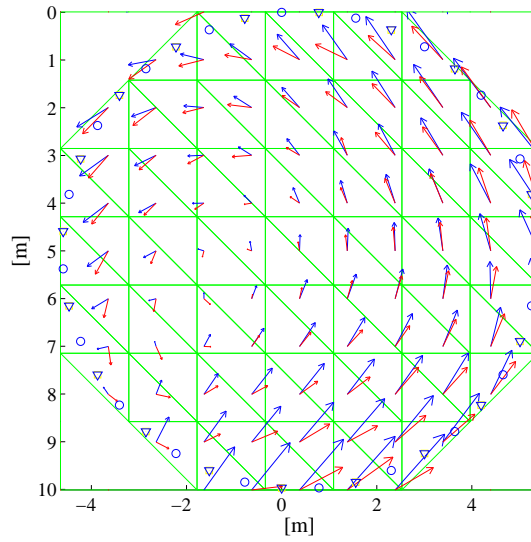
The original sound speed and the corresponding reconstructions are shown in Figure 4.4. The sound speed reconstruction is robust to the noise and the model mismatch as well. □

4.2.5 Discussion

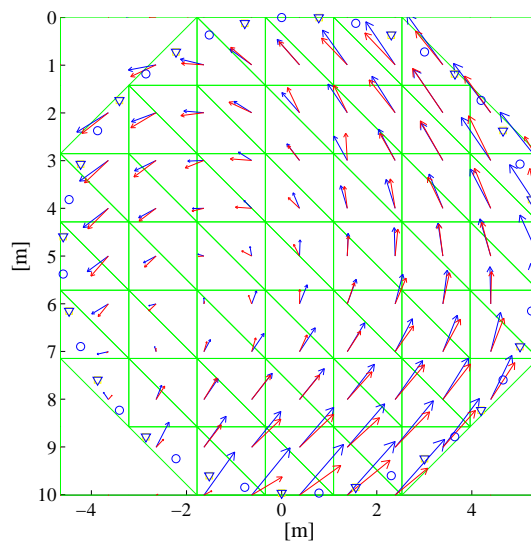
The idea of performing only a few (one or two) iterations in the conjugate gradient method showed to be successful. Numerical simulations confirmed that the iterative algorithm achieves better reconstruction than the one step inversion. Also, the approximations introduced in the computations of the longitudinal and the transversal interactions still lead to a good reconstruction. For both examples, the iterative method converges after 5 iterations. However, when the initial solution is far from the correct one, the algorithm usually shows some improvement in the first two-three iterations, and then starts diverging. This is a well known problem for tomographic algorithms that are not well conditioned (and no regularization is applied). Like in other non-linear algorithms, we define the stopping criterium based on: 1) error between the measurements and the forward prediction of the current system; 2) number of iterations; 3) variation of the solution.

From a practical point of view, numerical results confirm as well that acoustic tomography offers a powerful method for studying small scale temperature and wind distributions in the atmosphere with a high spatial resolution. Both numerical examples show that the wind eddies and temperature variations have been resolved. The number of measurements taken over time is potentially high as well, since the information is obtained without interaction with the

atmosphere and without inertia of the system. Nevertheless, as the angle-of-arrival/departure can be estimated with the time-of-flights (in case of an acoustic dipole), the full reconstruction is now physically realizable using only the time-of-flight measurements.



(a)



(b)

Figure 4.1: Wind field. (a) Original (blue) and the reconstructed (red) wind field using the straight ray model, $RMSE_v = 1.63$ m/s. (b) Original (blue) and the reconstructed (red) wind field using the bent ray model and the iterative algorithm, $RMSE_v = 1.35$ m/s.

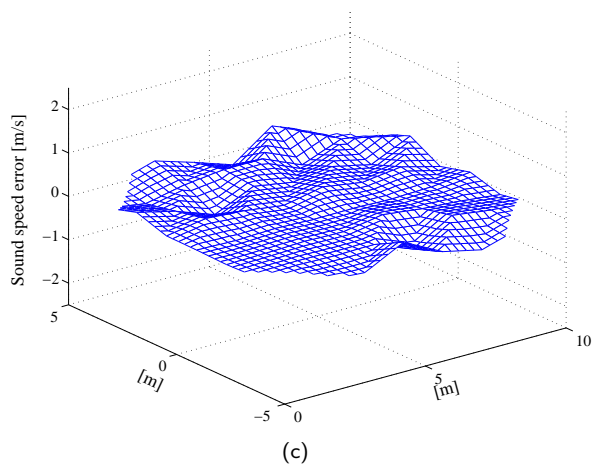
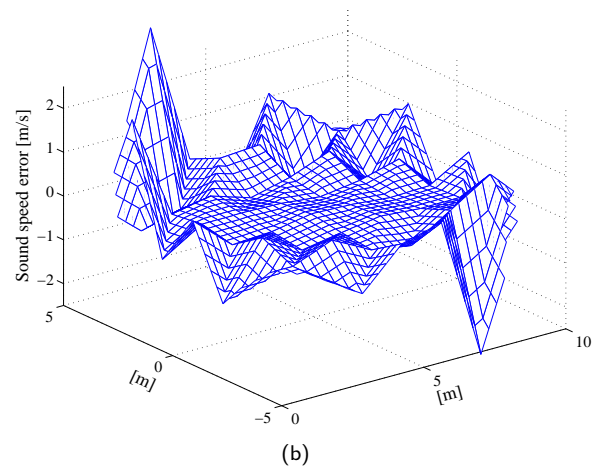
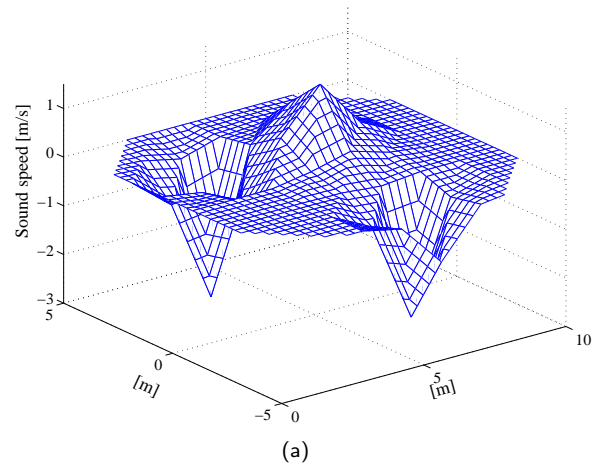
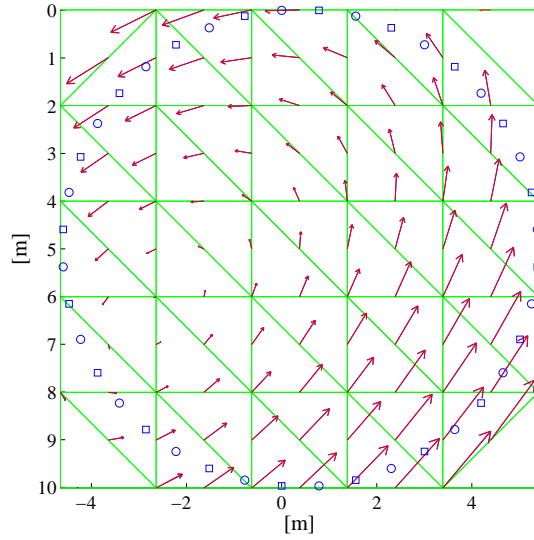
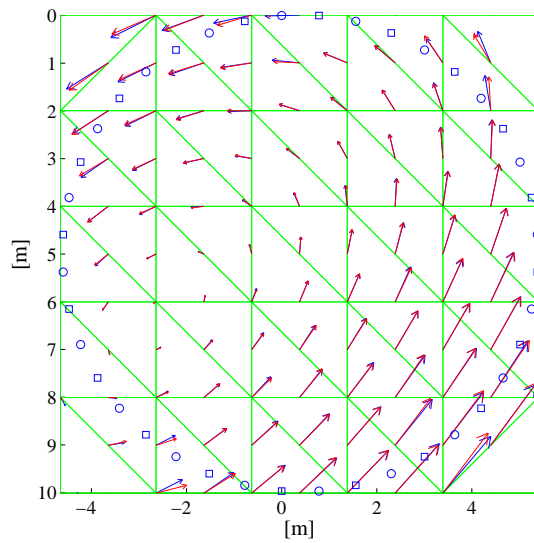


Figure 4.2: Sound speed. (a) Original sound speed. (b) Reconstruction error using the straight ray model, $RMSE_c = 2.69$ m/s. (c) Reconstruction error using the bent ray model and the iterative algorithm, $RMSE_c = 0.81$ m/s.



(a)



(b)

Figure 4.3: Wind field. (a) Original (blue) and the reconstructed (red) wind field overlap. (b) Original (blue) wind and the wind reconstructed (red) from the noisy received signal $\text{SNR} = 10$ dB, and for the model mismatch created by adding 30 dB of distortion to the coefficients in \mathbf{G}_l .

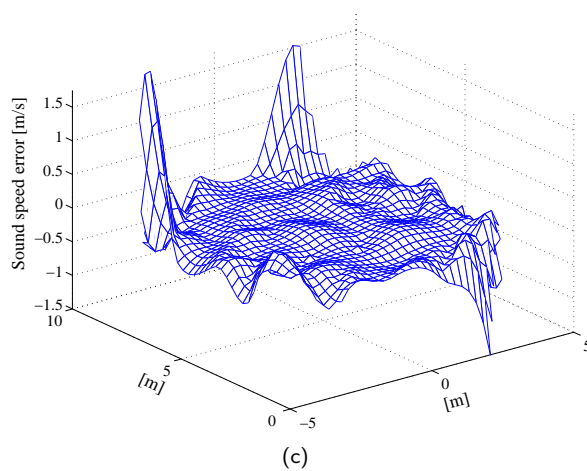
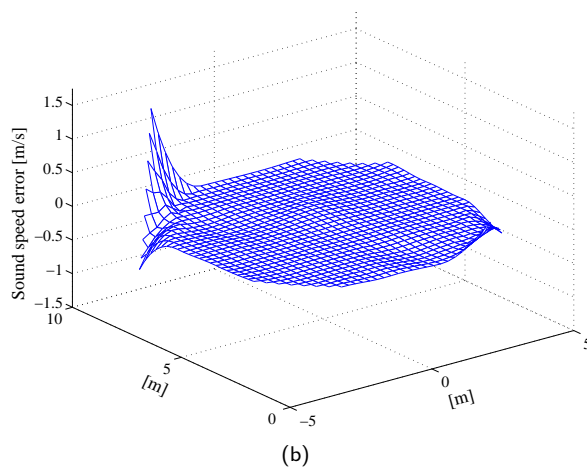
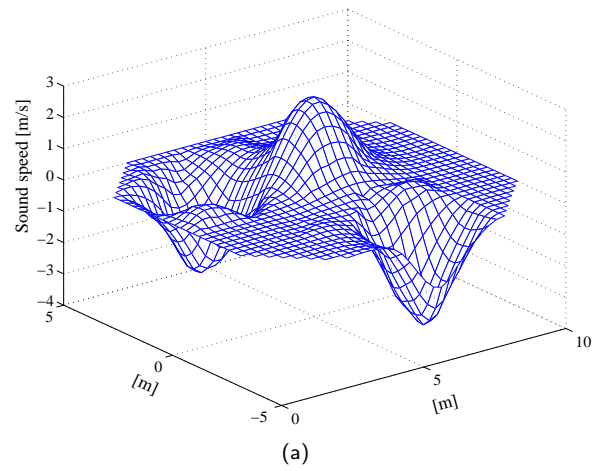


Figure 4.4: Sound speed. (a) Original sound speed. (b) Reconstruction error for the perfect model match. (c) Reconstruction error from the noisy received signal $\text{SNR} = 10$ dB, and for the model mismatch created by adding 30 dB of distortion to the coefficients in \mathbf{G}_l .

4.3 Temperature estimation in diffusive environment using the inversion based on sparsity

In this section, we propose a new inversion method for tomographic reconstruction. The method is based on the two fundamental principles: 1) the unknown fields have a sparse representation (or, equivalently, are sparse); and 2) the measurements are chosen such that they allow to find the solution even when having fewer measurements than the number of unknowns. This method, known as compressed sensing (CS), was first proposed in the literature of information theory and approximation theory in an abstract general setting. Our goal is to show that compressed sensing can be successfully applied in acoustic tomography problems, because: 1) the unknown fields we want to reconstruct are usually sparse; and 2) the tomographic measurements indeed allow to find the solution with fewer measurements than the total number of unknowns¹. Therefore, this method can potentially increase the resolution of tomographic images, as the total number of reconstructed points can be larger than the number of measurements. Some drawbacks of the method will be pointed out later.

In Section 4.3.1 we present the basic ideas behind CS. The application of this method will be presented in Section 4.3.2, on the example of temperature estimation in a diffusive environment. The concept can be easily applied to other appropriate acoustic tomography problems. For simplicity, we only go through the first iteration in Algorithm 3.1, i.e. we perform the straight ray acoustic tomography. Simulation results are shown in Section 4.3.3, and the conclusions are given in Section 4.3.4.

4.3.1 Compressed Sensing

The central theorem of signal processing is the Nyquist/Shannon sampling theorem that says that the number of samples needed to reconstruct a signal without error is determined by the signal bandwidth. Recently, an alternative theory of CS has emerged which shows that super-resolved signals and images can be reconstructed from far fewer measurements than what is usually considered necessary. In fact, CS suggests ways to economically translate analog data into already compressed digital form [22, 12]. Because typical signals have some structure, they can be compressed efficiently without much perceptual loss. For instance, modern transform coders such as JPEG2000 exploit the fact that many signals have a sparse representation in a fixed basis, meaning that one can store or transmit only a small number of adaptively chosen transform coefficients rather than all the signal samples. The way this traditionally works is that one acquires the full signal, computes all transform coefficients, encodes that largest coefficients and discards all the others. This raises a fundamental question: because most signals are compressible, why spend so much effort acquiring all the data when we know that most of it will be discarded? Compressed sensing suggests an efficient way of acquiring sparse signals.

To have an idea of CS, consider a continuous 2D signal $m(\mathbf{r})$, and suppose that the basis $\mathbf{\Lambda}(\mathbf{r}) = [\lambda_1(\mathbf{r}), \lambda_2(\mathbf{r}), \dots, \lambda_M(\mathbf{r})]$ provides a K -sparse represen-

¹We remark here the the total number of unknowns refers to the size of the unknown sparse vector and not to the number of non-zero coefficients in that sparse vector.

tation of the signal, that is, $m(\mathbf{r})$ can be written as a linear combination of K elements of $\mathbf{\Lambda}$:

$$m = \sum_{j=1}^M m_j^s \lambda_j = \sum_{k=1}^K m_{j_k}^s \lambda_{j_k}, \quad (4.8)$$

where j_k denotes the position of K nonzero entries of the sparse vector \mathbf{m}^s (the superscript s denotes the sparsity), and we omit the dependence on \mathbf{r} for simplicity of notation. For example, we know that there are M heat sources in the region of interest but only K are active (see Figure 4.5). The equation (4.8) can be written in matrix form as

$$m = \mathbf{\Lambda} \mathbf{m}^s,$$

where \mathbf{m}^s is an $M \times 1$ column vector that has K nonzero elements, and the goal is to reconstruct the coefficients of the sparse vector \mathbf{m}^s . Unlike in the traditional approach where we need M measurements, the compressed sensing approach suggests $N < M$ measurements. The measurements are acquired as projections of the signal $m(\mathbf{r})$ onto a second set of basis $\mathbf{\Omega}(\mathbf{r}) = [\omega_1(\mathbf{r}), \omega_2(\mathbf{r}), \dots, \omega_N(\mathbf{r})]$, that is

$$d_i = \langle \omega_i, m \rangle = \sum_{j=1}^M \langle \omega_i, \lambda_j \rangle m_j^s \quad (4.9)$$

where $\langle \cdot, \cdot \rangle$ denotes the inner product. To simplify the notation, we can write in matrix form

$$\mathbf{d} = \mathbf{G}(\mathbf{\Lambda}) \mathbf{m}^s,$$

where $G(\mathbf{\Lambda})_{ij} = \langle \omega_i, \lambda_j \rangle$, and \mathbf{d} is of size N .

Since $N < M$, the inversion from the measurement vector \mathbf{d} back to \mathbf{m}^s is ill-posed, as the system of equation is underdetermined. However, the premise that \mathbf{m}^s is sparse radically changes the problem, making the search for solutions feasible even when $N < M$. It has been shown that for the perfect reconstruction of K -sparse vectors of dimension M , we need only

$$N = O(K \log M) \ll M \quad (4.10)$$

measurements [12, 22]. In this case, the signal can be recovered by solving an l_1 -norm minimization problem

$$\hat{\mathbf{m}}^s = \arg \min \|\mathbf{m}^s\|_1 \quad \text{s.t.} \quad \mathbf{d} = \mathbf{G} \mathbf{m}^s. \quad (4.11)$$

This optimization problem, also known as basis pursuit [14], can be solved using standard linear programming. The solution exists when the bases $\mathbf{\Omega}$ and $\mathbf{\Lambda}$ are incoherent [22], or equivalently, when the basis set $\{\omega_i\}$ does not provide a sparse representation of the elements $\{\lambda_j\}$. There is a lot of freedom in choosing the appropriate basis elements to approximate the field of interest in a sparse manner. For example, wavelet expansion can be used whenever there are sharp transitions in the field since wavelets can represent sharp transitions in a very efficient manner. As one can see, there is a strong connection between image compression techniques and this inversion method.

In the case of noisy measurements, it is possible to adapt the optimization

4.3. Temperature estimation in diffusive environment using the inversion based on sparsity 51

algorithm to incorporate the noise [14]. The new optimization procedure can be stated as:

$$\hat{\mathbf{m}}^s = \arg \min(\|\mathbf{d} - \mathbf{G}\mathbf{m}^s\|_2^2 + \alpha\|\mathbf{m}^s\|_1), \quad (4.12)$$

where α controls the trade off between the sparsity of the solution and the residual in the reconstruction.

In the following, we will show that tomographic measurements provide data of the form (4.9).

4.3.2 Temperature estimation in a diffusive environment

We have already seen in (4.1) and (4.2) that in dry air the temperature can be inferred from the sound speed. If there is no wind, i.e. $\mathbf{v} = 0$, the time-of-flights are

$$\tau = \int_{\Gamma} \frac{1}{c} ds \simeq \int_{\Gamma} \frac{1}{c_0} ds - \frac{R\gamma}{2c_0^3} \int_{\Gamma} \Delta T ds,$$

where $T = T_0 + \Delta T$, T_0 is the spatial average temperature, ΔT is the temperature fluctuation, $c_0 = \sqrt{R\gamma T_0}$ is the spatial average of the sound speed, and $T_0 \ll \Delta T$. The longitudinal interaction is then

$$l_{\Gamma} = \frac{2c_0^3}{R\gamma} (\tau_0 - \tau) = \int_{\Gamma} \Delta T ds.$$

In the following, we assume that the temperature variation ΔT has a K -sparse representation in a basis set $\mathbf{\Lambda}$, that is

$$\Delta T = \sum_{j=1}^M m_j^s \lambda_j = \sum_{k=1}^K m_{j_k}^s \lambda_{j_k},$$

with the same notation as in (4.8). The time-of-flight measurements represent the available data from which we can compute the longitudinal interaction. Writing l_{Γ} as

$$l_{\Gamma} = \int_{\Gamma} \Delta T ds = \sum_{j=1}^M m_j^s \int_{\Gamma} \lambda_j ds = \sum_{j=1}^M \langle \omega_i, \lambda_j \rangle m_j^s.$$

we can see that the tomographic measurements inherently provide the data of the form in (4.9). The basis elements ω_i are the 2D indicator functions $\mathbf{1}_{\Gamma}$ with the support Γ , and the index i represents different trajectories along which the measurements are taken.

Diffusion Assume that at a certain time instant t_0 we have a temperature field $T_{t_0}(x, y)$. In a diffusive environment the change of temperature over time is governed by the heat equation, that is, a concentrated deposit of heat diffuses away in a Gaussian manner, as described by the 2-D heat kernel:

$$h(x, y, t) = \frac{1}{4\pi Dt} e^{-\frac{x^2+y^2}{4Dt}} \quad (4.13)$$

where D is a diffusion constant. If there are no active heat sources, the temperature at time t can be computed as a convolution of the initial heat at time t_0 with the heat kernel:

$$T_t(x, y) = T_{t_0} * h(x, y),$$

and, as well,

$$\Delta T_t(x, y) = \Delta T_{t_0} * h(x, y). \quad (4.14)$$

Keeping the same setup (number of emitters and receivers) we can take the time-of-flight measurements over a series of time instants. One can predict the change of the kernels in the diffusion process by knowing the physical parameters of the medium, that is the diffusion constant. By taking measurements over time instants t_1, t_2, \dots, t_k , one can write

$$\begin{bmatrix} \mathbf{l}(t_1) \\ \mathbf{l}(t_2) \\ \vdots \\ \mathbf{l}(t_k) \end{bmatrix} = \begin{bmatrix} \mathbf{G}(\Lambda_{t_1}) \\ \mathbf{G}(\Lambda_{t_2}) \\ \vdots \\ \mathbf{G}(\Lambda_{t_k}) \end{bmatrix} \mathbf{m}^s, \quad (4.15)$$

where $\mathbf{G}(\Lambda_{t_i})$ is found by first computing the new diffused kernel Λ_{t_i} at time t_i . This will result in a larger number of measurements than in the case of one-shot measurements, and therefore in a more accurate estimation of ΔT_t .

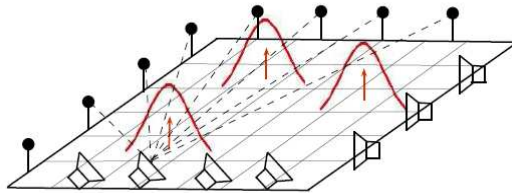


Figure 4.5: Acoustic tomography setup with transmitters and receivers placed around the region of interest. The temperature distribution is sparse in B-spline domain, as it originates from 3 local sources with the B-spline kernel.

4.3.3 Simulation results

In the following, we are going to show the simulation results for two different temperature models, one that reflects sparsity in B-spline domain, and the other that reflects sparsity in cosine basis domain. In the simulations, we first compute the travel times for a given temperature distribution, and then use them as the input data in our reconstruction algorithm.

Example 4.3.1 (Sparsity in B-spline domain). In the first scenario, we consider the tomographic problem in which the goal is to reconstruct the temperature field produced by K localized sources. We define an M -node grid covering the tomographic region, and assume that the sources can appear only at the nodal positions. The induced field can be modeled as a set of 2D weighted

4.3. Temperature estimation in diffusive environment using the inversion based on sparsity53

Diracs convolved with a normalized kernel $\varphi(x, y)$ that describes the sources, as shown in Figure 4.5. The basis functions λ_j are then

$$\lambda_j = \delta(x_j, y_j) * \varphi(x, y) \quad \text{for } j = 1, \dots, M,$$

where $\delta(x, y)$ is the Dirac delta function, and (x_j, y_j) is the j -th nodal point. In this example, the sources are described with 2D cubic B-splines:

$$\varphi\left(\frac{\mathbf{r}}{a}\right) = \begin{cases} \frac{2}{3} - \frac{\|\mathbf{r}\|^2}{a^2} + \frac{\|\mathbf{r}\|^3}{2a^3} & 0 \leq \frac{\|\mathbf{r}\|}{a} < 1, \\ \frac{(2 - \frac{\|\mathbf{r}\|}{a})^3}{6} & 1 \leq \frac{\|\mathbf{r}\|}{a} < 2, \\ 0 & 2 \leq \frac{\|\mathbf{r}\|}{a}, \end{cases}$$

where we use $\|\mathbf{r}\| = \sqrt{x^2 + y^2}$ as the radial coordinate. The parameter $a > 0$ is the scale of the B-spline that regulates the spline width. We also assume that the sources can be different, that is, there are p possible widths of the kernels. Since for each of M nodes on the grid we can choose any set of the p possible kernels, there are pM unknowns in total. Then, the temperature can be represented as

$$\Delta T = \sum_{i=1}^p \sum_{j=1}^M \varphi_i(x - x_j, y - y_j) m_{M(i-1)+j}^s = \sum_{i=1}^p \sum_{j=1}^M \lambda_{M(i-1)+j} m_{M(i-1)+j}^s$$

where $m_{M(i-1)+j}^s$ is the weight of the kernel φ_i on the node j with the position (x_j, y_j) . As long as there are K active sources, only K of the coefficients in \mathbf{m}^s are non-zero.

In Figure 4.6(a) we show the original temperature that is composed of $K = 5$ cubic splines, arbitrarily placed on the grid of $M = 12 \times 12 = 144$ nodes. Their positions and the weights are randomly chosen. We also assume that the possible spline scales belong to the set of $p = 4$ elements. In total, we have $pM = 576$ unknowns. There are 8 transmitters and 8 receivers placed on the border of the region of interest. We consider a diffusive environment and take the measurements in 2 time slots, what results in $N = 128$ measurements. In the diffusion process, the shapes of the kernels change according to (4.14); however, the positions of the Diracs remain the same. To account for the effect of noise and the model mismatch, we add 40 dB distortion to \mathbf{l} and the same amount of distortion to the coefficients in \mathbf{G} (with respect to the energy in \mathbf{l} and \mathbf{G} , respectively). The sparse reconstruction algorithm provides the temperature reconstruction with the error shown in Figure 4.6(b). Due to the distortion, the estimate $\hat{\mathbf{m}}^s$ is not K -sparse but has K large coefficients while the others are close to zero. Choosing the positions of the K largest coefficients and fixing them as the correct positions, we can reduce the initial M number of unknowns in \mathbf{m}^s , to the K chosen unknowns. The new coefficients can be recomputed using the least squares method (e.g. pseudo-inverse). The new error is shown in Figure 4.6(c). However, it should be noted that the success of the least squares method is directly related to the correctness of the K positions found in the l_1 optimization method. \square

Example 4.3.2 (Sparsity in cosine basis domain). In the second scenario, we assume that the temperature is smooth in the region of interest. It is known

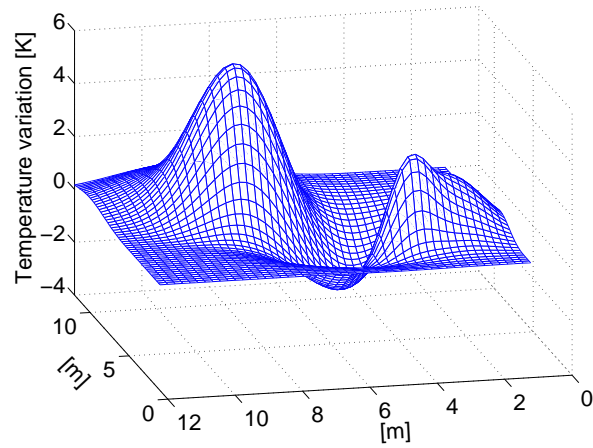
that smooth signals are sparse in the Fourier domain (when comparing to the signals with discontinuities). Hence, the temperature can be represented using a sparse vector of the Fourier coefficients. It is assumed that the temperature distribution is a sum of $K = 20$ cosine basis functions that are randomly chosen from a set of $M = 484$ cosine basis functions. To make use of the diffusion in the reconstruction, one needs to compute the basis elements that are the diffused version of the original basis elements. As previously explained, the new basis elements are found by convolving the original elements with the diffusive kernel. In the case of the Fourier domain representation, the convolution is replaced by multiplication. The way to write the new system of equations is the same as in (4.15). In this setup, we take the measurements in 3 time slots, which results in $N = 192$ measurements in total. Again, to model the effect of noise and the model mismatch we add 30 dB of distortion, both to \mathbf{l} and \mathbf{G} . Due to the noise in the system, we run the optimization for the noisy case given in (4.12).

The original temperature and the reconstruction errors are shown in Fig. 4.7. As in the previous example, the reconstruction error is largely reduced when the additional step of least square minimization is applied. \square

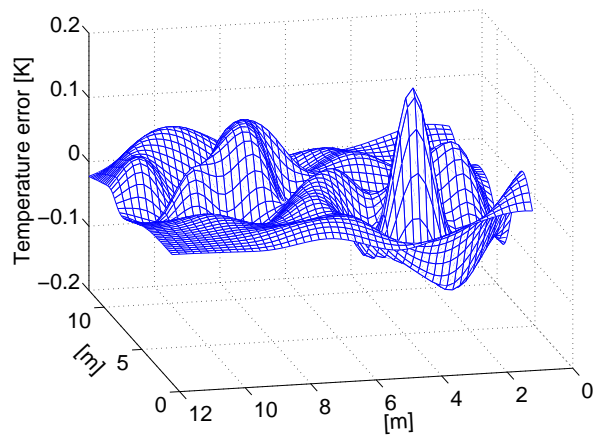
4.3.4 Discussion

We can see that the proposed method exhibits good reconstruction accuracy for both scenarios, and shows robustness to the noise and model mismatch. Moreover, having a limited number of measurements, predefined by practical constrains (e.g. number of transducers, number of channels of the acquisition card), this method can potentially increase the resolution of reconstructed images with respect to the methods that minimize the l_2 -norm error. The direct comparison between the methods presented in this chapter will be given in Section 4.5. Practically, there are some difficulties in choosing the “optimal” parameter α in (4.12) when the order of sparsity is not known. There exist algorithms that scan through the different values of α until the desired level of sparsity is satisfied. The complexity of the algorithms that perform the l_1 -norm minimization is still high, and is of the order of $O(M^3)$. The fast algorithms are currently under development. They would allow the use of the methods based on sparsity in medical applications, where a large number of transducers is employed, and a high resolution is desired.

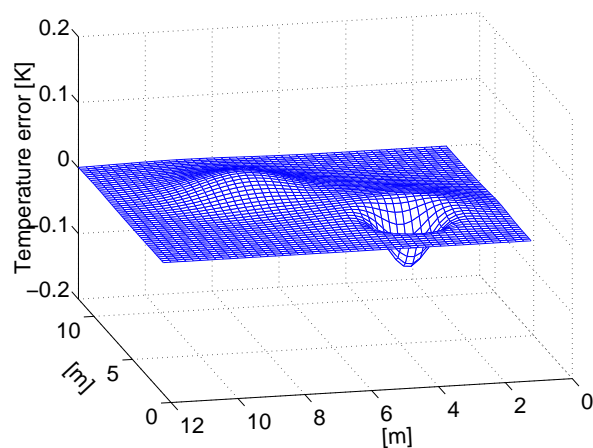
4.3. Temperature estimation in diffusive environment using the inversion based on sparsity



(a)

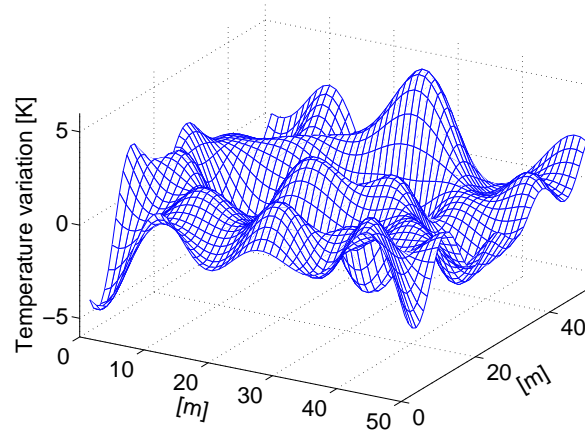


(b)

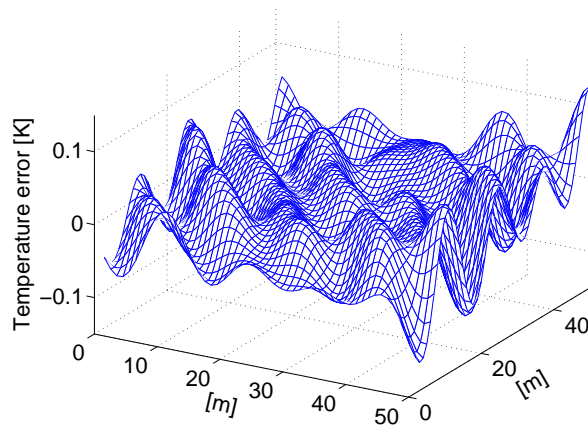


(c)

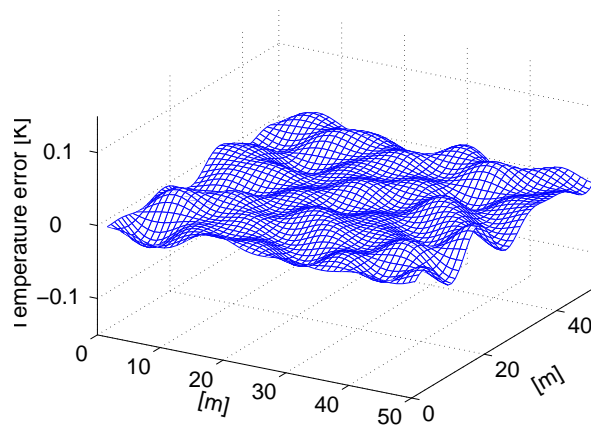
Figure 4.6: Sparsity in signal domain. The temperature distribution is supposed to be composed of $K = 5$ cubic splines that can have one of $p = 4$ possible widths, and they are arbitrary placed on the grid of $M = 12 \times 12 = 144$ nodes. (a) Original temperature distribution. (b) Reconstruction error after applying l_1 -norm optimization. (c) Reconstruction error after applying l_1 -norm plus reduced l_2 -norm optimization.



(a)



(b)



(c)

Figure 4.7: Sparsity in transform domain. The temperature distribution is supposed to be a sum of $K = 20$ cosine basis functions that are randomly chosen from a set of $M = 484$ functions. (a) Original temperature distribution. (b) Reconstruction error after applying l_1 -norm optimization. (c) Reconstruction error after applying l_1 -norm plus reduced l_2 -norm optimization.

4.4 Characterization of diffusive heat sources using the inversion based on FRI

In this section, we introduce a new inversion method for tomographic reconstruction. The method is based on the work proposed by Vetterli, Marziliano and Blu [74]. The authors in [74] provide exact sampling schemes for some classes of signals that are neither bandlimited nor live on shift-invariant spaces, namely, certain signals with finite rate of innovation (FRI). A common feature of such signals is that they have a parametric representation with a finite number of degrees of freedom per unit of time, or finite rate of innovation. We show that some of these sampling schemes can be extended for use in acoustic tomography, if the underlying fields have finite rate of innovation. This method can potentially provide an exact reconstruction of non-bandlimited fields using only a finite number of measurements.

Section 4.4.1 presents the idea of FRI sampling. In Section 4.4.2, we consider the problem of reconstructing different parameters of localized diffusive sources (e.g. localization, time origin, and the released amount) and show an example of heat sources. In Section 4.4.3, we show the simulation results. The concluding remarks are given in Section 4.4.4. In this section, for simplicity, we consider the straight-ray tomography model.

4.4.1 Sampling signals with FRI

In [74], it was shown that the signals that have a parametric representation with a finite number of degrees of freedom per unit of time, or finite rate of innovation ρ , can be perfectly reconstructed from a set of samples taken at a rate $R > \rho$, after appropriate smoothing. Equivalently, the direct reconstruction approach is exchanged for the reconstruction of the finite number of parameters or finite number of parameters per unit of time. The key in all constructions is to identify the innovative part of a signal, such as time instants of Diracs, using an annihilating or locator filter, a well-known tool from spectral analysis [67], or error correction coding [5]. This allows standard computational procedures for solving the sampling problem for a wide class of non-bandlimited signals. Examples include streams of Diracs, non-uniform splines and piecewise polynomials. The exact sampling schemes, for some classes of the 1-D and 2-D FRI signals, have been developed in [74, 45, 55].

While there are many signals that are characterized with a finite number of parameters, it is often difficult to propose practical sampling scheme. In our work, we extend some of the results formulated in [44] for a set of 2-D Diracs, and show how to apply them in a tomographic sampling scheme. Particularly, we consider localized instantaneous sources that reside in a 2-D diffusive environment.

4.4.2 Characterization of diffusive sources

We consider the problem of reconstructing a 2-D field induced by sources localized in space and time. Due to their localization in space and time, the sources can be modeled as a set of weighted Diracs. After the activation of a source, the induced field, although non-bandlimited, is completely determined by a

finite set of parameters, namely, the source location, its time origin and the total amount released. Intuitively, only a finite number of samples is required for perfect reconstruction.

A set of 3-D weighted Diracs is used to model the sources:

$$s(x, y, t) = \sum_{k=1}^K c_k \delta(x - x_k, y - y_k, t - t_k).$$

All diffusive processes are governed by diffusion, or equivalently the heat equation (4.13). At any point, we can compute the field as a convolution of the local sources with the heat kernel:

$$\Delta T(x, y, t) = [s * h](x, y, t) = \sum_{k=1}^K \frac{c_k}{4\pi D(t - t_k)} e^{-\frac{(x-x_k)^2 + (y-y_k)^2}{4D(t-t_k)}}. \quad (4.16)$$

The resulting field is simply a weighted sum of K 2-D Gaussians that diffuse over time. Notice also that $\Delta T(x, y, t)$ is completely determined by the parameters of the sources (c_k, x_k, y_k, t_k) , and it is therefore the signal with finite rate of innovation.

In the following, we envision three possible scenarios. The first one assumes that all Diracs appear at the same but unknown time. This assumption allows to obtain the exact reconstruction of the field $g(x, y, t)$. In the second scenario, the Diracs appear at different times, and only an approximate solution is proposed. In the third scenario, we consider different tracking problems.

All sources activate at the same time

In the following, for the sake of simplicity, we are first going to show the method for estimating the parameters $\{c_k, x_k, y_k\}$ assuming that the time origin t_k are all equal and known. The algorithm for estimating t_k will follow. The second algorithm does not require the knowledge of $\{c_k, x_k, y_k\}$ and, in practice, it should be applied first.

Retrieving the parameters $\{c_k, x_k, y_k\}$

Proposition 4.1. Let us assume that all Diracs appear at the same time $t_0 = 0$, and that we observe the system at time $t > 0$. This implies that, at the time instant t , we have

$$\Delta T(x, y, t) = \sum_{k=1}^K \frac{c_k}{4\pi Dt} e^{-\frac{(x-x_k)^2 + (y-y_k)^2}{4Dt}}. \quad (4.17)$$

The longitudinal interaction is then equal to:

$$l_\Gamma = \int_\Gamma \Delta T ds = \int_\Gamma \sum_{k=1}^K \frac{c_k}{4\pi Dt} e^{-\frac{(x(s)-x_k)^2 + (y(s)-y_k)^2}{4Dt}} ds. \quad (4.18)$$

The perfect reconstruction of $\Delta T(x, y, t)$ can be achieved with $2K + 1$ line integrals in (4.18).

4.4. Characterization of diffusive heat sources using the inversion based on FRI59

Proof: Let us assume that the measurement setup is such that we measure the time-of-flights along the trajectories parallel to the s -axis, as shown in Figure 4.8. For now, we also assume that the trajectories extends from $-\infty$ to $+\infty$. The case of finite length trajectories can be similarly solved, and it is going to be discussed at the end of this section. Changing the coordinate system to s - l system, the longitudinal interaction becomes

$$\begin{aligned} l_{\Gamma}(l) &= \int_{\Gamma_l=-\infty}^{\infty} \sum_{k=1}^K \frac{c_k}{4\pi Dt} e^{-\frac{(s-s_k)^2+(l-l_k)^2}{4Dt}} ds \\ &= \sum_{k=1}^K \frac{c_k}{\sqrt{4\pi Dt}} e^{-\frac{(l-l_k)^2}{4Dt}}. \end{aligned} \quad (4.19)$$

The longitudinal interaction $l_{\Gamma}(l)$ is a weighted sum of K 1-D Gaussians. The problem of reconstructing the parameters c_k and l_k from a finite number of measurements of the form in (4.19), taken along the trajectories $\Gamma(l)$, for $l = n\Delta l$, where Δl is a sampling interval in space, and $n = 1, \dots, N$, where $N \geq 2K + 1$, is already solved in [74]. For a fixed time t , the samples of $l_{\Gamma}[n] = l_{\Gamma}(n\Delta l)$ can be written as:

$$l_{\Gamma}[n] = \sum_{k=1}^K \left(\frac{c_k}{\sqrt{4\pi Dt}} e^{-\frac{l_k^2}{4Dt}} \right) \cdot e^{\frac{nl_k\Delta l}{2Dt}} e^{-\frac{n^2\Delta l^2}{4Dt}}. \quad (4.20)$$

If we let

$$\begin{aligned} S[n] &= l_{\Gamma}[n] \cdot e^{\frac{n^2\Delta l^2}{4Dt}}, \\ a_k &= \frac{c_k}{\sqrt{4\pi Dt}} e^{-\frac{l_k^2}{4Dt}}, \end{aligned}$$

and

$$u_k = e^{\frac{l_k\Delta l}{2Dt}},$$

then (4.20) is equivalent to

$$S[n] = \sum_{k=1}^K a_k u_k^n, \quad n = 0, \dots, N-1. \quad (4.21)$$

Note that, $S[n]$ is a linear combination of the real exponentials u_k . To compute u_k we need to find the so called annihilating filter $\mathbf{A} = [A[0] \ \dots \ A[K]]^T$, that satisfies

$$\begin{bmatrix} S[K+1] & S[K] & \dots & S[1] \\ S[K+2] & S[K+1] & \dots & S[2] \\ \vdots & \vdots & \ddots & \vdots \\ S[2K+1] & S[2K] & \dots & S[K+1] \end{bmatrix} \cdot \begin{pmatrix} A[1] \\ A[2] \\ \vdots \\ A[K+1] \end{pmatrix} = \mathbf{0}. \quad (4.22)$$

or, shortly

$$\mathbf{S} \cdot \mathbf{A} = \mathbf{0}.$$

It is actually true that the roots of the annihilating filter polynomial \mathbf{A} are exactly the u_k . The method is described in [74]. The coefficients a_k are then

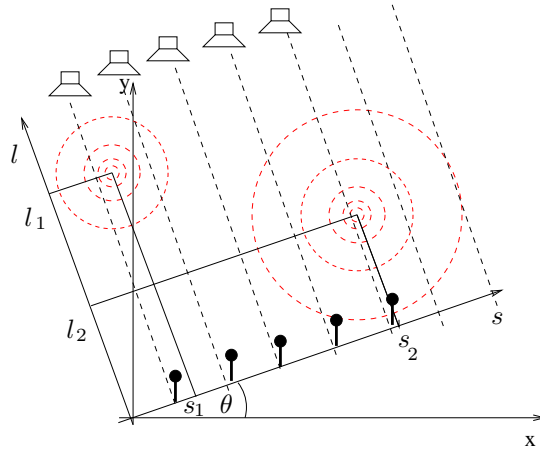


Figure 4.8: Sampling of 2-D Gaussians using the Radon projections. For the perfect reconstruction of 2 Gaussians we need only $2 \cdot 4 + 1$ samples of the Radon transform.

directly obtained using (4.21), as the solution of the system

$$\begin{bmatrix} u_1 & u_2 & \dots & u_K \\ u_1^2 & u_2^2 & \dots & u_K^2 \\ \vdots & \vdots & \ddots & \vdots \\ u_1^K & u_2^K & \dots & u_K^K \end{bmatrix} \cdot \begin{pmatrix} a_1 \\ a_2 \\ \vdots \\ a_K \end{pmatrix} = \begin{pmatrix} S[1] \\ S[2] \\ \vdots \\ S[K] \end{pmatrix}. \quad (4.23)$$

From u_k we find the positions l_k , and from a_k we find the weights c_k 's.

Since the set of locations l_k does not itself define the positions of the 2-D Diracs, we need more measurements of l_Γ , e.g. along the trajectories $\Gamma(s)$ that are now parallel to l -axis. Assuming also that $\Gamma(s)$ extends from $l = -\infty$ to $l = +\infty$, similarly as in (4.19), the longitudinal interaction becomes:

$$l_\Gamma(s) = \sum_{k=1}^K \frac{c_k}{\sqrt{4\pi Dt}} e^{-\frac{(s-s_k)^2}{4Dt}}.$$

Sampling the signal $l_\Gamma(s)$ at $s = n\Delta s$, where Δs is a sampling period in space, for $n = 0, \dots, N-1$, and $N \geq 2K+1$, and applying the annihilating filter method, we can first compute s_k and then the weights c_k . By comparing the weights computed from the first and second set of measurements, one can associate every l_k in the first set to the corresponding s_k in the second set. The proposed method gives the exact positions and weights if all l_k , s_k and c_k are distinct. The case where some of the parameters are equal can be resolved by taking the measurements of l_Γ along $K+1$ different orientation of Γ [44]. For the case of distinct parameters c_k , l_k and s_k , the signal is completely characterized by $2K+1$ samples of $l_\Gamma(l)$, and $2K+1$ samples of $l_\Gamma(s)$. ■

4.4. Characterization of diffusive heat sources using the inversion based on FRI61

Retrieving the time origin Assume now that we do not know the time origin $t_k = t_0$. Let us again consider the annihilating filter formula in (4.22). The entries of the matrix are annihilated by the K roots of the filter \mathbf{A} . The matrix \mathbf{S} has rank K , and it is rank deficient. If we write $S[n] = l_\Gamma[n] \cdot e^{\frac{n^2 \Delta l^2}{4D\Delta t}} = l_\Gamma[n] \cdot \alpha^{n^2}$, then we need to find such α for which

$$\mathbf{S} = \begin{bmatrix} l_\Gamma[K+1] \alpha^{(K+1)^2} & l_\Gamma[K] \alpha^{K^2} & \dots & l_\Gamma[1] \alpha \\ l_\Gamma[K+2] \alpha^{(K+2)^2} & l_\Gamma[K+1] \alpha^{(K+1)^2} & \dots & l_\Gamma[2] \alpha^2 \\ \vdots & \vdots & \ddots & \vdots \\ l_\Gamma[2K+1] \alpha^{(2K+1)^2} & l_\Gamma[2K] \alpha^{(2K)^2} & \dots & l_\Gamma[K+1] \alpha^{(K+1)^2} \end{bmatrix} \quad (4.24)$$

is rank deficient. This is not an easy task especially for noisy data. The straightforward method would be to search for α that minimizes the smallest eigenvalue. This method proves to be very unstable. Instead, we search for α that minimizes the effective rank [63]. This new measure represents how the energy is distributed among the directions of the eigenvectors and it can be seen as a continuous extension of the rank. The method largely outperforms the minimum eigenvalue approach (see Section 4.4.3).

General case

Assume that all Diracs appears at different time instants t_k . Let us rewrite the equation (4.19) as,

$$l_\Gamma(l, t) = \sum_{k=1}^K c_k h(l - l_k, t - t_k) u(t - t_k), \quad (4.25)$$

where $h(l, t) = \frac{1}{\sqrt{4\pi Dt}} e^{-\frac{l^2}{4Dt}}$ is a 1-D Gaussian, and $u(t)$ is the step function that ensures positive t . Taking the Fourier transform of (4.25), the shifts in space and time translate into the phase shifts:

$$L_\Gamma(\Omega_l, \Omega_t) = \sum_{k=1}^K c_k H(\Omega_l, \Omega_t) e^{-j\Omega_l l_k} e^{-j\Omega_t t_k}. \quad (4.26)$$

The term $H(\Omega_l, \Omega_t)$ represents the 2-D Fourier transform of $h(l, t)$, and can be computed as:

$$H(\Omega_l, \Omega_t) = \int \int \frac{1}{\sqrt{4\pi Dt}} e^{-\frac{l^2}{4Dt}} e^{-j\Omega_l l} e^{-j\Omega_t t} dl dt = \frac{1}{D\Omega_l^2 + j\Omega_t}.$$

As it does not depend on k , $H(\Omega_l, \Omega_t)$ can be taken out of the sum in (4.26). Finally, we get

$$L_\Gamma(\Omega_l, \Omega_t)(D\Omega_l^2 + j\Omega_t) = \sum_{k=1}^K c_k e^{-j\Omega_l l_k} e^{-j\Omega_t t_k}. \quad (4.27)$$

Evaluating the previous equation in $\Omega_l = 2\pi n/N\Delta l$ and $\Omega_t = 2\pi m/M\Delta t$ for $n = 0, \dots, N-1$, $m = 0, \dots, M-1$, where Δl and Δt are the sampling intervals

in space and time respectively, we obtain

$$L_{\Gamma} \left(\frac{2\pi n}{N\Delta s}, \frac{2\pi m}{M\Delta t} \right) \left(D \left(\frac{2\pi n}{N\Delta l} \right)^2 + j \frac{2\pi m}{M\Delta t} \right) = \sum_{k=1}^K c_k e^{-j \frac{2\pi n l_k}{N\Delta l}} e^{-j \frac{2\pi m t_k}{M\Delta t}}. \quad (4.28)$$

Notice that, on the right-hand side of (4.28) we have a linear combination of K complex exponentials. Fixing, for example, $m = 0$ and taking the samples for $n = 0, \dots, N - 1$, we can again apply the annihilating filter method and compute the roots $e^{-j \frac{2\pi n l_k}{N\Delta l}}$ from which we obtain the positions l_k . Repeating the same steps for $n = 0, m = 0, \dots, M - 1$ we can compute the time instants t_k . The coefficients c_k can then be directly obtained from (4.28). Similarly, but taking another set of measurements, e.g. of the form $l_{\Gamma}(s)$, and computing the corresponding Fourier transform, we will be able to compute s_k positions as well.

The only problem in the previous derivation is that the Fourier transform of $l_{\Gamma}(l)$, or $l_{\Gamma}(s)$, is not available in practice, since we only have a finite number of samples of $l_{\Gamma}(l)$, or $l_{\Gamma}(s)$. However, L_{Γ} can be approximated by its Discrete Fourier Transform (DFT) coefficients,

$$L_{\Gamma} \left(\frac{2\pi n}{N\Delta s}, \frac{2\pi m}{M\Delta t} \right) \approx \Delta t \Delta l L_{\Gamma}^{\text{DFT}}[n, m]. \quad (4.29)$$

We remark that (4.29) is only an approximation because the DFT coefficients are aliased. The aliasing decreases as the time t increases since $L_{\Gamma}(\Omega_l, \Omega_t)$ is becoming more and more bandlimited-like. This means that for an appropriate t , one can minimize the total effect of aliasing and noise, and optimize the estimation.

Tracking

Using the previous results, different tracking algorithms can be imagined. For example, assume that the heat sources are divided in groups and that each group can appear at different time instants. If we take the measurements over time fast enough, so that no more than one group of Diracs appear in the same sampling interval, then the exact reconstruction method can be derived from the previous results for the case when all Diracs appear at the same time. It is sufficient to compute the predicted field that is generated by the sources activated so far, i.e. $l_{\Gamma}^{i-1}[n, t]$, and to subtract that from the current state $l_{\Gamma}^i[n, t]$,

$$l_{\Gamma}^i[n, t] - l_{\Gamma}^{i-1}[n, t] = \sum_{k=0}^{K-1} \frac{c_k}{\sqrt{4\pi D(t-t_i)}} e^{-\frac{(n\Delta l - t_k)^2}{4D(t-t_i)}}.$$

The resulting signal is a sum of K Gaussians with the same variance $\sigma^2 = 2D(t - t_i)$, where t_i is the time origin of the i -th group. The parameters c_k, l_k, t_i can be found by applying the previously proposed scheme. If more than one Dirac with different time origin appear in the same sampling interval, then the approximate results derived for the general case can be used.

4.4. Characterization of diffusive heat sources using the inversion based on FRI63

The effect of finite line integration for l_Γ

Assume that the acoustic transmitters and receivers are placed around a certain region of interest, as shown on Figure ??, and that we can measure the time-of-flight from the transmitter located at the position s_T to the receiver located at the position $s_R = 0$. Then, (4.19) should be changed to

$$\begin{aligned} l_\Gamma(l, t) &= \int_0^{s_T} \sum_{k=1}^K \frac{c_k}{4\pi Dt} e^{-\frac{(l-l_k)^2 + (s-s_k)^2}{4Dt}} ds \\ &= \sum_{k=1}^K \frac{c_k}{\sqrt{4\pi Dt}} \left(\operatorname{erf}\left(\frac{s_k}{\sqrt{4Dt}}\right) + \operatorname{erf}\left(\frac{s_T - s_k}{\sqrt{4Dt}}\right) \right) e^{-\frac{(l-l_k)^2}{4Dt}}. \end{aligned}$$

Similarly,

$$\begin{aligned} l_\Gamma(s, t) &= \int_0^{l_T} \sum_{k=1}^K \frac{c_k}{4\pi Dt} e^{-\frac{(l-l_k)^2 + (s-s_k)^2}{4Dt}} dl \\ &= \sum_{k=1}^K \frac{c_k}{\sqrt{4\pi Dt}} \left(\operatorname{erf}\left(\frac{l_k}{\sqrt{4Dt}}\right) + \operatorname{erf}\left(\frac{l_T - l_k}{\sqrt{4Dt}}\right) \right) e^{-\frac{(s-s_k)^2}{4Dt}}. \end{aligned}$$

The parameters (c_k, l_k, s_k, t_0) can be found by applying the algorithms previously introduced.

4.4.3 Simulation results

In the following, we present the simulation results. The setup consists of two local heat sources (2D Diracs). The parameters of the sources are randomly chosen in the intervals: $c_k \in (0.5, 10)$, $x_k, y_k \in (0, 4)$. All Diracs appear at the same time.

We first tested the time search algorithm. According to (4.24) we need to search for α that makes the matrix \mathbf{S} rank deficient. In the case of the effective rank (ER) criterion, the minimum ER corresponds to the largest discrepancy in the eigenvalues distribution. Therefore, the optimal α is the one that contributes most to the clear differentiation between the signal and noise space. In Figure 4.9, we plot the ER and the minimum eigenvalue of \mathbf{S} with respect to α . For comparison purpose, the matrix \mathbf{S} is normalized and the results are scaled to the interval $[0, 1]$. In the noiseless case, the two methods provide the correct answer $\alpha_{opt} = 1.04$ (see Figure 4.9(a)). In the noisy scenario (SNR=45dB for the samples $l_\Gamma[n]$), the ER clearly outperforms the singular value approach which basically provides no insight about the optimal solution (see Figure 4.9(b)).

Figure 4.10(a) shows the performance of the position finding algorithm proposed in Section 4.4.2. This algorithm is known to be very unstable for the case of noisy data. Therefore, we use the successful variation of the original algorithm, that is developed in [43]. Good estimates are obtained by performing oversampling in space with $N = 5(2K + 1)$. The relative MSE represents the mean square of the relative error of the positions. The algorithm gives good results for SNR > 40 dB. Figure 4.10(b) shows one reconstruction example.

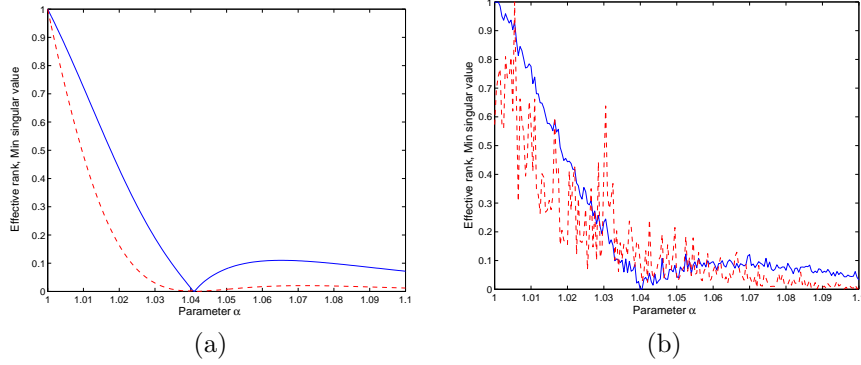


Figure 4.9: Comparison of the time origin search algorithms: the first one searches for the α that minimizes the effective rank (plain) measure and the second one searches for the α that minimizes the smallest singular value (dashed). The optimal α is 1.04. (a) Noiseless case. (b) Noisy case (SNR= 45dB).

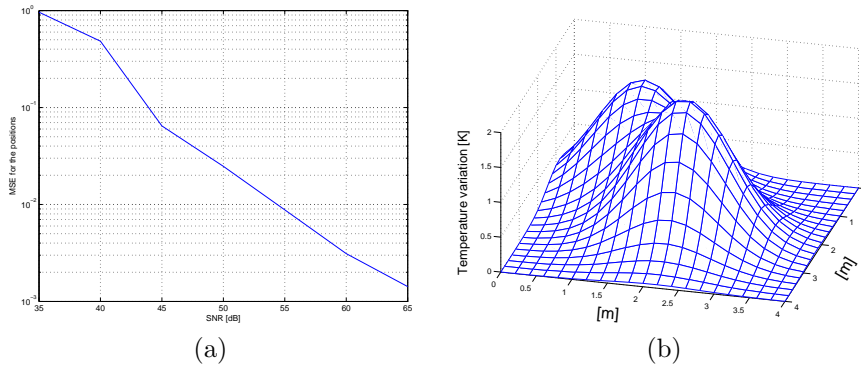


Figure 4.10: (a) Relative MSE for the position estimation, (b) The reconstruction of two 2D Diracs. The samples of the Random transform are computed along the dashed lines.

4.4.4 Discussion

This method provides an exact solution to the problem of tomographic sampling of the signals with finite rate of innovation. However, the system to solve is non-linear

$$\mathbf{G}m(\Theta) = \mathbf{d} \quad \text{where} \quad \Theta = [c_k, x_k, y_k, t_k]$$

with respect to the parameters c_k , x_k , y_k , and t_k . The drawback of the method is that sometimes it is not robust enough to noise. To overcome this problem special algorithms as the one in [43] needs to be developed.

4.5 Conclusions

In this chapter, we introduced three different methods for tomographic inversion. The first method, namely the l_2 -norm minimization, is most conventional and can be applied in any configuration. We show that it can be successfully incorporated into the non-linear tomography algorithm. The use of other two inversion methods, namely, the inversion based on sparsity, and the inversion based on FRI, present novel approaches to the tomography inversion. These two methods are not studied in the context of the non-linear tomography inversion but as separate methods. They both show the improvement in terms of the quality of the reconstruction with respect to the classical inversion techniques, but they are both based on a particular solution model. For the comparison purpose, in case of a circular array and the uniform Radon sampling (uniform spacing between the transducers, and uniform rotation steps of the circular setup) if N is the total number of measurements, we would be able to resolve M unknowns (e.g. grid points inside the region of interest) where,

1. $M = O(N)$ for the inversion based on l_2 -norm minimization,
2. $M = O(e^{\frac{N}{K}})$ for the inversion based on sparsity,
3. $M = \infty$ when $N > 2K + 1$, and the inversion is based on FRI.

However, we have to add that in noisy cases the method based on FRI is sometime ill-conditioned. Still there is an immense potential improvement of the two methods based on sparsity and FRI.

Part II

Applications

Chapter 5

Breast Cancer Detection

Acoustic or more precisely ultrasound tomography has received much attention in the area of medical imaging. When an ultrasound wave propagates through tissue, it can be scattered, absorbed, refracted, and can undergo a change in velocity. The measurements of these interactions, their frequency, and temperature dependence can provide important information on fundamental properties, such as the density and bulk modulus. Moreover, tissue motion can be measured by Doppler methods. The extraordinary potential of ultrasound to diagnose tissue state is also the source of its major weakness. Because of the existence of so many different interactions, it is difficult to isolate any one in particular. The three major interactions amenable to measurement are: sound speed, attenuation, and scattering. In this work, we measure sound speed in tissues.

The sound speed distribution in a tissue may well be its most critical acoustic property. In the first place, it has intrinsic significance as a means to describe the tissue structure, particularly underlying tissue densities and tissue “stiffness”. Second, the accuracy and the resolution of an image of any other acoustic parameter can be profoundly affected by the sound speed distribution in the tissue. Specifically, as the sound speed distribution determines the propagation of sound waves, this information can be used to correct images of any other tissue acoustic parameter, e.g. the attenuation or the reflection. Third, the sound speed distribution is intimately associated with the scattering behavior of tissue, the interaction most often observed in clinical diagnosis. For example, if one is able to obtain both sound speed and scattering images of one region, one could in principle compute the density distribution in that region.

Next to its indirect contribution to the imaging of other acoustics parameters, sound speed distribution has an important direct role in differentiating cancers from normal breast tissue. Namely, previous *in vitro* studies [28] indicated that cancerous tissue has a high sound speed and also attenuation when compared to normal tissue or benign masses. Therefore, sound speed is a good parameter used to distinguish benign masses from cancers. The sound speed difference over fat is even greater, leading to potential characterization of masses in even heterogeneously dense breasts.

In this chapter, we investigate the use of ultrasound tomography to breast cancer detection. We use the inverse method presented in Chapter 4. The chapter is organized as follows. In Section 5.1, we motivate the use of ultrasound

for breast cancer detection. The experimental setup is presented in Section 5.2. Signal acquisition and time-of-flight estimation is studied in Section 5.3. We propose beamforming techniques to overcome some current problems in the breast screening with ultrasound tomography. The experimental results are shown in Section 5.4, and the conclusions are given in Section 5.5.

5.1 Breast cancer detection with ultrasound

Breast cancer is the most frequently diagnosed cancer in women. In 2006, breast cancer was the most common form of cancer in Europe with 429,900 cases, that is 13.5% of all cancer cases. The incidence of breast cancer is increasing. Although mammography is the gold standard for breast imaging, it also generates many abnormal findings not related to cancer leading to a false positive rate associated with diagnosing breast masses that can be as high as 80%. The differentiation of benign from malignant tissue in mammogram findings is as well very poor for young women and women with dense breasts, and results in 50% of false negative rate. To overcome this problem, mammography is, therefore, generally complemented by ultrasound which helps differentiate cysts from solid masses and has become the dominant mode for guiding needle biopsy. Efforts to improve the diagnostic accuracy of ultrasound have been carried out on two fronts. One approach is based on improving the classical ultrasound devices and techniques that rely on reflection (or B-mode) imaging while the second, to which our own study belongs, utilizes transmission tomography to characterize masses.

Greenleaf *et al.* [28] have demonstrated that using the parameters of sound speed and attenuation could help to differentiate benign masses from cancer. As a direct result of this and similar studies, a number of investigators developed transmission ultrasound scanners in an attempt to measure transmission parameters *in vivo*, e.g. the work of Carson *et al.* [13], Andre *et al.* [1], Johnson *et al.* [32], Marmarelis *et al.* [46], Liu and Waag [42], and Duric *et al.* [24]. Our own contribution to this contemporary body of research came as a result of a collaboration with the latter research group from the Karmanos Cancer Institute in Detroit, USA. They have developed the Computed Ultrasound Risk Evaluation System (CURE), the clinical breast imaging device that aims at whole breast, operator independent imaging, and differentiation of breast masses. Although the system can use both ultrasound reflection and transmission tomography, we only focused on the transmission part and the sound speed estimation. In order to improve the final image quality in terms of estimation accuracy and resolution we have worked both on the acquisition part of the system, that is enhancement of the received signal, and the inversion part, that is employing different inversion methods.

5.2 Experimental setup

The Computerized Ultrasound Risk Evaluation (CURE) device is a clinical prototype tomographic ultrasound scanner. The system was designed at the Karmanos Cancer Institute (KCI), Detroit. Figure 5.1(a) depicts the patient setup for the CURE scan, which is markedly different than that for mammog-

raphy or conventional ultrasound. The patient is positioned prone with the breast situated through a hole in the canvas bedding so that the breast is suspended in the water tank. Figure 5.1(b) shows an enlargement of the imaging tank, with the transducer ring that translates in the vertical direction to image the entire breast volume. The 20 cm diameter ring transducer, with an operating frequency of 1.5 MHz, encircles the breast and begins scanning near the patient's chest wall. The ultrasound signal is sequentially transmitted by each element and subsequently received with all 256 elements situated around the ring. This sequence is then repeated for each transmitting element, taking approximately 0.1 seconds to acquire a full slice, and approximately 45 – 60 seconds for a full breast scan including the chest wall. A motorized gantry translates the ring along the breast, ranging from near the chest wall through the nipple region. One complete scan leads to approximately 45 – 75 tomographic slices of data per patient, taking about one minute to image the entire breast volume.

The operator can choose the form of the signal that is going to be sent by the transducers, and upload it in a digital form with the sampling frequency of 16.66 MHz. At the receiver's side the 256 received signals are sampled at two optional frequencies that are 6.25 MHz and 8.33 MHz. The data are then transferred to the PC workstation for image reconstruction.

5.3 Signal enhancement and time-of-flight estimation

The choice of signal processing tools and parameters to be applied in a particular problem needs to be carefully tailored to the specificity of the problem. To this end, a comprehensive analysis of what we have as a priori information and what we need will be done. First, we are going to study the raw signal characteristics in Section 5.3.1, and the importance of having a reference signal will be justified in Section 5.3.2. In Section 5.3.3 we show how the signal-to-noise ratio can be increased, and in Section 5.3.4 two time-of-flight estimation techniques are compared.

5.3.1 Raw signal analysis

In most of the experiments the signal sent to the transmitters is a short impulse generated as a half or a quarter cycle of a sinusoid of frequency 1.5 MHz. This signal travels from the transmitter through the water and the object of interest to the receivers, and on its way it is transformed by the transfer function of the transmitters, water, object, and receivers.

Let us identify important parts of the signal. Figure 5.2 shows a typical received signal for *in vivo* data. The receiving buffer is triggered as the transmission starts. Before the main signal arrives, the receivers record the noise with the exception that at the very beginning there is a part of the transmitted signal that travels directly through the frame of the ring (with a high sound speed). However, so far neither part of the received signal is of our interest. Once the signal arrives we have a main signal part. Soon after there are late arrivals that are caused by reflections, refractions or the part of the signal that travels on the surface of the object, hereafter referred as a surface wave signal.



(a)



(b)

Figure 5.1: Clinical prototype of the CURE device. (a) CURE system workstation and patient bed. The workstation is used to set the scanning parameters. The patient lies on the bed, in the prone position, with the breast suspended through a hole in the table, in the water tank just below the table surface. The various components of the system are labeled. (b) Close up of the imaging tank showing the transducer ring affixed to a mechanical arm that steps the ring down while imaging the entire breast volume.

No matter what the cause of the late arrivals is, they are an undesirable part of the received signal. Moreover, they are sometimes less attenuated, and they might be very close in time to the component associated to the main signal.

Thus, they can appear as a dominant signal on the receiver side. Such situations are shown in Figure 5.2(b), where the late arrival can be separated in time from the main signal, but it has a higher amplitude than the correct signal part. Even worse is the case in Figure 5.2(d), where the main signal and the late arrivals are inseparable. Therefore, it is usually very difficult to distinguish the late arrivals from the main signal, and to compute the correct time-of-flights. Also, as we can see from the *in vivo* data shown in Figure 5.2 the main signal is attenuated and the SNR is low. This additionally complicates the time-of-flight estimation. Ideally, we want to enhance the direct (main) signal and to suppress the late arrivals at the same time. A simple solution based on increasing the power of the transmitted signal does not work since the power of the late arrivals is increased proportionally. The use of a longer pulse can reduce the error in time-of-flight estimation; however, it increases the probability of having the overlap between the main and the late arrivals.

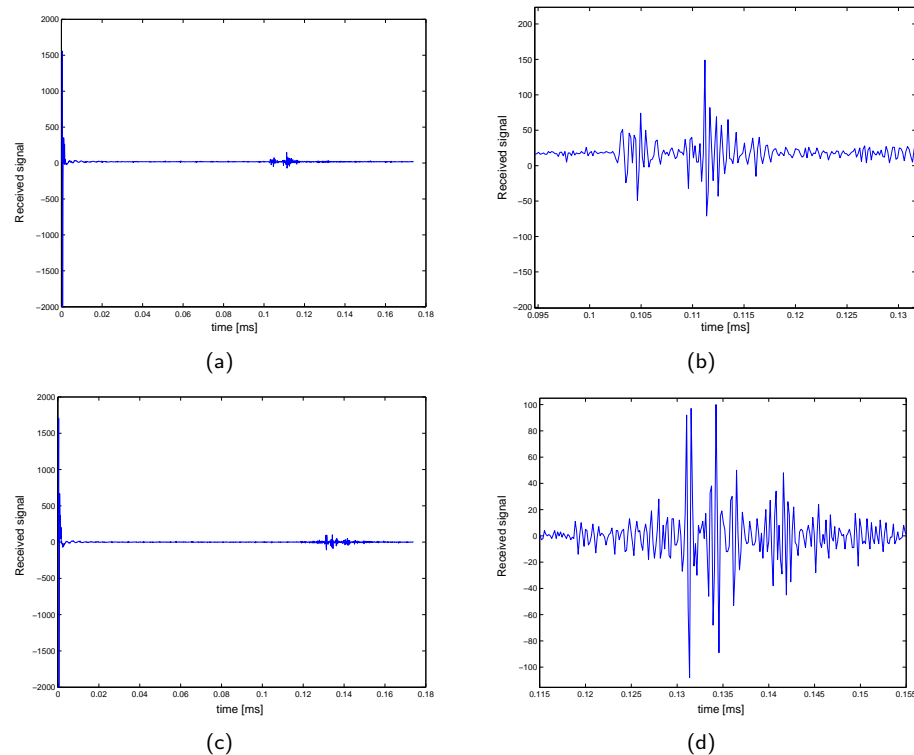


Figure 5.2: Examples of the received signal. (a) First example. (b) Detail of the previous signal. The late arrival can be separated in time from the main signal, but it has a higher amplitude than the main signal part. (c) Second example. (d) Detail of the previous signal. The late arrivals and the main signal are not separable in this case.

5.3.2 Reference signal

The water has well defined sound speed properties and, therefore, the signal sent through the water can serve as a reference. Having a sound speed reference allows to estimate only the sound speed variation instead of the absolute value. Intuitively, this is an easier problem to solve because the systematic error that can appear when estimating the absolute sound speed can be avoided if we estimate only the variation. For example, the delays of the transducers, all electronic delays, and the transducers positions, although carefully taken into account, are never perfectly estimated and they are potential sources of the systematic error. Since the same systematic error appears in the time-of-flight of the reference signal, it is going to be canceled when the difference between these two time-of-flights is computed. Another advantage of having a reference signal is that it contains information about the transfer function of the transducers that is usually unavailable. This information can be useful when computing the time-of-flights.

The ability to provide a reference signal in acoustic transmission tomography is a great opportunity of this method and an important advantage over the reflection tomography methods.

5.3.3 Signal preprocessing

Low SNR is the main factor responsible for inaccurate time-of-flight estimation, especially when the estimation is based on amplitude thresholding. Among many techniques used to increase the SNR, we study the most common one that is filtering, and also propose a new technique for ultrasound tomography imaging based on beamforming.

Filtering with a bandpass filter is used to cut the noise that appears outside the bandwidth of the signal. However, the signal that we send has a high bandwidth and it is bandpassed by the transfer function of the transmitter and the receiver. We can choose to bandpass the received signal around the resonant frequency of the transducers (1.5 MHz), that would eliminate the noise outside the filter bandpass but, it would also distort the signal itself. To stay consistent, we need to apply the same filtering to the reference signal. The two signals can then be fairly compared. However, when the SNR is low, e.g. $\text{SNR} = 0$ dB, we prefer to use a technique that does not distort the signal, and one of these technique is beamforming.

Beamforming is a signal processing technique used with arrays of transmitters or receivers that control the directionality of a radiation pattern. When receiving a signal, the so called *receive beamforming* can increase the receiver sensitivity in the direction of wanted signals and decrease the sensitivity in the direction of interference and noise. When transmitting a signal, the so called *transmit beamforming* can increase the power along the chosen direction. Therefore, using beamforming we can enhance the signal in a particular direction and suppress noise and reflections coming from other directions. To this end, we use a simple *delay and sum beamformer*.

Delay and sum beamforming is quite true to its name as it merely takes the set of signals, delays and maybe weights them by varying amounts, and then adds them all together. The delays are determined by the direction (for farfield) or point (for nearfield) at which the array or transmitters or receivers

is aimed. Despite its simplicity, delay and sum beamformer manages to achieve optimal noise suppression for the case of a point source in a background of white noise. In this work, we use the delay and sum beamformer for the nearfield case. Both the transmit and the receive beamformer are implemented. However, this technique is powerful but also sensitive to the delays that need to be applied to the transmit and the received signals. The details on how to compute the correct delays of the beamformer are presented in our patent [35].

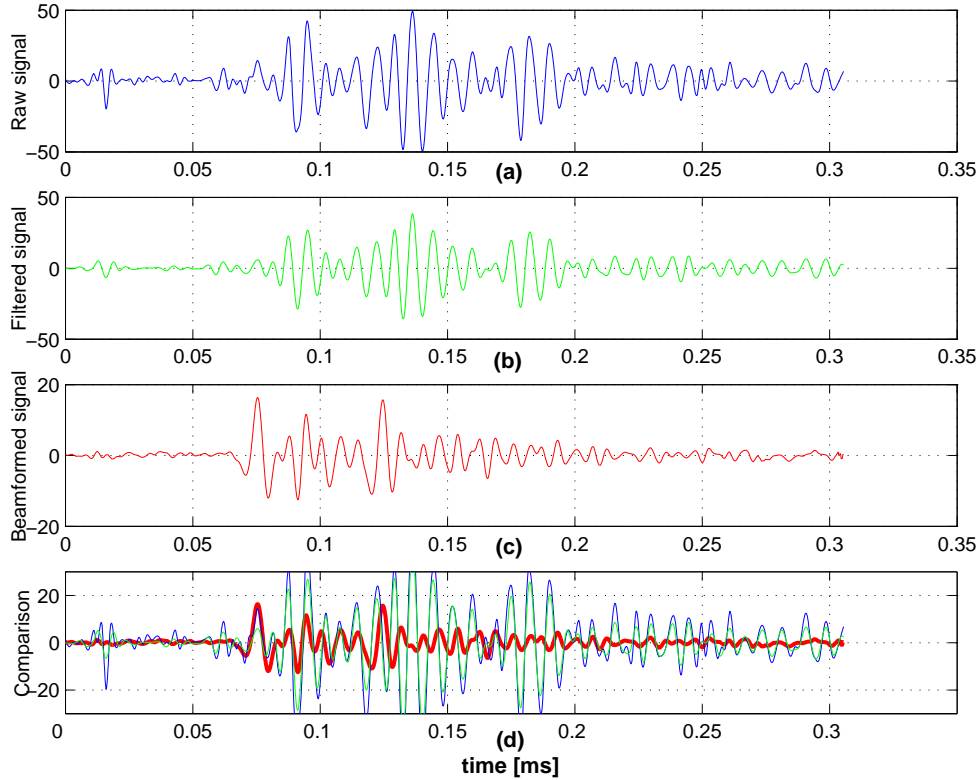


Figure 5.3: Signal processing in order to increase SNR. (a) Raw signal; (b) Filtered signal; (c) Beamformed signal; (d) The raw, filtered and the beamformed signals are superimposed for a comparison purpose. We can clearly see the advantages of beamforming: it decreases the noise and annihilates the late arrivals.

The effects of filtering and beamforming used to enhance the received signal are presented in the following example. Figure 5.3(a) shows a segment of a raw received signal, obtained from *in vivo* measurements with the CURE scanner. The received signal contains the direct signal (short pulse) and the late arrivals, but, in this particular example, it is not possible to determine the beginning of the direct signal. Figure 5.3(b) represents the filtered version of the raw signal. The filtering is done using a passband filter with the stop corner frequencies at 0.45 MHz and 2.55 MHz, and the pass band corner frequencies at 0.75 MHz and 2.25 MHz. The filter is designed as an optimal equiripple FIR filter using the Parks-McClellan FIR filter design procedure (implemented in Matlab under the

function `remez`). Analyzing the filtered signal, we can conclude that filtering distorts the signal and for the low SNR it does not reveal the main signal. In Figure 5.3(c) we show the result after applying the beamforming to the raw signal. Both the transmit and the receive beamforming is applied using 7 transmitters and 7 receivers for each beamforming process. As we can see, the noise level is dramatically decreased and we can clearly see where the main signal starts. The late arrivals are suppressed as well, comparing the raw signal and its filtered version. Since the beamforming showed to be very efficient in our setup, we decide to use it without any filtering.

5.3.4 First peak arrival versus cross-correlation method

We estimate the time-of-flight between every transmitter and receiver by comparing the received signal when the object is present, hereafter referred as signal, with the received reference signal. Both the signal and the reference are obtained after applying beamforming. We compute the time-of-flight difference between the signal and the reference. This can be done by searching for the beginning of the two signals and comparing the two positions, but sometimes this can be very difficult due to the ringing of the transducers. Namely, the transducers do not respond instantaneously to the excitation but only after a transition period. Instead, we search for the first significant peak of the two signals and compare their positions (as explained in Section 3.3.2). The correct time delay is obtained as a sum of the difference between the two delays and the time delay of the reference that is computed from the positions of the transducers and the known sound speed.

Another option to estimate the time-of-flight is to compute the cross-correlation between the reference and the signal. The peak of the cross-correlation determines the time delay between these two signals. Since the medium is very heterogenous and the signal contains many reflections and refractions the cross-correlation will have many peaks and the highest peak will not necessarily be the right one. Depending on the signal energy contained in the first arrival comparing to the late arrivals, the first peak might be smaller than the later peaks.

The cross-correlation method will be used when the signal does not undergo strong attenuation, and the result will be compared to the first peak arrival method.

5.4 Results

The time-of-flights are used to construct the maps of the sound speed distribution. The region of interest ($20 \times 20 \text{ cm}^2$) is covered with the rectangular cells and the value of the points inside the cells is constant. There are 150×150 rectangular cells in total. The sound propagation is modeled using the equations of sound propagation introduced in Chapter 3, and assuming that the medium is not moving, i.e. $\mathbf{v} = 0$. A fifth-order Runge-Kutta algorithm is applied to integrate the ray equations forward in time. Since the medium is heterogenous the use of the bent ray model is highly beneficial. The correct rays are found using the shooting method. The algorithm has an adjustable step size and error tolerance at the receiver side. The solution is computed us-

ing the iterative algorithm described in Section 3.6.1. The method alternates between estimating the sound ray trajectories and the sound speed.

We perform sound speed reconstruction for the *in vitro* and *in vivo* data. In the following examples, we compare the effect of two techniques for time-of-flight estimation, namely the first peak arrival and the cross-correlation method. The effect of enhancing the raw signal using the beamforming techniques is also presented.

5.4.1 In vitro study

For the in vitro study, we use an anthropomorphic breast phantom (see Figure 5.4(a)), constructed by Dr. Ernest Madsen of the University of Wisconsin, that provides tissue-equivalent scanning characteristics of breast tissue. Materials characteristic of fat and fibroglandular tissue contain masses ranging in size from 6 to 14 mm with varying mass densities. The coronal slices of the phantom are scanned with the CURE system. For a comparison, coronal CT reconstructions of the phantom were evaluated as well (Siemens Somatom Sensation CT scanner, 1 mm thick axial slices, coronal reconstruction thickness = 1 mm, mAs = 140, topogram length = 256 mm, B31 medium smooth reconstruction kernel). Because CT yields map of rescaled linear attenuation coefficients, the CT numbers are characteristic of the material composition and density, and we use the CT scan to localize the inclusions inside the phantom (see Figure 5.4(b)).

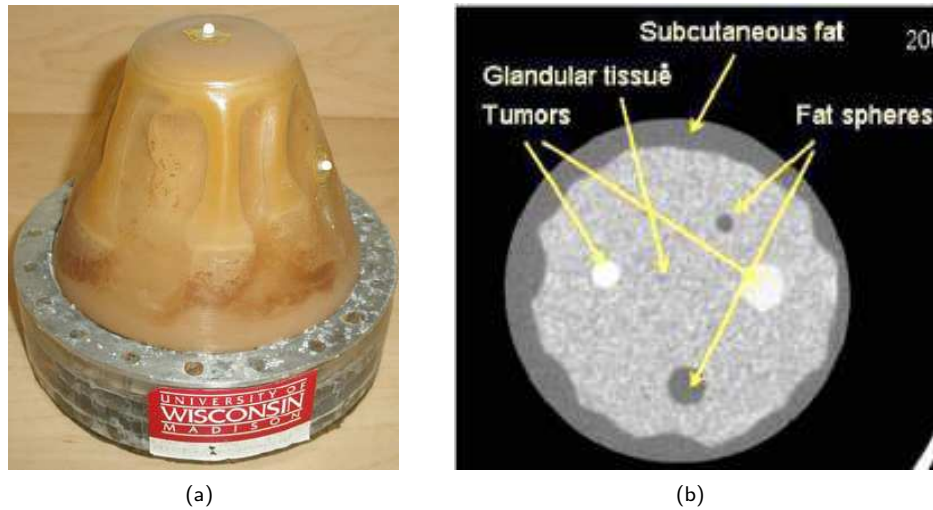


Figure 5.4: Breast mimicking phantom. (a) Anthropomorphic breast phantom constructed by Dr. Ernest Madsen of the University of Wisconsin. (b) CT scan of the phantom with specified inclusions.

Starting from the same set of raw data, we first compute the time-of-flights using two different estimation techniques, namely, the first peak arrival and the cross-correlation method. In both cases the differences between the time-of-flight through the object and the time-of-flight through the water are computed. Figure 5.5 shows the time-of-flight differences for one transmitter and

all receivers. The results of both techniques are similar since the power of the received signal was sufficient to insure the correct results. The outliers in both techniques indicate the points when the methods fail, since the result is expected to be smooth.

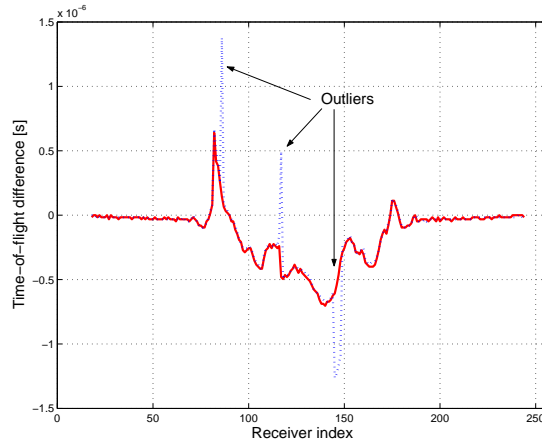


Figure 5.5: Time-of-flight differences with respect to the reference time-of-flights in the water. The delays are computed for a fixed transmitter and all receivers, using the cross-correlation (· ·) and the first peak arrival (-) method.

More direct comparison requires the final reconstruction images. Figure 5.4 represents the reconstructions for two different time-of-flight estimation techniques, namely for the first peak arrival (Figures 5.6(a) and 5.6(b)) and the cross correlation method (Figures 5.7(a) and 5.7(b)). The effect of beamforming is shown in Figures 5.6(b) and 5.7(b). All the reconstructions show a high resemblance in the region of the phantom. More differences are visible around the phantom where the ray-like artifacts can be noticed. Comparing the images, we conclude that the first peak arrival gives better reconstruction and that the beamforming clearly improves the reconstruction in both techniques.

The best reconstruction, i.e. the reconstruction in Figure 5.6(b), is compared in more detail to the CT scan of the phantom in Figure 5.8. The inclusions are well localized and the computed sound speed corresponds to the expected sound speed. The effect of smoothing that is inherent in the tomographic reconstruction is also present. Therefore, the reconstructed sound speed inside the inclusions is smoothed depending on the value of the sound speed in the surrounding tissue.

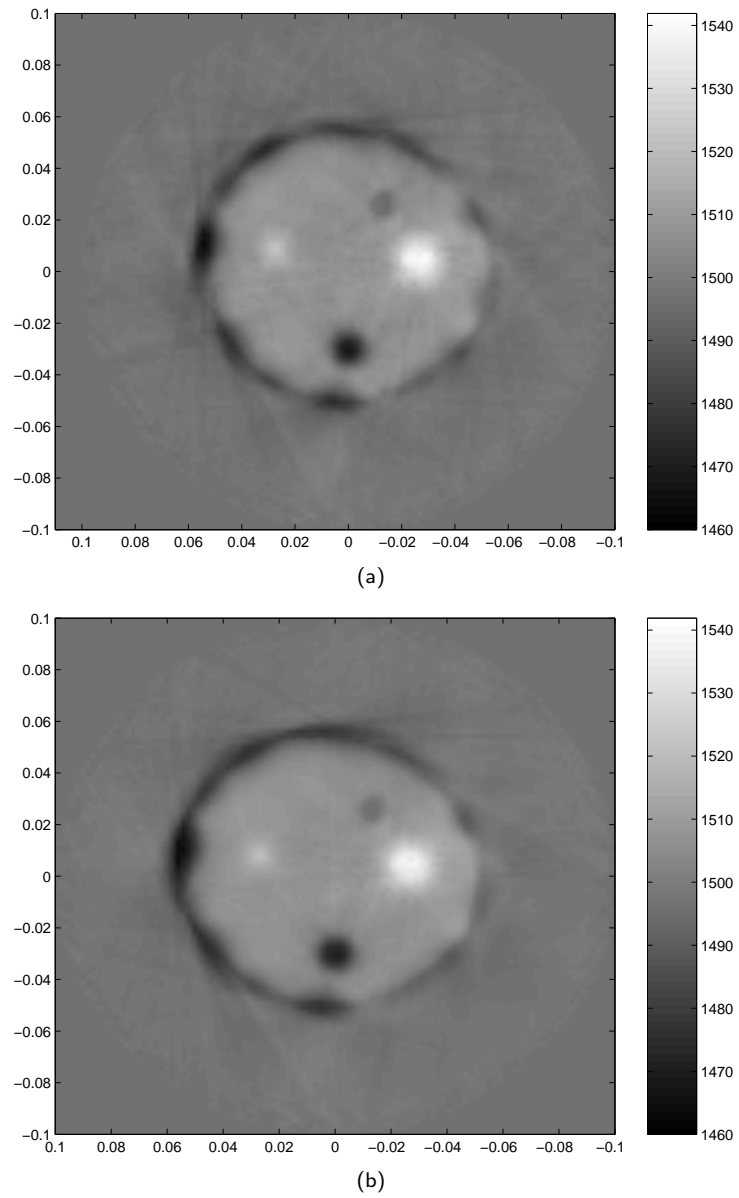


Figure 5.6: Sound speed reconstruction for the phantom study. The time-of-flights are computed using the first peak arrival method. (a) Without beamforming. (b) With beamforming.

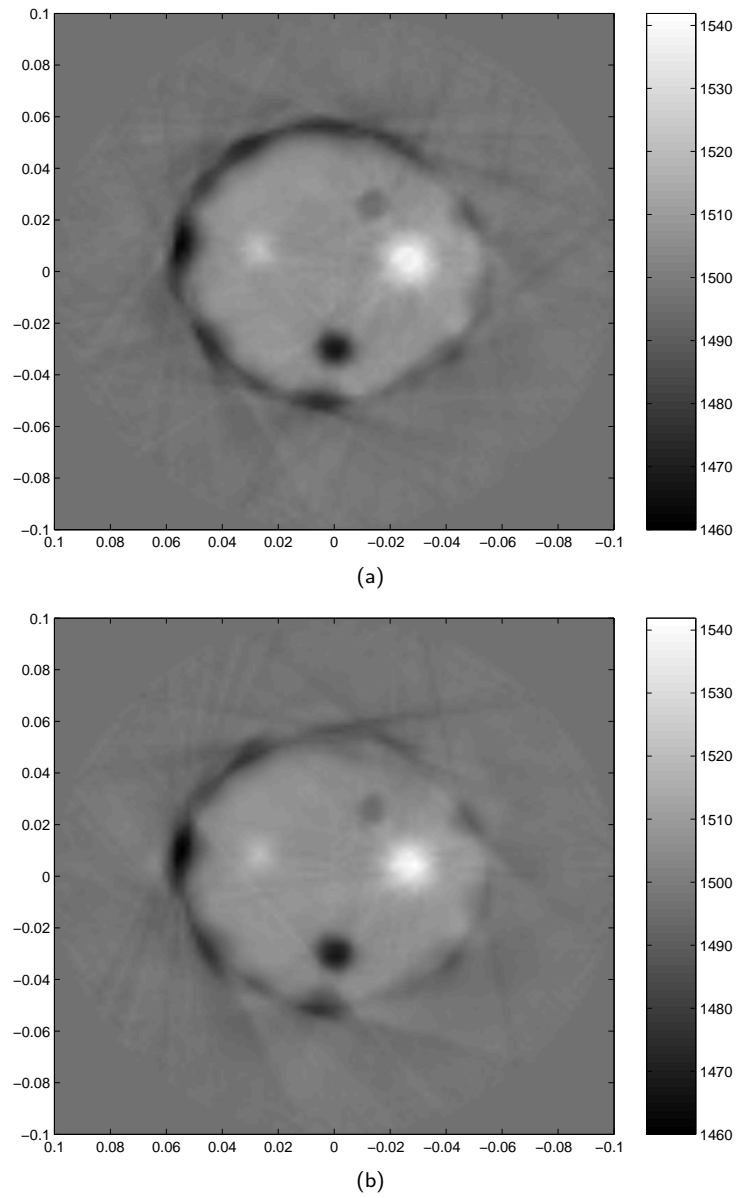


Figure 5.7: Sound speed reconstruction for the phantom study. The time-of-flights are computed using the cross-correlation method. (a) Without beamforming. (b) With beamforming.

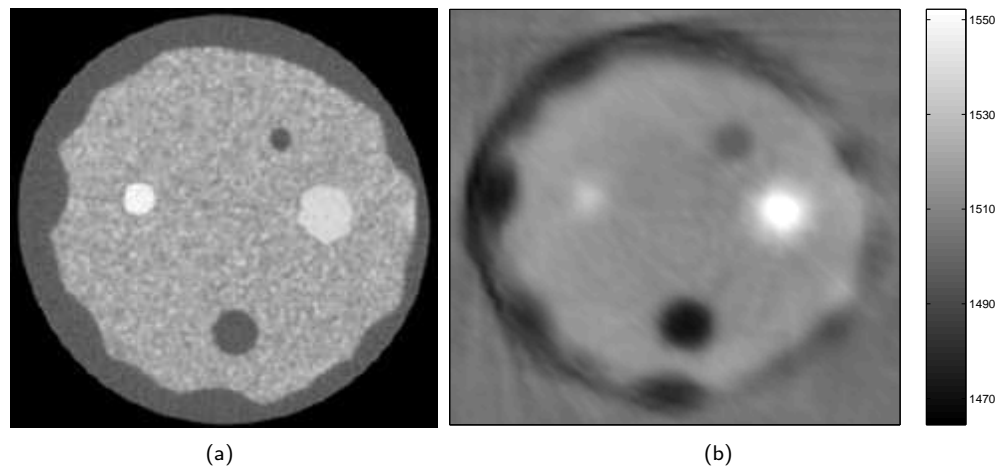


Figure 5.8: Comparison between the CT scan and ultrasound scan. (a) CT scan. (b) Ultrasound transmission tomography scan. Detail from Figure 5.6(b).

5.4.2 In vivo study

The difficulties in imaging the sound speed for the *in vivo* case are mostly due to higher inhomogeneities compared to the *in vitro* case and the fact that the direct received signal is usually very attenuated while the late arrivals are strong.

In Figure 5.9, we present the sound speed images obtained from the time-of-flights estimated with the first peak arrival technique, and, in Figure 5.10, the sound speed images obtained from the time-of-flights estimated with the cross-correlation method. Moreover, for each of these two techniques we compare the reconstructions obtained with and without applying beamforming. As for the *in vitro* case, the first peak arrival method for delay estimation leads to a slightly better reconstruction. However, both techniques generate severe artifacts in the region close to the ring, where the surface wave is dominant. As the cross-correlation method has difficulties in dealing with late arrivals, these artifacts are more pronounced for this method. We notice that in both cases beamforming brings a significant improvement. It successfully removes the late arrivals, which has a positive consequence on the whole reconstruction, and not only in the region where the effect of strong late arrivals is present. The latter is because the artifacts present in one part of the image affects all the trajectories that pass through that region and therefore the effect is spread to the other parts, as well. After beamforming is applied the two time-of-flight estimation techniques lead to similar reconstructions (see Figures 5.9(b) and 5.10(b)). Some differences can be noticed in the region of the water, where sound speed should be constant. Namely, we can see that the variation in this part is smaller for the case when the time-of-flights are based on the first peak arrival estimation technique. All reconstructions reveal the presence of two inclusions with the sound speed above 1570m/s, which is consistent with the presence of cancerous masses. This is further confirmed by the mammography scans that are available for every data set.

We also compared the reconstruction obtained by conjugate-gradient method with the reconstruction obtained using the sparse reconstruction method. In the reconstruction algorithms, we use only a portion of the measurements (10,000 measurements randomly chosen out of 30,000), and we want to see which of the two methods provide the reconstruction closer to the reconstruction obtained with the full set of measurements (e.g. the one shown in Figure 5.9(b)). In this way, the reconstruction with the full set of measurements serves as the ground truth. The reconstruction based on sparsity is performed by minimizing the l_1 -norm of the transformed coefficients. We suppose that the unknown sound speed map is sparse in the wavelet transform domain. The wavelet transform is a multi-scale representation of the image. Coarse-scale wavelet coefficients represent the low resolution image components and fine-scale wavelet coefficients represent high resolution components. It is known that natural, real-life images are sparse in the wavelet transform domain (and the discrete cosine transform domain, as well). The wavelet transform is used in the JPEG-2000 image compression standard [69]. Specifically, we use the Daubechies wavelets family of the 5th order.

Figure 5.11 shows the reconstructions obtained using the two algorithms. We can notice that imposing sparsity in the wavelet domain results in more smooth image, as the recovered coefficients mostly belong to the coarse-scale

coefficients. Still, the inclusions are well recovered and they are slightly more pronounced than in the case of the conjugate-gradient algorithm. The ray-like artifacts present in Figure 5.11(a) are not visible in Figure 5.11(b). For the comparison purpose, we measured the mean and the standard deviation in the water and in the breast in the regions marked by the rectangles in Figure 5.11. It is found that, in the water, the mean values of the sound speed are 1520.4 m/s and 1516.4 m/s, with the standard deviations of 29.8 m/s and 13.8 m/s for the conjugate-gradient and the sparse reconstruction, respectively. Looking at the standard deviations, the results indicate more precise reconstruction in the case of the algorithm based on sparsity. In the breast tissue, the mean sound speed is found to be 1441.5 m/s and 1450.3 m/s with the standard deviation of 17.2 m/s and 11.1 m/s for the conjugate-gradient and sparsity algorithms, respectively. Smaller standard deviation in the latter case suggests that the reconstruction contains less artifacts. Also, as the ray-like artifacts are not present in Figure 5.9(b) we suppose that the reconstruction in Figure 5.11(b) is more accurate. The simulations run for some other syntetic examples show that the reconstruction algorithm based on sparsity outperform the conjugate-gradient method when little data are available [29]. The choice of the sparsifying transform and the level of sparsity that we require in the transform coefficients can affect the reconstruction, as well. These questions are subject of our current research and more details can be found in [29].

5.5 Conclusions

We address the problem of breast cancer detection by computing a map of sound speed in breast tissue. Ultrasound showed to be very sensitive in tissue characterization. The time-of-flight estimation is substantially improved using the beamforming techniques. The technique shows to be very efficient in reducing many artifacts. Next to the reconstruction obtained using the l_2 -norm minimization of error, we also show the reconstructions using the methods based on sparsity. They allow for higher resolution comparing to the classical methods and enable millimeter resolution still employing the simple ray based theory of sound propagation. The latter methods are subject of our future research, as they show a great potential.

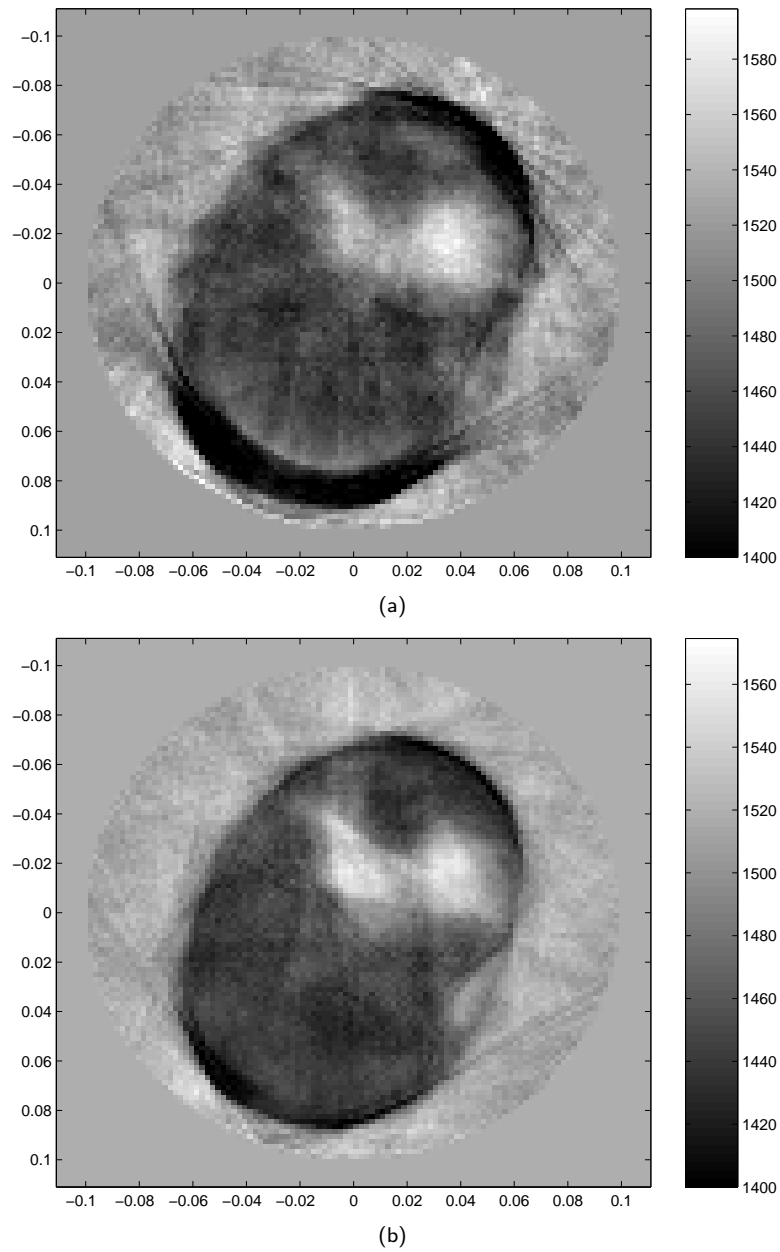


Figure 5.9: Sound speed reconstruction for the *in vivo* study. The time-of-flights are computed using the first peak arrival method. (a) Without beamforming. (b) With beamforming with 7 transmitters and 7 receivers.

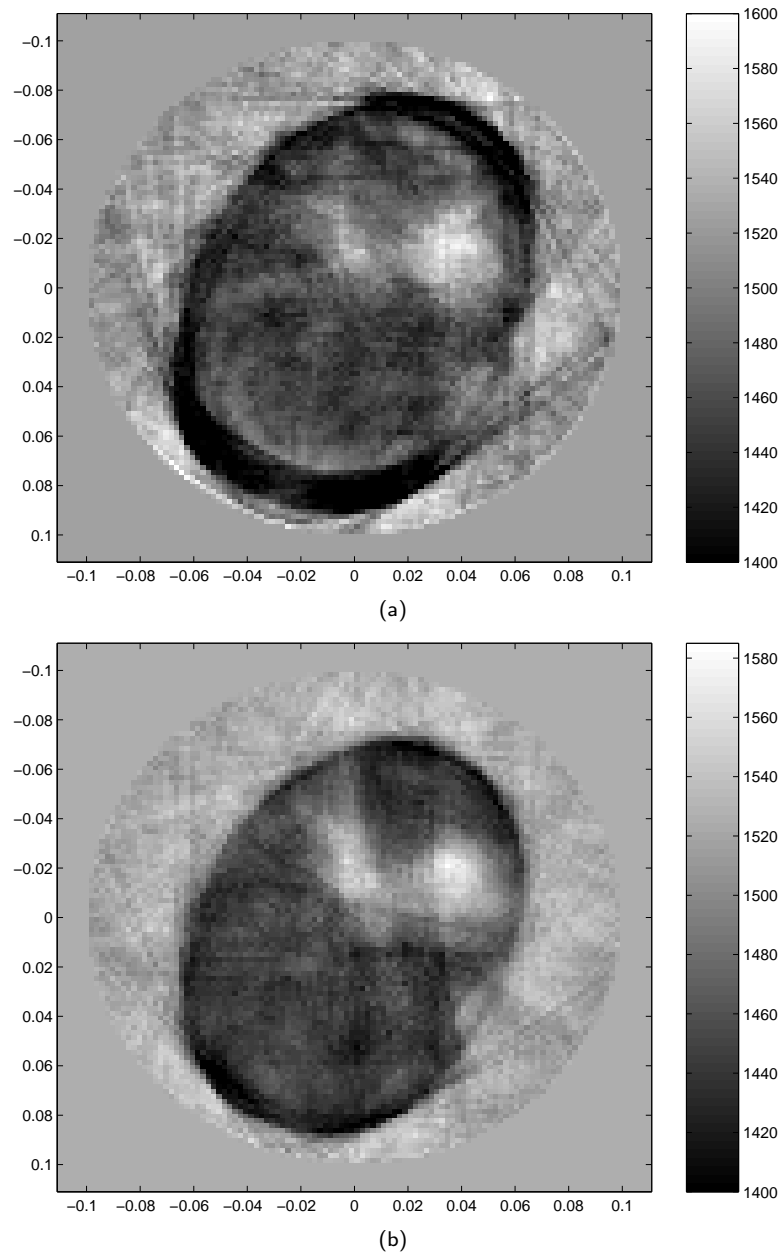


Figure 5.10: Sound speed reconstruction for the *in vivo* study. The time-of-flights are computed using the cross-correlation method. (a) Without beamforming. (b) With beamforming with 7 transmitters and 7 receivers.

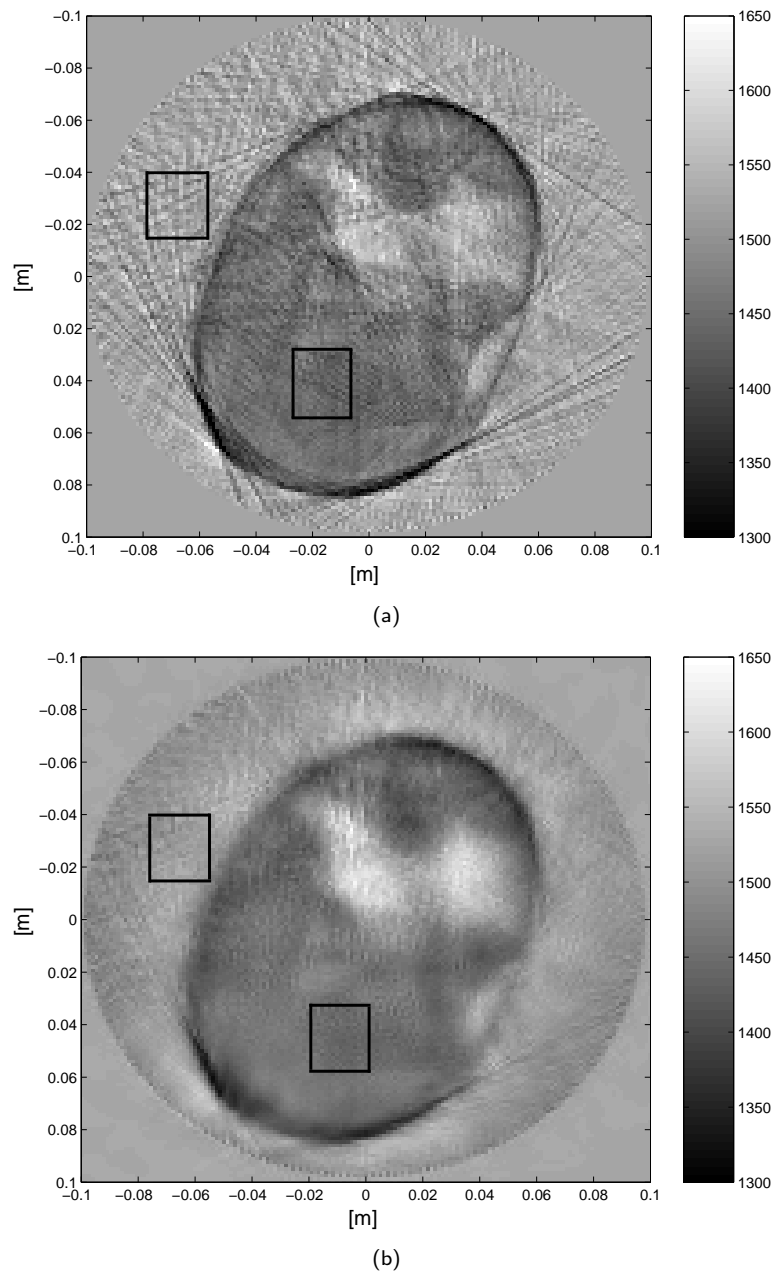


Figure 5.11: Reconstructions from two different algorithms. The number of unknowns is larger than the number of measurements. (a) Conjugate-gradient method. The sound speed in the water is 1520.4 m/s with the standard deviations of 29.8 m/s, and in the breast 1441.5 m/s with the standard deviation of 17.2 m/s. (b) Reconstruction method based on sparsity. The sparsifying transform uses the Daubechies wavelets of the order 5. The sound speed in the water is 1516.4 m/s, with the standard deviation of 13.8 m/s, and in the breast 1450.3 m/s with the standard deviation of 11.1 m/s.

Chapter 6

Thermal Therapy Monitoring

In this chapter, we show how one can monitor temperatures during thermal therapies using ultrasound tomography methods. So far, the use of ultrasound for monitoring and guiding thermal therapies showed to be successful in more common reflection tomography method with B-mode scans. Ultrasound transmission tomography, to the best of our knowledge, was not used for thermal therapy monitoring. In this chapter, we show that ultrasound transmission tomography offers a great potential for temperature monitoring and overcomes some of the problems of B-mode scans.

In Section 6.1, we show that the sound speed can be used as a temperature dependent parameter in order to estimate temperature inside tissue. We conducted two types of experiments in which we measure the temperature induced changes of sound speed. In the first experiment, presented in Section 6.2, we show how the sound speed changes in a tissue-mimicking gelatin phantom in the temperature interval from 10°C to 20°C. The second experiment is motivated by the need to monitor subzero temperature (0°C to -60°C) during tissue freezing in cryosurgery, that is a minimally invasive thermal therapy method used to destroy abnormal tissue. The results of the second experiment are presented in Section 6.3. Finally, some conclusions are given in Section 6.4.

6.1 Temperature monitoring in tissues with ultrasound

A major limitation of thermal therapies is the lack of detailed thermal information needed to monitor and guide the therapy. Temperatures are routinely measured invasively with thermocouples, but this technique is invasive, interactive and provides only sparse measurements. The fact that sound propagation in tissues is significantly influenced by temperature offers a possibility for temperature monitoring using ultrasound. Ultrasound tomography can provide a temperature monitoring modality that is non-invasive, non-interactive, non-ionizing, convenient and inexpensive. This modality is applicable if the temperature-dependent ultrasound parameters are: 1) identified, 2) measured, and 3) calibrated. The sound speed, the attenuation, and the backscattered energy can be identified as the most prominent ultrasound propagation parameters that depend on temperature. In this work, we use the sound speed as the

temperature-dependent parameter, and focus on measuring the temperature induced sound speed changes. Calibration is an important issue, and we will show that the relationship between the temperature and the sound speed is not as simple as it was the case in the atmosphere (see Chapter 7). Although we are not going to study the sound speed versus temperature maps in details, we give an overview of the existing work, especially related to this relationship in the breast tissues.

How does the tissue sound speed change with temperature? In general, speed of sound has the following relationship to coefficient of stiffness C , and material density ρ :

$$c = \sqrt{\frac{C}{\rho}}.$$

Both C and ρ depend on temperature in a non-linear fashion. Moreover, tissue represents a mixture of different materials and therefore the speed vs. temperature relationship needs to be examined individually for every tissue of interest.

In the past, many researchers experimentally measured the speed vs. temperature relationship for different tissue types. One of the first motivations was to provide thermal dosimetry for the treatment of cancer by hyperthermia, or by high temperature ablation, modalities which are now widely accepted by the medical community. It was found that, in water and in most tissue media, sound speed increases with increasing temperature [58], for temperatures above 0°C. However, in fatty tissues, sound speed decreases with increasing temperature [58]. For the case of breast tissue, it is shown in [33] that in non-fatty breast tissue the sound speed increases approximately linearly from 1540m/s to 1580m/s in the temperature interval from 23°C to 43°C. However, the slope for breast fat and fatty breast parenchyma becomes negative between about 32°C and 35°C, and then it is positive for temperature values above 40°C. It is hypothesized that this decrease in speed of sound of fatty breast tissue between 32°C and 35°C is due to the phase changes associated with melting of some components of breast fat.

Currently, there is a growing interest for monitoring the temperatures below 0°C, since many promising minimally invasive thermal therapies are based on freezing the cancerous cells. A precise control of the frozen region growth during the treatment is necessary to protect healthy tissues, vital organs, and major blood vessels. The temperature distribution inside the frozen region is also of importance since the cytotoxic tissue temperatures (i.e. < -20°C) appear only at some distance behind the leading edge of the visualized frozen region. So far, little research is done to construct the speed vs. temperature maps for subzero temperatures. The expectation is that tissues behave similarly to water, in which case the sound speed increases abruptly below 0°C, and continues to increase as the temperature decreases. This is confirmed in case of the skin tissue, and the average sound speed inside the frozen tissue is shown to be 2865 ± 170 m/s [39].

Our work focuses on the problem of measuring the sound speed changes caused by temperature changes, and we do not address the speed vs. temperature mapping.

Comparison to echographic systems In most of the previous work the sound speed changes were observed using ultrasound echographic systems, i.e. B-mode scans. However, in case of subzero temperatures, the B-mode scans can only localize and track the growth of the frozen region, since they reconstruct the reflection image that shows only the edge of the region. The temperatures inside the frozen region are then interpolated based on experience on the temperature gradient observed in the previous experiments [41]. If we imagine more complicated ice forms (not only the iceball), then it becomes difficult to predict the temperature distribution inside the frozen region. This would be the case if, for instance, the freezing takes place close to the blood vessels or any other organ that needs to be protected. As the transmission tomography reconstructs the full sound speed map, the full temperature map can be obtained.

In our work we want to show that transmission ultrasound tomography also provides a tool for temperature monitoring. To this end, we conducted two types of experiments in which we reconstruct the sound speeds for (i) the temperature intervals above zero for which no tissue phase change occurs, and (ii) the subzero temperatures for which tissue phase changes occur. We used the CURE acquisition system presented in Section 5.2. The temperature changes were introduced to the tissue-mimicking phantom and the changes in the phantom sound speed were measured over time.

6.2 Temperature changes without tissue phase change

In the first experiment, the tissue-mimicking phantom (gelatin phantom) is first refrigerated at the temperature of approximately 10°C , and then put in water at a room temperature of 22°C . We measure the sound speed over time using the CURE scanning device. The warming of the phantom with time is expected to cause an increase in the sound speed. In order to correlate the changes in sound speed with the changes in temperature, we measure the temperature sparsely using 6 thermocouples positioned at different distances from the center of the phantom. Due to the symmetry we can then extrapolate the temperatures in the whole phantom. The sound speed measurements and the temperature measurements are taken every 3 minutes during an interval of one hour. The ring setup with the phantom inside is shown in Figure 6.1.

Sound speed reconstruction The reconstruction of the sound speed is not very different from the case studied in Chapter 5. The signal does not undergo strong attenuation, and, therefore, the time estimation is done using the first peak arrival method without beamforming. Figure 6.2 represents the sound speed distribution in the water (inside the outer ring, with the sound speed of approximately 1488m/s), and in the phantom. The reconstruction is computed from the measurements taken 6 minutes, 18 minutes, and 30 minutes after the beginning of the experiment, respectively. As expected, the phantom warms up with time, and the sound speed increases with the increase of the temperature.

In order to relate the sound speed changes to the temperature changes, we measure the temperature with thermocouples, at 6 different positions. The positions are marked in Figure 6.2(a). The temperature changes over time are

shown in Figure 6.3. The dashed lines denote the time instants of 6, 18, and 30 minutes for which we have the reconstructed sound speeds in Figure 6.2. We can notice that the external part of the phantom warms up faster, as it is in direct contact with the water that is at the room temperature. The same behavior is observed from the reconstruction of sound speed inside the phantom in Figure 6.2.

We reconstruct the sound speed for all time slots, and then read the sound speed values at the positions of each thermocouple. However, due to the unprecise positioning of the thermocouples the read sound speeds contain a systematic error. If there were no systematic error, all the 6 lines (one for every thermocouple) should coincide, since the phantom is homogenous. Still, we are able to see that the slopes coincide, and we read that the sound speed inside this gelatin phantom changes linearly in the interval from 11°C to 19°C with a positive trend of $3.3\text{ m/s}/^{\circ}\text{C}$.

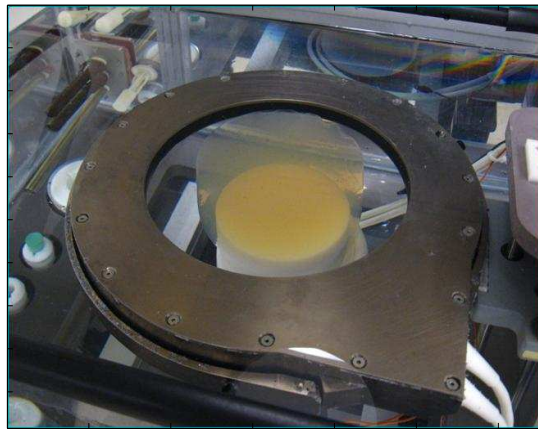
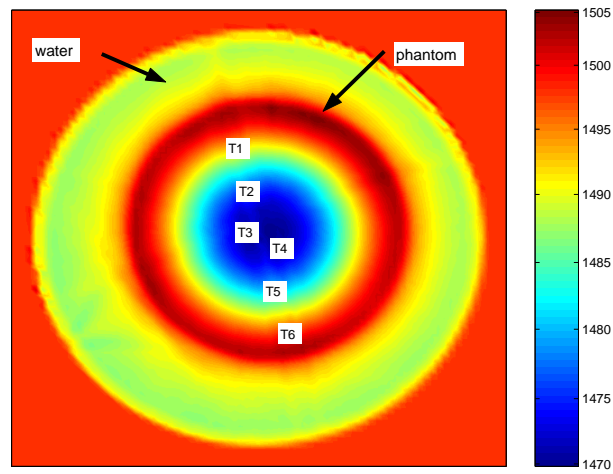
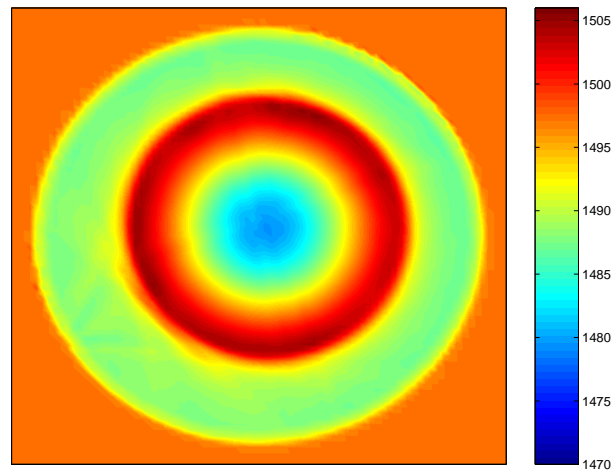


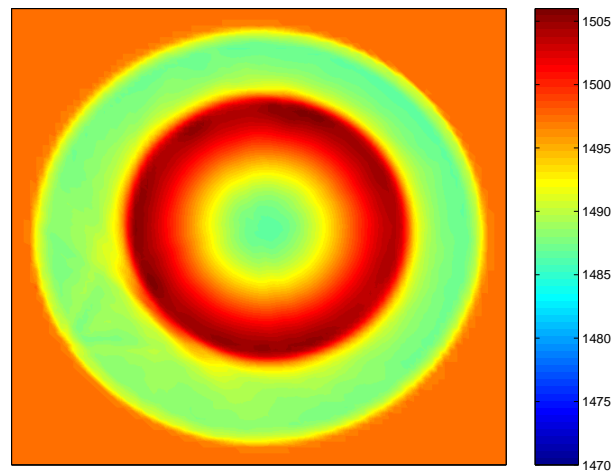
Figure 6.1: CURE temperature monitoring setup. A cold tissue-mimicking phantom (10°C) is immersed in water at a temperature of 22°C . The warming of the phantom is monitored every 3 minutes.



(a)



(b)



(c)

Figure 6.2: Sound speed monitoring. (a) Sound speed reconstruction 6 minutes after the beginning of the experiment. The positions of 6 thermocouples are noted with T1-T6. (b) Sound speed reconstruction 18 minutes after the beginning of the experiment. (c) Sound speed reconstruction 30 minutes after the beginning of the experiment.

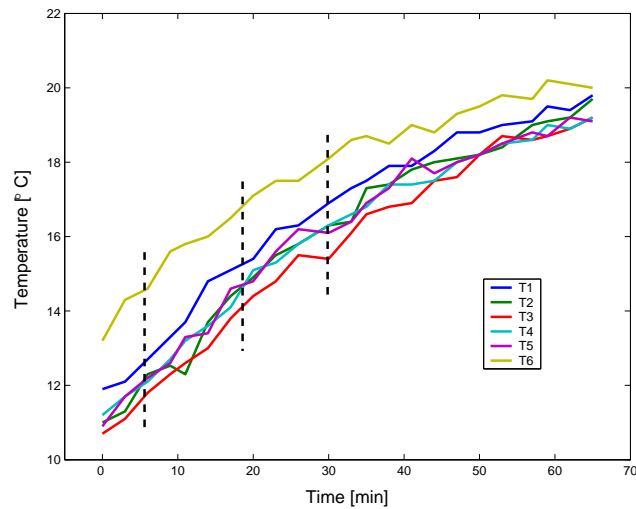


Figure 6.3: Temperature readings from 6 thermocouples denoted with T1-T6, and positioned as shown in Figure 6.2(a). The dashed lines represent the time instants of 6 minutes, 18 minutes, and 30 minutes after the beginning of the experiment. The phantom warms up with time, and we can follow the spatial temperature changes.

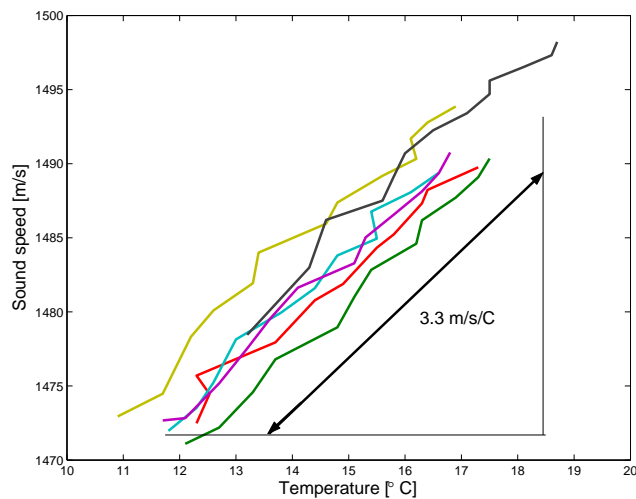


Figure 6.4: The sound speeds versus the temperatures readings at the position of 6 thermocouples. Due to the unprecise positioning of the thermocouples the read sound speeds contain a systematic error. Otherwise, all 6 lines should coincide. The slopes coincide, and it can be read that the sound speed in the gelatine phantom changes linearly in the interval from 11°C to 19°C with a positive trend of 3.3 m/s/°C.

6.3 Temperature changes with tissue phase change

In the second experiment, we aim at monitoring large temperature changes, in the intervals from body temperature to -60°C . The ability to estimate temperature in this interval is of a great importance in cryotherapy, where the sub-zero temperature is used to destroy abnormal tissue.

Cryosurgery Cryosurgery, sometimes referred to as cryotherapy or cryoablation, is a surgical technique that uses cytotoxic cold temperatures to destroy cancerous cells by direct cell injury from ice crystal formation [25]. A coolant or cryogen is circulated through a cryoprobe (see Figure 6.5(a)) that is placed in contact with the tissue to be destroyed. The extraction of heat from the tissue at the cryoprobe tip produces a frozen region that penetrates into the tissue, forming a hemispheric freezing interface commonly called the iceball (see Figure 6.5(b)).

Developed first in the middle of the nineteenth century it has recently experienced a revival thanks to the development of imaging techniques used to monitor the cryosurgery. Onik and Rubinsky [51] worked on imaging monitored cryosurgery with conventional ultrasound. They showed that the discontinuity of the acoustic impedance from unfrozen to frozen tissue can be successfully imaged with B-mode scans. The accuracy of this image is limited by the assumption that the sound speed in the tissue is uniform and known. Because the ice reflects most of the energy, the area behind the freezing interface is in shade, and cannot be imaged. These two drawbacks motivate the development of other techniques as MRI, optical imaging, electrical impedance tomography, for cryosurgery monitoring. MRI overcomes the acoustic shadowing but it is much more expensive and it requires special surgical tools and a special environment. Acoustic tomography offers a promising alternative for monitoring cryosurgery, since the region of interest is insonified from many directions. Therefore, the shadowing effect almost disappear as it will be shown in the following. The technique is also inexpensive and easy to use.

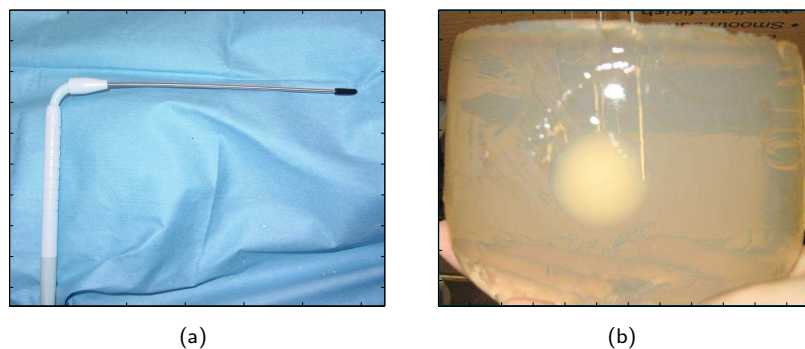


Figure 6.5: Cryosurgery is a minimally invasive thermal therapy. (a) An example of a cryoprobe. They exist in different sizes, needle diameters, and power. (b) The iceball formed inside the gelatine phantom with the diameter of approximately 3 cm.

Sound speed reconstruction The setup used in this experiment is the same as the one used in the first experiment. The gelatine phantom is locally frozen using focal cooling induced by a freeze cycle around an available cryoprobe. We use 3 cryoprobes positioned in the form of a triangle with each cryoprobe being 30 mm away from the other two. The motivation for using the 3 cryoprobes was to show that acoustic tomography has the ability to image complex shapes of frozen regions. After the cryoprobes are powered on, the iceballs around the cryoprobes start to grow, and after 5 – 10 minutes reach the size of approximately 2.0 – 3.0 cm in diameter. We take measurements every 15 seconds. The sound speed estimation inside frozen tissue showed to be a difficult task. We identified two major problems that need to be overcome.

First, upon formation of ice, the sound attenuation in the ice is dramatically increased allowing only 2% of the transmitted energy through the ice. Without help of signal processing tools needed to detect the signal that goes through the frozen part, we only receive the signal that travels on the surface of the iceballs. This signal is not attenuated, and as it travels on the surface of the iceball, where the sound speed is much lower than in the ice, it actually arrives later than the correct signal. As a result, the first reconstructions showed that the sound speed in the frozen tissue decreases linearly (as the iceballs grow) with temperature. This was an obvious indicator that we did not estimate the correct time-of-flights. To increase the power of the received signal we use the beamforming technique introduced in Chapter 5.

Second, upon formation of ice, the sound speed markedly increases (~ 2500 m/s) with respect to non-frozen tissue (~ 1500 m/s). The computed travel times confirm this fact. However, it is difficult to reliably reproduce the strong sound speed gradient that appears around the edge of the ice-zone using the classical tomography reconstruction methods. Therefore, although the travel time indicates a sudden and dramatic change of the sound speed the classical reconstruction is inherently smoothed. To overcome this problem we propose to use the methods based on sparsity (see Section 4.3). The sound speed increases only locally at the positions of the cryoprobes, and therefore the sound speed reconstruction is supposed to be sparse in signal domain. This is particularly advantageous because we do not have to use any sparsifying transform, and the complexity of the algorithm can be reduced. We can also assume that the sound speed distribution is sparse in any other transform domain, for instance, in the wavelet domain. In this case, the reconstruction algorithm applies a sparsifying transform to the signal domain coefficients and searches for a sparse solution in the transform domain. This algorithm outperforms the previous two algorithms, but increases the computational complexity.

The results show that it is possible to estimate a large range of sound speed variations within the tissue. In Figure 6.6, the three cryoprobes are switched on and the cooling had started. However, the ice has not yet formed, and only the three cold zones (lower temperature but still 0°C) are formed. The sound speed in these three regions (at the position of the cryoprobes) is low comparing to the sound speed in the rest of the phantom. This confirms the fact that, above the zero temperature, the sound speed decreases as the temperature decreases. Figure 6.7 represents the sound speed distribution 15 seconds after the three cryoprobes were switched on. The speed is estimated using the two inversion algorithms: the conjugate-gradient (CG) shown in Figure 6.9(a), and

the matching pursuit (MP) shown in Figure 6.7(b). No sparsifying transform is applied in the second algorithm, and only the sparsity in the signal domain is assumed. The ice is formed and the sound speed increases abruptly. The regions of the high sound speed, that is in this case around 1800 m/s, correspond to the ice zones. Still, the speed is not as high as expected due to the inherent smoothing of the tomography methods. Higher reconstruction error concentrated at the edge of the region of interest, i.e. the ring, can be noticed in the CG method. Figure 6.8 shows the details of Figure 6.7 around the three cryoprobes. We can see that the MP method allows to increase the resolution of the image. The pixel size is $1.15 \times 1.15 \text{ mm}^2$ for the MP method, and $2 \times 2 \text{ mm}^2$ for the CG method. The reconstruction in Figure 6.8(b) is more localized, while in Figure 6.8(a) we have a significant blurring effect. Figure 6.9 shows the evolution of the iceballs over time using the CG method, the MP method, and also the method based on sparsity but in the wavelet domain. Specifically, for this example, we use the Daubechies wavelets family of the 7th order.

We can follow the growth of the iceballs indicated by the abrupt increase of the sound speed in that region. For the comparison and the visualization purpose, the color scales are the same for all three methods at each time instant. We can notice that the best reconstruction is obtained by imposing sparsity in the wavelet domain. The CG and the MP methods obtain similar results, but looking at the details (see Figure 6.8) the MP algorithm still performs better. When the iceballs are big, the received signal is very attenuated and the iceballs are losing the exact shape in the CG and MP method (see Figure 6.9(j) and figure 6.9(k)), but the wavelet based sparsity method still gives a good result (see Figure 6.9(l)).

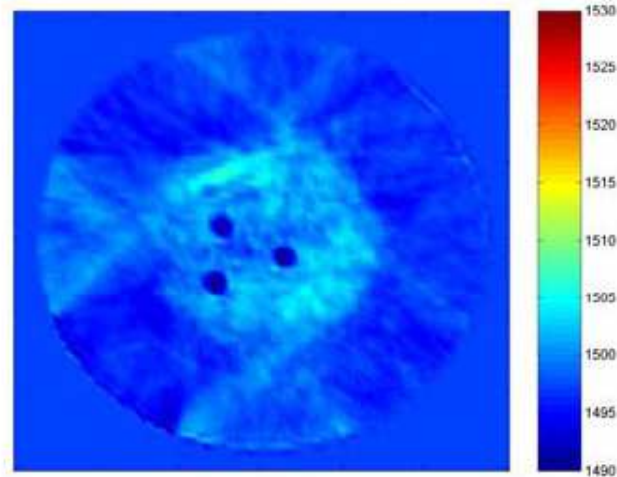


Figure 6.6: The three cryoprobes are switched on but the ice was not yet formed. The sound speed at the position of the cryoprobes is low comparing to the rest.

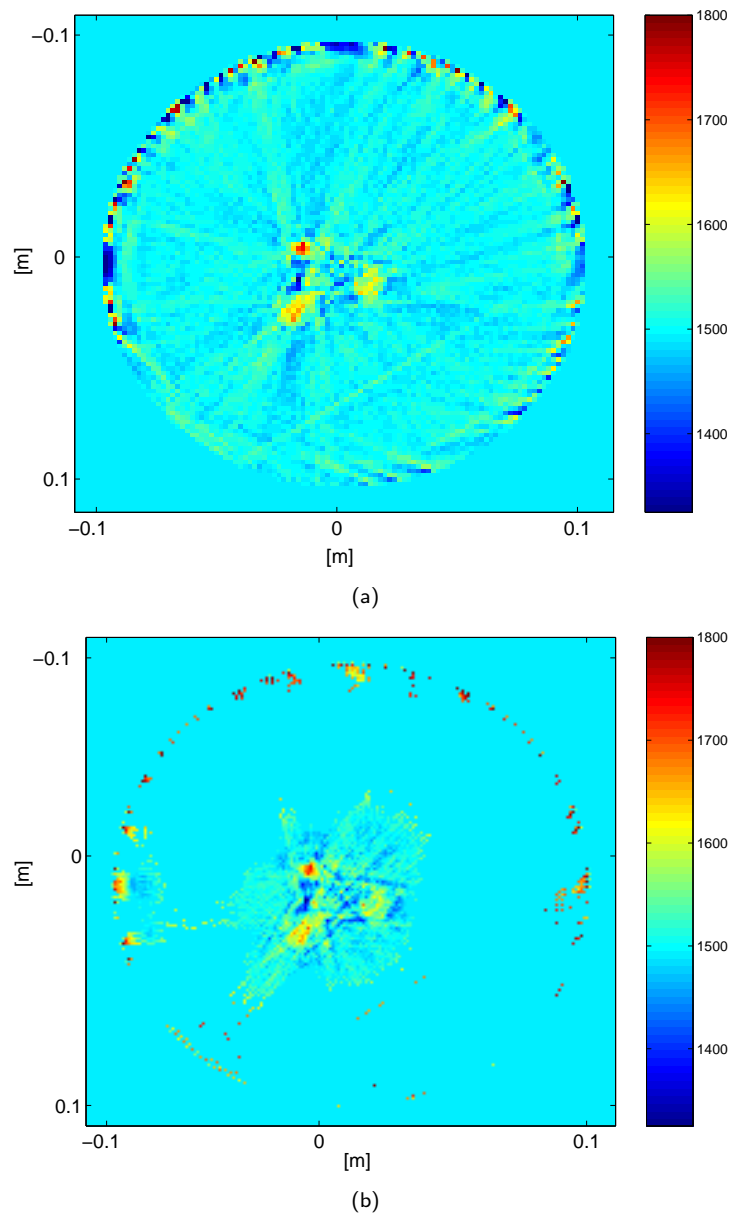


Figure 6.7: Sound speed estimation 15 seconds after the three cryoprobes are switched on. (a) The reconstruction using the conjugate-gradient method. (b) The reconstruction obtained using the inversion based on sparsity, with the matching pursuit algorithm. This method allows to increase the resolution of the image.

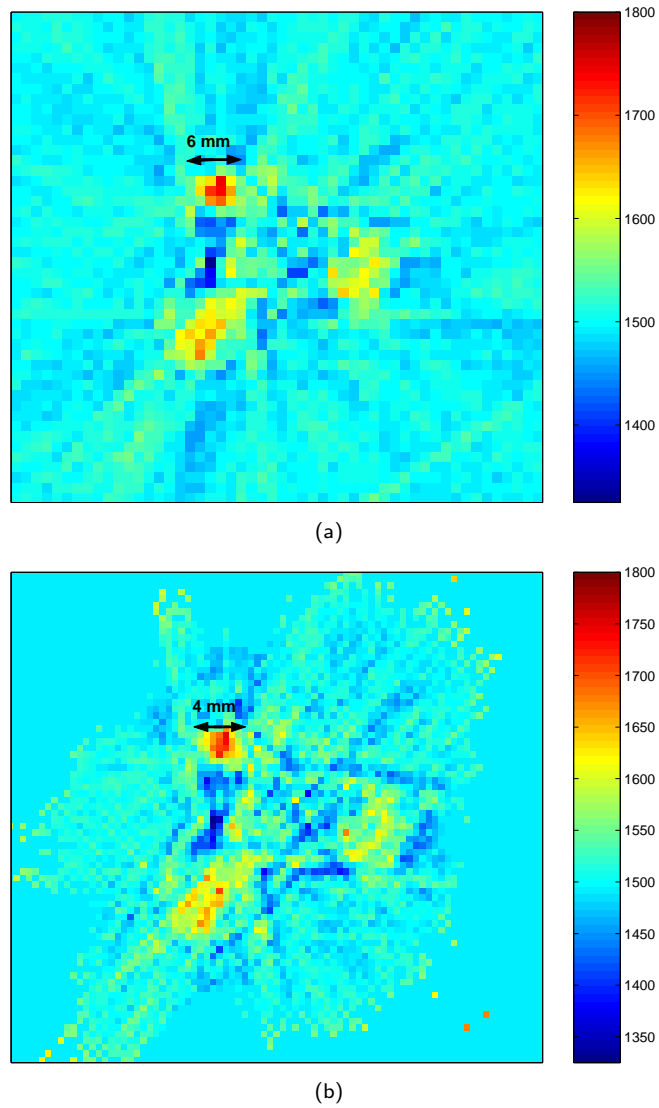


Figure 6.8: Detail of Figure 6.7. (a) The reconstruction using the conjugate-gradient algorithm. Detail of Figure 6.7(a). (b) The reconstruction using the algorithm based on sparsity. Detail of Figure 6.7(b).

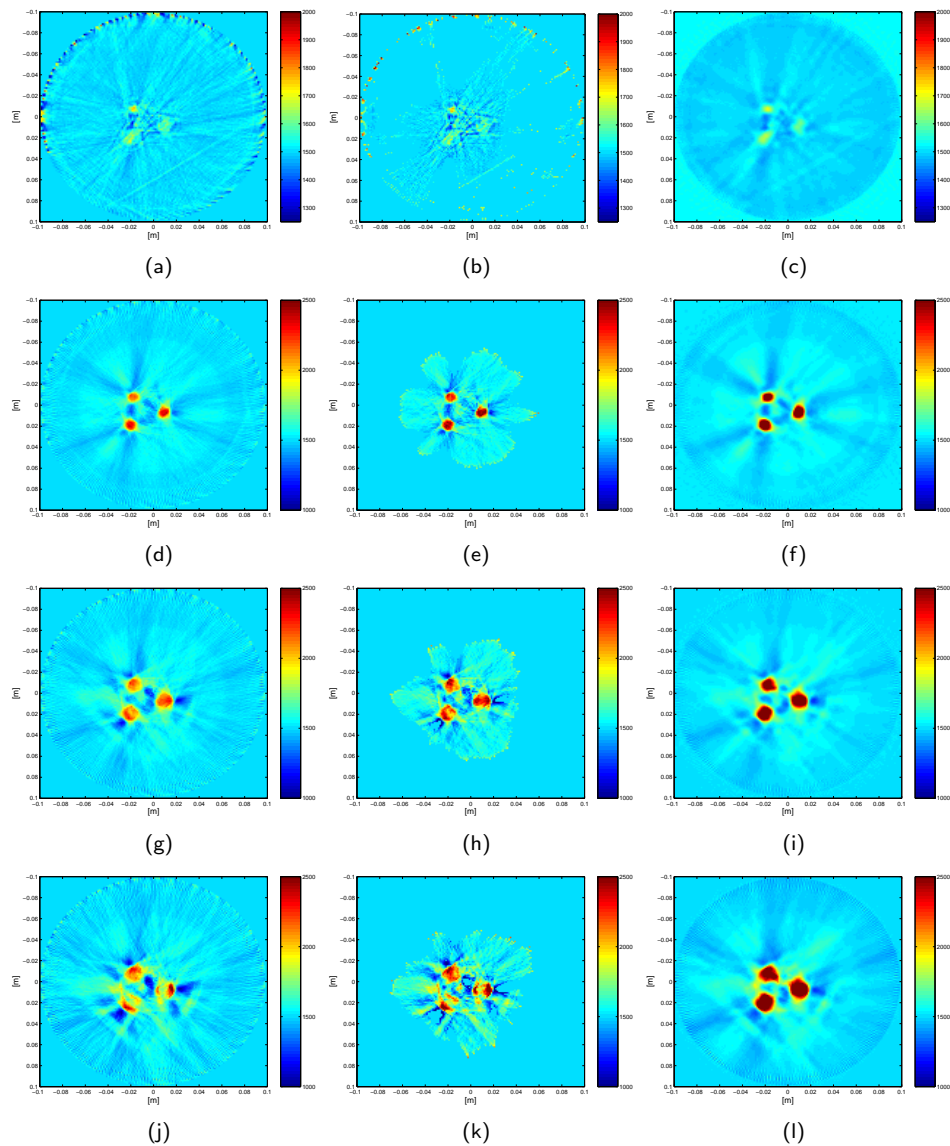


Figure 6.9: Sound speed estimation over time. The iceballs are growing over time, and the sound speed increases as the temperature decreases. The three reconstruction algorithms are compared. (a) 15 s - the reconstruction with the CG method. (b) 15 s - the reconstruction with the MP method. (c) 15 s - the reconstruction with the wavelet based sparsity method. (d) 1 min - the reconstruction with the CG method. (e) 1 min - the reconstruction with the MP method. (f) 1 min - the reconstruction with the wavelet based sparsity method. (g) 1 min 45 s - the reconstruction with the CG method. (h) 1 min 45 s - the reconstruction with the MP method. (i) 1 min 45 s - the reconstruction with the wavelet based sparsity method. (j) 2 min 45 s - the reconstruction with the CG method. (k) 2 min 45 s - the reconstruction with the MP method. (l) 2 min 45 s - the reconstruction with the wavelet based sparsity method.

6.4 Conclusions

Imaging is an important factor in the development of thermal therapies. We showed that transmission tomography is a very promising modality for thermal therapy monitoring. The range of temperatures above zero can be successfully monitored with the methods used in common breast screening. Due to the strong attenuation of the acoustic signal that passes through the frozen tissue, monitoring subzero temperatures is a more difficult problem. The strong attenuation can be efficiently overcome using beamforming techniques. Because the region of interest is insonified from many directions in transmission tomography the shadowing effect is much less noticeable compared to the B-mode scans. Also, the shadowing effect is visible only when the signal passes through two iceballs, that is, along the lines that connect two iceballs. This is because the signal that passes through two iceballs is strongly attenuated. Still, we were able to follow the growth of the 3 iceballs, that was indicated by the sound speed estimation, and confirmed visually. The dramatic change in the sound speed, which is almost a doubling between the unfrozen and frozen tissue enables the imaging of the frozen region with extremely high contrast.

Towards the real time application, we need to reduce the complexity of the reconstruction algorithm. We propose to alternate between the full (usual) and the local reconstruction of the region of interest. In the local reconstruction phase, we monitor only a small region of interest, i.e. the ablation region, and assume that the rest does not change. Still, we periodically perform the full reconstruction in order to correct for possible errors due to the patient movement and global change of temperature.

Inexpensive and easy to use ultrasound tomography has the potential to be the leading modality for thermal temperature monitoring.

Chapter 7

Temperature Estimation in the Atmosphere

In this chapter, we present the experimental setup used for small scale temperature measurements in the atmosphere, built in our laboratory. We deal with the practical details of the realization. In Section 7.1, we present the related work, and point out the directions for improvement. Section 7.2 gives the details of the experimental setup. In Section 7.3, we suggest a new time-of-flight estimation technique that can lower down the cost of the acquisition system, in terms of using a slow A/D convertor, while still insuring high estimation accuracy. In Section 7.4, we discuss the positions calibration of the transducers. Section 7.5, shows the experimental reconstruction of the temperature distribution around a heat source. Section 7.6 concludes the chapter.

7.1 Temperature and wind estimation in the atmosphere

We have already seen that sound propagation in the atmosphere is strongly influenced by temperature and wind, and, therefore, it can be used to measure these physical phenomena. It is also important that the atmosphere is very transparent to low frequency sound, so that the acoustic signal can be transmitted over distances of several hundred meters with low attenuation. The advantage of tomography methods to provide a number of measurements proportional to the square of the number of sensors, can be well used to obtain high resolution reconstructions of temperature and wind fields. It then can be particularly useful for the study of small scale temperature variations and wind turbulences.

Imaging of temperature and wind in near ground atmosphere with acoustic tomography has been already demonstrated in field experiments [76, 78], and lab size experiments [3]. Similarly, but without reconstructing the fields, the authors in [16] studied the effects of large-scale wind velocity fluctuations on the time-of-flight of acoustic signals propagating in a stable stratified atmospheric boundary layer. The signals, transmitted every 20s by a special detonation source, were received on the earth's surface at distances of 2.7km and 4.5km

Table 7.1: Comparison of the experimental setups developed by other research groups.

	Tx	Rx	size	scale	time accuracy
Wilson <i>et al.</i>	3	7	$200 \times 200 \text{ m}^2$	50 m	$1 \cdot 10^{-4} \text{ s}$
Ziemann <i>et al.</i>	8	12	$300 \times 700 \text{ m}^2$	100 m	$3 \cdot 10^{-4} \text{ s}$
Barth <i>et al.</i>	8	8	$4 \times 7 \text{ m}^2$	1 m	$3 \cdot 10^{-6} \text{ s}$
our current setup	12	12	$1 \times 1 \text{ m}^2$	0.15 m	$1 \cdot 10^{-7} \text{ s}$

from the source. Although in all this research the fact that the time-of-flight measurements are not sufficient for the reconstruction of full wind field (but only its longitudinal component) is not taken into account, the experiments show that the application of acoustic tomography in the atmosphere is practically realizable.

A short comparison of the existing experimental setups and the accuracy they achieve in the time-of-flight estimation (one of the crucial factors in tomographic reconstruction) is presented in Table 7.1. The table shows the number of transmitters (Tx), the number of receivers (Rx), the size of the experiment, the resolvable scale in terms of the reconstruction grid size, and the achievable accuracy of the time-of-flight estimation. The present work aims at showing that the current limits can be moved for one order of magnitude in terms of the number of transmitters and the receivers employed, and in terms of the time-of-flight estimation accuracy as well.

We also want to prove that an accurate time-of-flight estimation can be achieved without using expensive and fast audio acquisition cards (A/D converters). Namely, in the atmosphere, the transmitted signal has low frequency, that ranges from 100 Hz for the distances of few hundreds meters to 50 KHz for the distances up to ten meters. To be able to sample this signal without any aliasing, we need a sampling card that works at a frequency only twice higher than the maximal frequency of our signal. The fast acquisition cards increase the precision of the time-of-flight estimates but they are also more expensive. In this work we show how it is possible to estimate the time-of-flights with a precision of two orders of magnitude higher than the sampling period used to acquire the signal.

In the following, we present our experimental setup, used to reconstruct temperature distribution around a heat source from the measurements of the time of flights. The same setup can be extended to wind flow estimation in the case when a wind source is outside the region of interest (source-free vector field).

7.2 Experimental setup

The system is mostly assembled from commercially available audio equipment. The setup consists of 12 emitters and 12 receivers placed on a 1 m radius ring (see Figure 7.1). To suppress the sound reflections the ring is covered with a foam. We use piezoelectric transducers to send and receive the acoustic signal.

The emitters are equipped with amplifiers, and the receivers with preamplifiers, in order to guarantee the signal levels compatible with the audio card (Motu 24I/O card). This card is used to interface the transmitted and the acquired signals with a personal computer. The reconstruction is then performed by the computer. In the following, we are going to describe in more details the components of this setup.

It is important to point out that a small system is very practical to use and reconfigure in a laboratory environment. However, it is quite challenging to design a precise system for the high precisions required for time-of-flight measurements. For our system, we targeted the precision of 10^{-7} s, which is significantly smaller than the sampling period of 10^{-5} s.



Figure 7.1: Experimental setup. It consists of 12 transmitters and 12 receivers placed on the 1 m radius ring

7.2.1 Transducers

Ideally, we would like to have omnidirectional transducers, linear on a wide bandwidth. For the short distances like 1 m, we can use transducers that work on frequencies around 50 KHz. We choose the piezoelectric air transducers, that work at resonant frequency of 40 KHz, and have bandwidth of 2 KHz. We experimented with several transducers but those with the best performance, especially in terms of the beamwidth and the signal power, were the AW8TR40-160C01 (Audiowell Electronics Co., Ltd.) and the Polaroid L-Series transducers. They are shown in Figure 7.2.

7.2.2 Audio card

The signal is generated and acquired by a Motu 24I/O audio card, operated by a computer (see Figure 7.3). The card provides 24, 24-bit/96 KHz analog



Figure 7.2: Polaroid L-Series piezoelectric transducers.

inputs and outputs, and the possibility to connect 4 cards together and thus, extend the number of input and output channels to 96. This option is very favorable when we want to increase spatial resolution. An important feature of this card is that the input and output channels are precisely synchronized. This is clearly crucial for a precise measurement of time-of-flight. However, one should be careful when choosing an audio card as the “perfect synchronization” for audio devices usually refers to the audible perception.



Figure 7.3: MOTU 24I/U audio acquisition card. It has 24 input and 24 output channels, and a possibility to connect 4 MOTU 24I/U cards together.

7.2.3 Amplifiers and preamplifiers

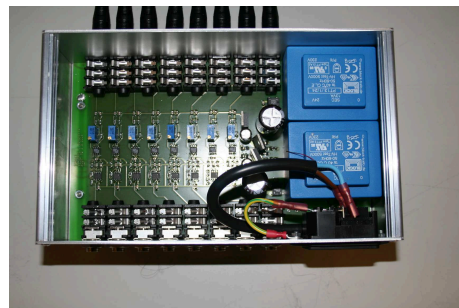
To compensate for relatively modest power levels of input and output signals arrays of amplifiers and preamplifiers are used. Both the amplifiers and preamplifiers are built in our laboratory in order to meet the tight specifications of bandwidth and SNR (see Figure 7.4).

Amplifier We choose a design with two stages shown in Figure 7.5. The first stage is based on the AD815 chip and ensures a gain of 1 to 20 (this can be set with the trimmer PB1). The second stage is used to drive the low impedance load given by the transducers, where the voltage gain is only 2. This stage is based on OPA551UA chip. The gain bandwidth product is 50 MHz for the AD817, and 3 MHz for the OPA551UA. As a result the total bandwidth was larger than the targeted 1 MHz.

Preamplifier Even if the signal at the transducers had a frequency of the order of 40 KHz, the bandwidth of the amplifier needs to be significantly larger to avoid phase distortion. For this reason, we use an operational amplifier LM837 with a high gain-bandwidth product (minimum 15 MHz). The preamplifier consists of three stages. The schematic is shown in Figure 7.6. The signal received by receivers was about 50mVrms to 200mVrms where the Motu 24I/O card input was about 1Vrms. The gain of maximum 60dB is obtained by using three stages based on the LM837 operational amplifiers. This solution has the advantage of a resulting wide bandwidth, that is, in this case, larger than 1 MHz. The DRV135UA chip is used to convert the unbalanced signals to balance signals compatible with the Motu 25I/O input.



(a)



(b)

Figure 7.4: Custom built amplifier and preamplifier.

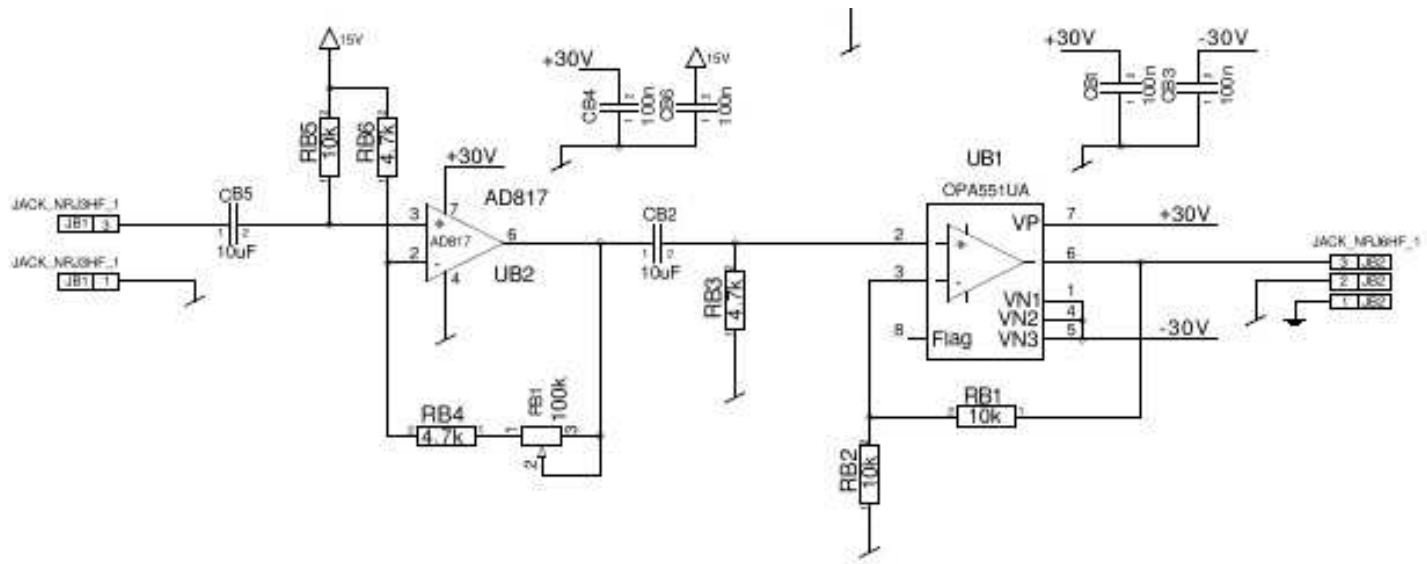


Figure 7.5: Amplifier scheme.

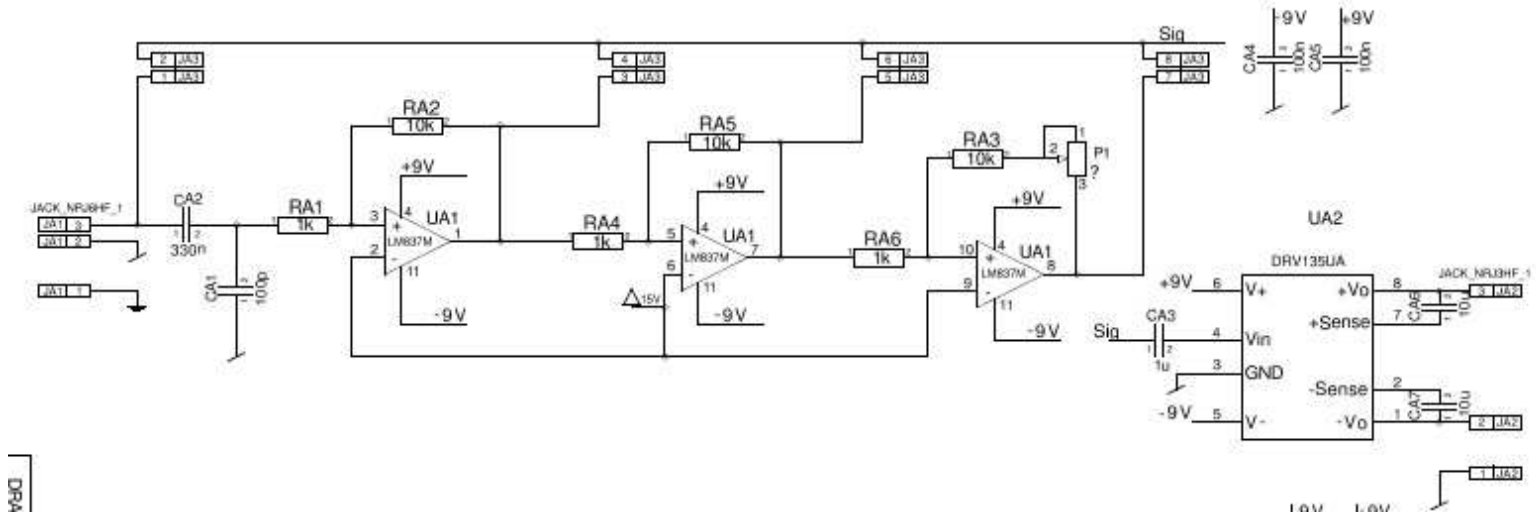


Figure 7.6: Preamplifier scheme.

DRP

7.3 Time of flight estimation

In this section, we introduce a new time-of-flight estimation technique that can be used for the time delay estimation in the atmosphere. The atmosphere has no strong inhomogeneities, as it is the case for tissue structure, and the first reflections can be approximatively determined from the geometry of the experimental setup. For instance, the first reflections come from the frame of the ring. The proposed estimation technique has two main steps: first, the coarse time-of-flight estimation is obtained using the cross-correlation method, and second, a refinement is gained by computing the phase of the sinusoidal part of the signal. More details are present in the following.

7.3.1 Probe signal

As we decided to compute the coarse time-of-flight estimation by computing the cross-correlation between the sent and the received signal, a well defined excitation pattern should be used. It should be clearly distinguishable from ambient noise, and its auto-correlation function should be characterized by a single peak which is as narrow as possible. We choose to send a signal composed of two parts, a pure sinusoidal part at 40 KHz followed by a pseudo-random sequence low-passed with the cutoff frequency of 2 KHz and then modulated at 40 KHz. This guarantees that the transmitted signal is in the range of 38 KHz to 42 KHz, compatible with the chosen transducers. The choice of a pseudo-random sequence is made because its auto-correlation is essentially an impulse, and asymptotically approaches the Dirac delta function. The signal is shown in Figure 7.7.

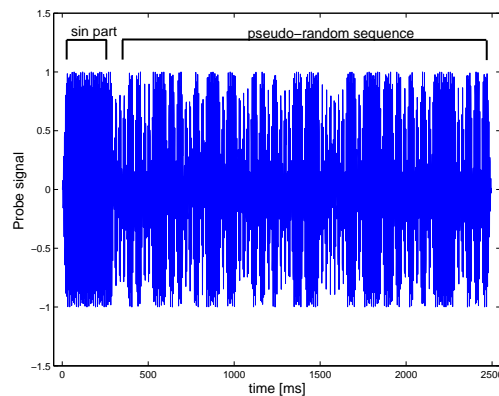


Figure 7.7: Probe signal consists of a sinusoidal part and a pseudo-random sequence.

7.3.2 Sample delay estimation

The received signal is correlated with the transmitted signal. The peak of the cross-correlation function corresponds to the time delay up to the sampling period. In our case, the sampling is performed at the frequency of 96 kHz, what

results in $1.04 \cdot 10^{-5}$ s sampling period. An additional refinement in the precision can be done by upsampling the cross-correlation function. However, the received signal contains a series of delayed versions, due to reflections. This limits the accuracy of the time-of-flight estimation and this problem cannot be overcome by upsampling the correlation function. Thus, we decide to estimate the remaining fractional delay by computing the phase delay of the sinusoidal part.

7.3.3 Subsample delay estimation

The remaining fractional delay is then computed using the phase delay of the sinusoidal part. If the integer delay correctly points at the beginning of the received signal, than we can compute the phase of the sinusoid at that (starting) point, and account for this additional fractional delay in the final estimate (see Figure 7.8). The precision of the fractional delay depends on the length of the sinusoidal part we use to estimate the phase, and it is limited by the arrival of the first reflection. We estimated experimentally the accuracy of the time delay to be of the order of $0.1 \mu\text{s}$. This uncertainty is found as the maximum delay deviation computed from 10 consecutive measurements assuming no temperature changes meanwhile. In this case, the error in the time-of-flight estimation is due only to the noise in the measuring devices.

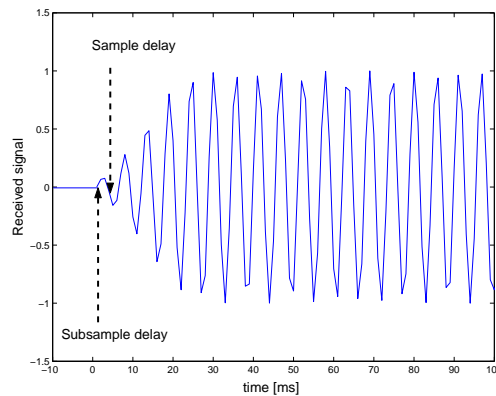


Figure 7.8: The coarse delay computed from the peak of the cross-correlation has a precision of one sampling interval, and might not point to the beginning of the signal. The subsample delay is estimated by computing the phase of the sinusoidal part of the signal. From the computed phase we can correct the delay found by the cross-correlation method.

7.4 Position calibration

The transducers are not mounted on the ring very precisely. Moreover, it is not easy to determine the origin of the acoustic waves generated by the transducer. In addition, the piezoelectric transducers have a certain delay between the application of an input voltage and the actual generation of the

acoustic wave. For these reasons a precise calibration of the positions and delays of the transducers is needed.

To avoid mechanical distance calibration we exploit the very good precision of time-of-flight estimates, and use these measurements to compute the positions and the delays of the transducers. Namely, we set up a system of equation where the unknowns are positions of the transducers and the transducers' delays, and the input data are the time-of-flights calculated between every transmitter and every receiver. We also need to assume a constant and known sound speed, and therefore the calibration needs to be performed in the conditions of no wind and constant known temperature (from which we can compute the sound speed). In the first approximation, we can assume that all the transducers have the same time delay. Then, the calibration is possible if we have at least 5 transmitters and 5 receivers, what results in 25 time-of-flight measurements. The unknowns are the $2 \times 10 = 20$ unknowns position coordinates, minus two unknowns for one reference point (since the measurements determine the relative distances), and plus one unknown for transducers' delays that are assumed to be equal. For the reference point, it can be assumed that the position of the first transmitter is known. Having more transducers will result in having more measurements than the number of unknowns. The system of equation is then solved in the mean squared sense.

In this way the positions are determined up to the precision of 5 mm, for the distances of 1 m, and the delays of the transducers are calculated within the accuracy of $15 \mu\text{s}$. Obviously, this is not enough for estimating the absolute temperature but since the error is mainly systematic its influence can be canceled when estimating only the temperature variation from a fixed known temperature value.

7.5 Results

In our experiment, we estimate the temperature distribution around a hot plate placed inside the ring setup (see Figure 7.1). The calibration is done with respect to a room temperature (22°C), and only the temperature variation is computed. The used transducers are not omnidirectional and have a beamwidth of 50 degrees. Therefore, we do not consider every transmitter-receiver pair, but only the receivers that are inside the transmitting beamwidth, as shown in Figure 7.9. The total number of measurements is, thus, equal to $12 \times 6 = 72$. The region of interest is divided into triangular cells and the linear interpolation is assumed. There are 38 unknowns that represent the nodal points. We took the measurements over short time intervals (5s) in order to check for the consistency of the reconstruction. In Figure 7.10 we show the consecutive reconstructions. They all reveal the presence of the heat source, and we can see that the reconstruction is consistent. In Figure 7.11, we show the reconstruction computed as the average from the reconstruction presented in Figure 7.10. As expected, the average reconstruction has less artifacts on the edge of the region of interest.

It is difficult to evaluate the accuracy of the measurements other than visually or with point measurements. We have used four temperature SHT15 sensors arranged along the line shown as the dashed line in Figure 7.11. The measurements obtained from these sensors showed that the temperature difference between the center of the heat source and the edge of the ring was 2°C . We believe that the difference comes from different practical issues related to the schildering effect of this sensors. Namely, the sensors measure only the temperature of the sensor itself, and it is up to the user to insure that this temperature is equal to the temperature we actually want to measure. However, this is just one more advantage of the acoustic tomography methods, they always measure the temperature in the air (or any other medium).

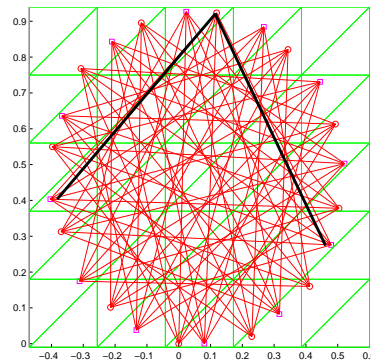


Figure 7.9: The beamwidth of the transducers is 50° , and we only consider trajectories inside that beamwidth.

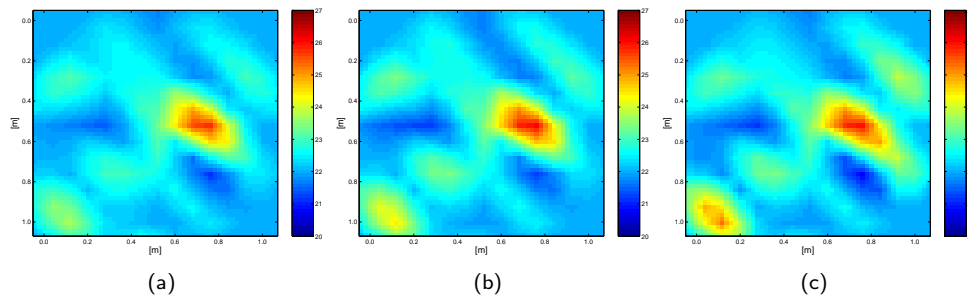


Figure 7.10: Temperature distribution around a heat source for three consecutive measurements.

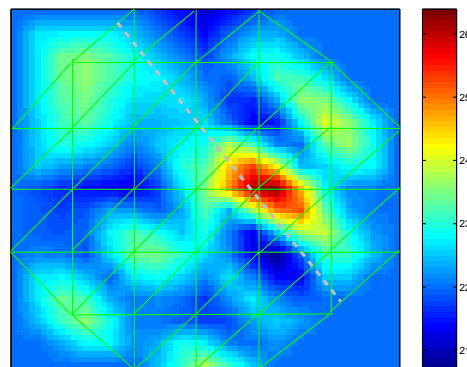


Figure 7.11: Average temperature distribution computed from the reconstructions shown in Figure 7.10.

7.6 Conclusions

In this chapter, we showed that the acoustic tomography in the atmosphere has potentials to be an inexpensive and still efficient technique. Although not used in this phase, the experimental setup can be directly extended for the measurements of solenoidal wind fields. The full wind reconstruction would require the angle-of-arrival measurements that can be realized with acoustic dipoles.

Measurements of sound propagation over great distances are remarkable, but it is also important to say that the time and effort to apply the tomographic method on a large scale are high. Therefore, our guess is that greatest scientific returns will come from acoustical studies at smaller scales, for which the possibilities seem unlimited. We anticipate that the acoustic tomography in the atmosphere will find its main application in resolving small scale temperature and wind variations with high resolution.

Chapter 8

Conclusions

The variety of existing tomography methods and their irreplaceable role in many areas of basic research, medicine and technology describes best how successful these methods are. Their success stems from their non-invasive nature and the fact that they can collect an amount of data proportional to the square of the number of sensors. More specifically, each of many of the tomography disciplines profits from the particular nature of the energy used to probe the measured fields. In this sense, acoustic signals, used in acoustic tomography, showed an extraordinary potential in imaging many properties of the medium, specifically, in the three applications of interest considered in this thesis. The ultimate goal of this thesis was to advance the use of acoustic tomography for breast screening, thermal therapy monitoring, and measurements in the atmosphere, by proposing new improved methods for acoustic signal acquisition and new methods for reconstruction of the measured fields.

8.1 Summary

Inverse problem in acoustic tomography

Acoustic tomography is an inverse problem, and it aims at recovering scalar and vector properties of the observed medium. Trying to image vector properties of the medium fundamentally differs from imaging the scalar properties, as the line integrals of a vector function only allow to recover the solenoidal part of the vector field. We pointed out that this essential phenomena is left out in the literature of acoustic tomography in the atmosphere. This has an unpredictable effect on the reconstruction and perpetuates the incorrect belief that the inverse problem is ill-conditioned while it is ill-posed. As a solution, we suggested a new set of measurements, related to the angle-of-departure and angle-of-arrival of the sound wave. These additional measurements together with the classical time-of-flight measurements allow full reconstruction of vector fields, and moreover, the reconstruction is now physically realizable in acoustic measurements.

Three reconstruction methods for acoustic tomography problems are proposed. The first one is based on quadratic optimization and does not require any a priori information. The second method builds upon the concept of sparsity in order to increase the reconstruction accuracy and resolution. The third

approach views tomographic reconstruction as a parametric estimation problem and solves it using recent results on sampling signals with finite rate of innovation. The proposed methods are compared and their respective advantages are outlined. The first two methods are applied on experimental data as well, and we emphasized the advantages of using the methods based on sparsity.

Breast cancer detection

In spite of competing techniques for diagnosis of soft tissue that have arisen, notably computerized X-ray tomography, ultrasound remains pre-eminent as the diagnostic tool able to probe the most subtle changes in tissue condition at high resolution, low cost, in real time, and in non-ionizing and non-invasive fashion. Thanks to the 360° access, and the soft tissue structure, breast screening can benefit these immense potentials of ultrasound tomography.

Our own contribution to this contemporary research can be summarized in two points. First, we introduced the beamforming technique, that, substantially improves the quality of ultrasound tomography images. It enhances the received signal and improves the SNR, allowing more precise time-of-flight estimation even in very inhomogeneous and absorbent tissue. Second, we show that the reconstruction methods based on sparsity outperform the classical reconstruction algorithms based on l_2 -norm minimization of the error. They also allow for higher resolution comparing to the classical methods and enable millimeter resolution still employing the simple ray based theory of sound propagation.

Thermal therapy monitoring

The development of non-invasive and minimally invasive thermal therapies are firmly related to the development of imaging techniques needed to guide these techniques. The non-invasive nature of acoustic tomography and the low cost implementation, makes it an attractive modality for monitoring thermal therapies. We particularly explored the use of acoustic tomography in monitoring subzero temperatures, since many promising minimally invasive thermal therapies are based on freezing the cancerous cells. One such technique is cryosurgery.

We showed that, by measuring sound speed, we can locate and follow the evolution of frozen regions. This has potentials to be used during cryosurgery to determine precisely the region of cytotoxic temperatures (e.g. $< -20^\circ$). The problem of strong attenuation that acoustic signals undergo when passing through frozen tissue can significantly be overcome using the beamforming technique. However, the increasing frozen region will eventually attenuate the entire signal. Nevertheless, we are only interested in the edge of the cytotoxic zone that is usually 1 cm below the leading edge of the frozen region (for freezing inside a body at 37°C). As shown in our experiments a depth of up to 3 cm can be imaged with acoustic tomography.

Temperature monitoring in the atmosphere

Following the successful application of acoustic tomography in seismology and oceanography, similar methods showed to be beneficial for measuring temperature and wind in the atmosphere.

We demonstrated the feasibility of temperature monitoring in the atmosphere using a custom-built laboratory-scale tomographic experiment. Practical solutions related to the measurement of time-of-flight using cheap, off-the-shelf sensing devices are suggested.

8.2 Future work

Although acoustic tomography is in its nature an estimation problem, many concepts applied in image processing, as compression, super-resolution, and denoising, can further improve the estimation quality.

For example, we have already shown that the inverse methods based on sparsity are very advantageous in the applications of acoustic tomography. There is a lot of freedom in choosing the appropriate basis elements to approximate the field of interest in a sparse manner. The experiences in image compression can be of a great help. For instance, wavelet expansion can be used whenever there are sharp transitions in the field, since wavelets can represent sharp transitions in a very efficient manner. It would be interesting to study the efficiency of other representations as well.

On the other hand, one of the factors that seriously limits the resolution capability of the inverse problem is the number of transducers used during the transmission phase. In the case of uniform sampling the resolution actually relates to the spacing between the transducers. In general, the more transducers, the better the resolution. In order to increase the number of transducers, e.g. on the ring, their size has to decrease proportionally. This prevents the use of cheap, possibly off-the-shelf, sensing devices, which subsequently increases the cost of the hardware significantly. Instead, we propose to use signal processing techniques, referred to as super-resolution [7, 54], in order to increase the resolution, while keeping the number of transducers fixed. Acquisition involves a setup that can rotate by a given angle or at a given speed. The main idea is to combine multiple “low-resolution” tomographic measurements obtained for different angles as a means to increase the resolution. This problem can be treated as a multichannel sampling problem with unknown offsets. It can then be expressed as a set of equations that are linear in the unknown signal coefficients, but nonlinear in the offsets. Based on this approach, new super-resolution methods for unregistered, aliased images have been developed in [71, 70, 72]. Using similar schemes, we plan to study how low-resolution images can be optimally combined in order to account for unknown shifts between the different sets of measurements, for example, due to the movement of the breast during scanning.

Bibliography

- [1] M. P. Andre, H. S. Janee, P. J. Martin, G. P. Otto, B. A. Spivey, and D. A. Palmer, “High-speed data acquisition in a diffraction tomography system employing large-scale toroidal arrays,” *Int. J. Imaging Syst. Technol.*, vol. 8, pp. 137–147, 1997.
- [2] D. F. J. Arago, “Resultats des experiences faites en 1822, par ordre du bureau des longitudes, pour la determination de la vitesse du son dans l’atmosphere,” *Ann. Chim.*, vol. 20, no. 210, 1822.
- [3] M. Barth, K. Arnold, and A. Raabe, “Flow fiels detection using acoustic time tomography,” *Proceedings of the 13th Inter. Symp. for the Advancement of Boundary Layer Remote Sensing*, pp. 81–82, 2006.
- [4] E. H. Barton, “On the refraction of sound by wind,” *Phil. Mag.*, vol. 1, no. 1, pp. 159–165, 1901.
- [5] R. E. Blahut, *Theory and Practice of Error Control Codes*. Addison-Wesley, Reading, MA, 1983.
- [6] D. I. Bolkhintzev, *Acoustics of an inhomogeneous moving medium*. (in Russian) Nauka, Moscow, 1946, [English translation, Physics Dept. Brown Univ., Providence, RI 1956].
- [7] S. Borman and R. Stevenson, “Spatial resolution enhancement of low-resolution image sequences - a comprehensive review with directions for future research,” University of Notre Dame, Technical Report, 1998.
- [8] R. N. Bracewell, “Strip integration in radioastronomy,” *Aust. J. Phys.*, vol. 9, pp. 198–217, 1956.
- [9] D. Braess, *Finite elements: Theory, fast solvers, and applications in solid mechanics*. Cambridge: University Press, 2001.
- [10] H. Braun and A. Hauck, “Tomographic reconstruction of vector fields,” *IEEE Transactions on Signal Processing*, vol. 39, no. 2, 1991.
- [11] S. C. Brenner and L. R. Scott, *The Mathematical Theory of Finite Element Method*. Springer-Verlag New York, 2002.
- [12] E. J. Candes, J. Romberg, and T. Tao, “Robust uncertainty principles: exact signal reconstruction from highly incomplete frequency information,” *IEEE Trans. on Information Theory*, vol. 52, no. 2, 2006.

-
- [13] P. L. Carson, C. R. Meyer, A. L. Scherzinger, and T. V. Oughton, "Breast imaging in coronal planes with simultaneous pulse echo and transmission ultrasound," *Science* 214, vol. 11413, 1981.
- [14] S. S. Chen, D. L. Donoho, and M. A. Saunders, "Atomic decomposition by basis pursuit," *SIAM Journal on Scientific Computing*, vol. 21, no. 1, pp. 33–61, 1998.
- [15] I. P. Chunchuzov, G. A. Bush, and S. N. Kulichkov, "On acoustical impulse propagation in a moving inhomogeneous atmospheric layer," *J. Acoustics Soc. Am.*, no. 88, pp. 455–461, 1990.
- [16] I. P. Chunchuzov, A. I. Otrezov, I. V. Petenko, V. N. Tovchigrechko, A. I. Svertilov, A. L. Fogel, and V. E. Fridman, "Travel-time and duration fluctuation of acoustic pulses in the atmospheric boundary layer," *Izvestiya, Atmospheric and Oceanic Physics*, 1995.
- [17] P. A. Coppin and K. J. Taylor, "A three-component sonic anemometer/thermometer system for general micrometeorological research," *Boundary-Layer Meteorology*, vol. 27, no. 1, 1983.
- [18] A. M. Cormack, "Representation of a function by its line integrals with some radiological applications," *J. Appl. Phys.*, vol. 34, no. 9, pp. 2722–2727, 1963.
- [19] —, "Representation of a function by its line integrals with some radiological applications," *J. Appl. Phys.*, vol. 35, pp. 2908–2913, 1964.
- [20] E. F. Cox, "Abnormal audibility zones in long distance propagation through the atmosphere," *J. Acoustics Soc. Am.*, no. 21, pp. 6–16, 1949.
- [21] F. Delaroche, "Sur l'influence que le vent exerce dans la propagation du son, sous le rapport de son intensite," *Ann. Chim.*, vol. 1, no. 176, 1816.
- [22] D. L. Donoho, "Compressed sensing," *IEEE Trans. on Information Theory*, vol. 52, no. 4, 2006.
- [23] P. Duckert, *Über die Ausbreitung von Explosionswellen in der Erdatmosphäre*. Akademische Verlagsgesellschaft, Leipzig, 1931.
- [24] N. Durica, P. Littrup, L. Poulou, A. Babkin, E. Holsapple, O. Rama, and C. Glide, "Detection of breast cancer with ultrasound tomography: First results with the computed ultrasound risk evaluation (CURE) prototype," *Medical Physics*, vol. 2, no. 34, pp. 773–785, 2007.
- [25] A. A. Gage and J. Baust, "Mechanisms of tissue injury in cryosurgery," *Cryobiology*, vol. 37, no. 3, pp. 171–186, 1998.
- [26] R. Gordon, R. Bender, and G. T. Herman, "Algebraic reconstruction techniques (art) for three-dimensional electron microscopy and x-ray photography," *J. Theor. Biol.*, vol. 29, pp. 471–481, 1970.
- [27] R. J. Greenfield, M. Teufel, D. W. Thomson, and R. L. Coulter, "A method for measurement of temperature profiles in inversions from refractive transmission of sound," *J. Geophys. Res.*, no. 79, pp. 5551–5554, 1974.

-
- [28] J. F. Greenleaf, A. Johnson, R. C. Bahn, and B. Rajagopalan, "Quantitative cross-sectional imaging of ultrasound parameters," in *1977 Ultrasonics Symposium Proc., IEEE Cat. 77CH1264-1SU*, 1977, pp. 989–995.
- [29] A. Hormati, I. Jovanović, and M. Vetterli, "Acoustic tomography: Reconstruction algorithms based on sparsity," Technical Report, LCAV/EPFL, 2008.
- [30] G. N. Hounsfield, "A method of and apparatus for examination of a body by radiation such as x ray or gamma radiation," The Patent Office, London, Patent Specification 1283915, 1972.
- [31] —, "Computerized transverse axial scanning (tomography): Part 1. description of system," *Brit. J. Radiol.*, vol. 46, pp. 1016–1022, 1973.
- [32] S. A. Johnson, D. T. Borup, J. W. Wiskin, F. Natterer, F. Wuebling, Y. Zhang, and C. Olsen, "Apparatus and method for imaging with wavefields using inverse scattering techniques," United States Patent No. 6,005,916, 1999.
- [33] S. A. Johnson, D. A. Christensen, C. C. Johnson, J. F. Greenleaf, and B. Rajagopalan, "Non-intrusive measurement of microwave and ultrasound-induced hyperthermia by acoustic temperature tomography," in *Ultrasonics Symposium Proceedings, IEEE Cat. T77Ch1264-1SU*, 1977.
- [34] S. A. Johnson, J. F. Greenleaf, C. R. Hansen, W. F. Samayoa, A. L. M. Tanaka, D. A. Christensen, and R. L. Wooley, "Reconstructing three-dimensional fluid velocity vector fields from acoustic transmission measurements," *Acoustical Holography*, L. W. Kessler, ed. New York: Plenum, vol. 7, pp. 307–326, 1977.
- [35] I. Jovanović, A. Hormati, M. Vetterli, and O. Roy, "Method for signal enhancement in acoustic tomography," to be submitted United States Patent, 2008.
- [36] I. Jovanović, L. Sbaiz, and M. Vetterli, "Acoustic Tomography for Estimating Temperature and Wind Flow," in *13-th Intern. Symp. for the Advancement of Boundary Layer Remote Sensing (ISARS)*, 2006.
- [37] I. Jovanović, A. Hormati, L. Sbaiz, and M. Vetterli, "Efficient and Stable Acoustic Tomography Using Sparse Reconstruction Methods," in *19th International Congress on Acoustics*, 2007.
- [38] P. Juhlin, "Principles of doppler tomography," *Proc. 15th Annual International Conference of IEEE Engineering in Medicine and Biology Society*, 1993.
- [39] P. Laugier, E. Laplace, J.-L. Lefaix, and G. Berger, "In vivo results with a new device for ultrasonic monitoring of pig skin cryosurgery: The echographic cryoprobe," *Journal of Investigative Dermatology*, vol. 111, pp. 314–319, 1998.
- [40] C. Li, L. Huang, N. Duric, H. Zhang, and C. Rowe, "An improved automatic time-of-flight picker for medical ultrasound tomography," *To be submitted*, 2008.

-
- [41] P. J. Littrup, L. Freeman-Gibb, A. Andea, M. White, K. C. Amerikia, D. Bouwman, T. Harb, and W. Sakr, "Cryotherapy for breast fibroadenomas," *Radiology*, vol. 234, pp. 63–72, 2005.
- [42] D.-L. Liu and R. C. Waag, "Propagation and backpropagation for ultrasonic wavefront design," *IEEE Trans. Ultrason. Ferroelectr. Freq. Control*, vol. 44, no. 1, pp. 1–13, 1997.
- [43] I. Maravic and M. Vetterli, "Sampling and Reconstruction of Signals with Finite Rate of Innovation in the Presence of Noise," *IEEE Transactions on Signal Processing*, vol. 53, no. 8, pp. 2788–2805, 2005.
- [44] —, "A sampling theorem for the radon transform of finite complexity objects," in *IEEE Conference on Acoustics, Speech and Signal Processing*, vol. 2, 2002, pp. 1197–1200.
- [45] —, "Exact Sampling Results for Some Classes of Parametric Non-Bandlimited 2-D Signals," *IEEE Transactions on Signal Processing*, vol. 52, no. 1, pp. 175–189, 2004.
- [46] V. Z. Marmarelis, T. Kim, and R. E. Shehada, "Paper 5035-6," in *Proceedings of the SPIE: Medical Imaging 2003*, Feb. 2002.
- [47] W. Munk and C. Wunsch, "Observing the ocean in the 1990s," *Phil. Trans. R. Society London*, pp. 439–464, 1982.
- [48] F. Natterer, *The mathematics of computerized tomography*. Philadelphia, PA, USA: Society for Industrial and Applied Mathematics, 2001.
- [49] S. J. Norton, "Tomographic reconstruction of 2-D vector fields: Application to flow imaging," *Geophysics Journal*, vol. 97, pp. 161–168, 1988.
- [50] —, "Unique tomographic reconstruction of vector fields using boundary data," *IEEE Transactions on Image Processing*, vol. 1, no. 3, 1992.
- [51] G. Onik, C. Cooper, H. I. Goldenberg, A. A. Moss, B. Rubinsky, and M. Christianson, "Ultrasonic characteristics of frozen liver," *Cryobiology*, vol. 21, pp. 321–328, 1984.
- [52] V. E. Ostashev, "Return-inclined acoustic sounding of the atmosphere," *Izv. Acad. Science USSR Atmos. Ocean Phys.*, no. 18, pp. 695–698, 1982.
- [53] —, *Acoustics in moving inhomogeneous media*. E&FN SPON, London, 1997.
- [54] S. C. Park, M. K. Park, and M. G. Kang, "Super-resolution image reconstruction: a technical overview," *IEEE Signal Processing Magazine*, vol. 20, no. 3, pp. 21–36, May 2003.
- [55] D. P.L. and M. Vetterli, "Exact sampling results for signals with finite rate of innovation using stang-fix conditions and local kernels," in *IEEE Conference on Acoustics, Speech and Signal Processing*, 2005.
- [56] W. H. Press, S. A. Teukolsky, W. T. Vetterling, and B. P. Flannery, *Numerical recipes in C (2nd ed.): the art of scientific computing*. New York, NY, USA: Cambridge University Press, 1992.

-
- [57] J. Radon, "Über die bestimmungen von funktionen durch ihre integralwerte längs gewisser mannigfaltigkeiten," *Ber. Vehr. Sächs. Akad. Wiss. Leipzig, Math-Nat. Kl.*, vol. 69, pp. 262–277, 1917.
- [58] B. Rajagopalan, J. F. Greenleaf, P. J. Thomas, S. A. Johnson, and R. C. Bahn, "Ultrasonic tissue characterization II," M. Linzer, Ed. Washington, D.C.: U.S. GPO, NBS Spec. Pub. 525, pp. 227–233, 1979.
- [59] L. Rayleigh, *Theory of sound*. Dover, New York, 1945.
- [60] O. Reynolds, "On the refraction of sound by the atmosphere," *Proc. Roy. Soc. Lond.*, vol. 22, pp. 315–324, 1874.
- [61] D. J. D. Rosier and A. Klug, "Reconstruction of three-dimensional structures from electron micrographs," *Nature*, vol. 217, pp. 130–134, 1968.
- [62] P. D. Rowley, "Quantitative interpretation of three-dimensional weakly refractive phase objects using holographic interferometry," *J. Opt. Soc. Amer.*, vol. 59, pp. 1496–1498, 1969.
- [63] O. Roy and M. Vetterli, "The Effective Rank: A Measure of Effective Dimensionality," in *European Signal Processing Conference (EUSIPCO)*, 2007, pp. 606–610.
- [64] L. Sbaiz and M. Vetterli, "Acoustic flow tomography," Technical Report, LCAV/EPFL, 2003.
- [65] V. A. Sharafutdinov, "Tomographic methods in optics," *Proc. SPIE, Tomographic methods in optics*, 1991.
- [66] J. L. Spiesberg and K. M. Fristrup, "Passive localization of calling animals and sensing of their acoustic environment using acoustic tomography," *Am. Nat.*, no. 135, pp. 107–153, 1990.
- [67] P. Stoica and R. Moses, *Introduction to Spectral Analysis*. Prentice Hall, 2000.
- [68] G. G. Stokes, "On the effect of wind on the intensity of sound," *Brit. Assoc. Report*, p. 22, 1857, (Reprinted in *Mathematical and physical papers of G.G. Stokes*, Cambridge University Press, Vol. 4, 1904, pp. 110 – 111).
- [69] D. S. Taubman and M. W. Marcellin, "JPEG-2000: Image Compression Fundamentals, Standards and Practice," *Kluwer International Series in Engineering and Computer Science*, 2002.
- [70] P. Vandewalle, L. Sbaiz, J. Vandewalle, and M. Vetterli, "Super-Resolution from Unregistered and Totally Aliased Signals Using Subspace Methods," *IEEE Transactions on Signal Processing*, vol. 55, no. 7, Part 2, pp. 3687–3703, 2007.
- [71] P. Vandewalle, S. Ssstrunk, and M. Vetterli, "A Frequency Domain Approach to Registration of Aliased Images with Application to Super-Resolution," *EURASIP Journal on Applied Signal Processing (special issue on Super-resolution)*, pp. Article ID 71 459, 14 pages, 2006.

-
- [72] P. Vandewalle, “Super-resolution from unregistered aliased images,” Ph.D. dissertation, 2006. [Online]. Available: <http://library.epfl.ch/theses/?nr=3591>
- [73] S. N. Vercherin, V. E. Ostashev, A. Zeimann, D. K. Wilson, K. Arnold, and M. Barth, “Tomographic reconstruction of atmospheric turbulence with the use of time-dependent stochastic inversion,” *J. Acoust. Soc. Am.*, vol. 122, no. 3, 2007.
- [74] M. Vetterli, P. Marziliano, and T. Blu, “Sampling signals with finite rate of innovation,” *IEEE Trans. on Signal Proc.*, vol. 50, no. 6, pp. 1417–1428, 2002.
- [75] D. K. Wilson, V. E. Ostashev, S. N. Vercherin, A. G. Voronovich, S. L. Collier, and J. M. Noble, “Assessment of acoustic travel-time tomography of the atmospheric surface layer,” in *AMS Symposium on Boundary Layers and Turbulence*, 2004.
- [76] D. K. Wilson and D. W. Thomson, “Acoustic tomographic monitoring of the atmospheric surface layer,” *J. Atmos. Ocean. Tech.*, no. 11, pp. 751–769, 1994.
- [77] P. M. Woodward, *Probability and information theory, with applications to radar*. London : Pergamon Press, 1953.
- [78] A. Ziemann, K. Arnold, and A. Raabe, “Acoustic travel time tomography – a method for remote sensing of the atmospheric surface layer,” *Meteorology and Atmospheric Physics*, pp. 43–51, 1999.

Curriculum Vitae

Ivana Jovanović

Avenue Vinet 20
1004 Lausanne
Switzerland

Audiovisual Communications Laboratory (LCAV)
School of Computer and Communication Sciences (I&C)
Ecole Polytechnique Fédérale de Lausanne (EPFL)
BC320 - Station 14
1015 Lausanne, Switzerland

Email: Ivana.Jovanovic@epfl.ch
Web: <http://lcavwww.epfl.ch/~ivana>

Personal

Date of birth: 18/04/1978
Nationality: Serbian

Education

- Feb. 04 - Present Doctoral Program in Computer, Communication and Information Sciences Ecole Polytechnique Fédérale de Lausanne, Switzerland, Supervisors: Prof. Martin Vetterli and Dr. Luciano Sbaiz.
- Oct. 02 - Oct. 03 Pre-Doctoral School in Communication Systems, Ecole Polytechnique Fédérale de Lausanne, Switzerland
- Oct. 97 - July 02 Master's degree in Telecommunication Systems, University of Belgrade, Faculty of Electrical Engineering, Belgrade, Serbia

Professional Experience

- Feb. 04 - Present Teaching assistant for various signal processing classes (bachelor, master and doctoral school's level)
- Jun. 07 - Aug. 07 Research Intern at the Karmanos Cancer Institute, Wayne State University, Detroit, Michigan, USA. Experimental work on the acoustic tomographic scanner used for breast cancer diagnose
- Oct. 01 - Jun 02 Laboratory assistant at the Department Of Electronics, Faculty of Electrical Engineering, Belgrade
- Jun 01 -Aug. 01 Joined the GSM OM Group in Mobtel, the biggest GSM operator in Serbia, for a 1-month internship. Worked on network performance analysis and improvements
- Feb. 97- Aug. 97 Junior assistant at the Petnica Science Center, Serbia, for the program "Applied Physics and Electronics"

Publications

Journal papers

1. I. Jovanović, L. Sbaiz and M. Vetterli, "Acoustic tomography for scalar and vector fields: theory and application to temperature and wind estimation," accepted to the *Journal of atmospheric and oceanic technology*, 2008.
2. I. Jovanović and B. Beferull-Lozano, "Oversampled A/D Conversion and Error-Rate Dependence of Non-Bandlimited Signals with Finite Rate of Innovation," *IEEE Transactions on Signal Processing*, Vol. 54, Nr. 6, pp. 2140 - 2154, 2006.

Conference papers

1. I. Jovanovic, P. Littrup, N. Duric, O. Rama, L. Sbaiz and M. Vetterli, "Noninvasive temperature monitoring in breast-mimicking phantoms using acoustic tomography," *Swiss Society of Biomedical Engineering Meeting*, 2007.
2. I. Jovanovic, A. Hormati, L. Sbaiz and M. Vetterli, "Efficient and Stable Acoustic Tomography Using Sparse Reconstruction Methods," *19th International Congress on Acoustics*, 2007.
3. I. Jovanovic, L. Sbaiz and M. Vetterli, "Tomographic approach for parametric estimation of local diffusive sources and application to heat diffusion," *IEEE International Conference on Image Processing*, Vol. 4, pp. 153-156, 2007.

-
4. P. Vandewalle, G. Barrenetxea, I. Jovanovic, A. Ridolfi and M. Vetterli, "Experiences with Reproducible Research in Various Facets of Signal Processing Research," *Proc. IEEE Conference on Acoustics, Speech and Signal Processing*, Vol. 4, pp. 1253-1256, 2007.
 5. I. Jovanovic, L. Sbaiz and M. Vetterli, "Acoustic tomography for estimating temperature and wind flow," *13th International Symposium for the Advancement of Boundary Layer Remote Sensing, ISARS*, pp. 69-71, 2006.
 6. I. Jovanovic, L. Sbaiz and M. Vetterli, "Acoustic Tomography Method for Measuring Temperature and Wind Velocity," *IEEE International Conference on Acoustics, Speech, and Signal Processing*, 2006.
 7. I. Jovanovic and B. Beferull-Lozano, "Oversampled A/D Conversion of Non-Bandlimited Signals with Finite Rate of Innovation," *IEEE Conference on Acoustics, Speech and Signal Processing*, Vol. 2, pp. 797-800, 2004.
 8. I. Jovanović and B. Beferull-Lozano, "Error-Rate Dependence of Non-Bandlimited Signals with Finite Rate of Innovation," *IEEE International Symposium on Information Theory (ISIT)*, pp. 493, 2004.